Aus der Klinik für Psychiatrie und Psychotherapie

Labor für Molekulare Psychiatrie

der Medizinischen Fakultät Charité – Universitätsmedizin Berlin

DISSERTATION

The role of microglia dysfunction in Huntington's Disease

zur Erlangung des akademischen Grades

Doctor of Philosophy (PhD)

vorgelegt der Medizinischen Fakultät

Charité – Universitätsmedizin Berlin

von

Ekaterini Maria Lyras

aus London, Vereinigtes Königreich

Datum der Promotion: 04.06.2021

Table of contents

Abbreviations

Note: Throughout the manuscript genes are given in *Italics*

Actb	beta-actin
ANOVA	analysis of variance
ARRIVE	Animal Research: Reporting of In Vivo Experiments
AU	arbitrary units
BBB	blood-brain barrier
BDNF	brain-derived neurotrophic factor
BSA	bovine serum albumin
C/EPB	CCAAT-enhancer binding protein
CAG	Cytidine Adenosine Guanosine
CBLM	cerebellum
CBP	CREB-binding protein
cDNA	complementary DNA
CNS	central nervous system
CREB	cAMP response element-binding protein
CSF-1R	colony stimulating factor 1 receptor
CTX	cortex
CX3CR1	chemokine, CX3C motif, receptor 1
D2R	dopamine receptor D2 (protein)
DAB	3,3'-Diaminobenzidine
DAPI	diamidino-2-phenylindole
Darpp-32	dopamine- & adenosine 3':5'-monophosphate-regulated phosphoprotein
ddH_2O	double-distilled H_2O
DEPC	diethyl pyrocarbonate
DMEM	Dulbecco's modified Eagle medium
DNA	deoxyribonucleic acid
DPBS	Dulbecco's phosphate buffered saline
Drd1	dopamine receptor D1 (gene)
Drd2	dopamine receptor D2 (gene)
EDTA	Ethylenediaminetetraacetic acid
ERT2	mutated oestrogen receptor
exon1-mHTT	human mHTT exon 1
FACS	fluorescence-activated cell sorting
FDA	U.S. Food & Drug Administration
FDR	false discovery rate
FELASA	Federation of European Laboratory Animal Science Associations
FEW	family-wise error
Gapdh	glyceraldehyde 3-phosphate dehydrogenase
GFAP	glial fibrillary acidic protein
GO	gene ontology
GV-SOLAS	Die Gesellschaft für Versuchstierkunde
HD	Huntington's Disease
Hprt	hypoxanthine-guanine phosphoribosyltransferase
HTT	huntingtin
IB	inclusion body
Iba1	Allograft inflammatory factor 1
IFN	interferon

IFNAR	interferon alpha-beta receptor
IgG	Immunoglobulin G
ISG	interferon-stimulated gene
JAK	Janus kinase
JD	determinant of the Jacobian matrix
kDa	kilodalton
LPS	lipopolysaccharide
MG-HD	microglia-HD mice (details in section 4.2.1.3)
mHTT	mutant huntingtin
MRI	magnetic resonance imaging
mRNA	messenger ribonucleic acid
MSN	medium-spiny neuron
NDS	normal donkey serum
NGS	normal goat serum
NMDA	N-methyl-D-aspartate
Nr4a1	nuclear receptor subfamily 4 group A member 1
OF	open field
P2RY12	$P2Y_{12}$ receptor
PB	phosphate buffer
PCR	polymerase chain reaction
PET	positron emission tomography
PFA	parafolmaldehyde
polyA	polyadenylation
polyQ	polyglutamine
PSD-95	postsynaptic density protein 95
qPCR	quantitative polymerase chain reaction
R6/2	B6CBA-Tg(HDexon1)62Gpb/3J mice
REST/NRSF	repressor element 1/neuron restrictive silencing factor repressor complex
RNA	ribonucleic acid
RNAseq	RNA sequencing
rpm	rounds per minute
RT	room temperature
SD	standard deviation
SPF	specific pathogen-free
Spi1	gene encoding transcription factor PU.1
STAT	signal transducers and activators of the transcription
STR	stiatum
T2w	T2-weighted
TAE	Tris-acetate EDTA
TAM	tamoxifen
TBS	tris-buffered saline
TBS-T	TBS + 0.3 % Triton-X-100
TR-FRET	time-resolved fluorescence energy transfer
Ub	ubiquitin
v/v	volume/volume
WT	wild-type

List of Figures and Tables

1. Summary

Huntington's disease (HD) is a chronic, autosomal-dominant neurodegenerative disease that is caused by a CAG trinucleotide repeat expansion in exon 1 of the huntingtin gene. Progressive striatal atrophy and cortical thinning are commonly observed in HD, resulting in movement, psychiatric and cognitive impairments. It is generally thought that the increase in CAG repeats in the huntingtin gene leads to a toxic gain of function that results in the accumulation of nuclear and cytoplasmic inclusions and progressive neurodegeneration. The exact mechanisms of how mutant huntingtin causes neurotoxicity, however, remain unclear.

In the past years, both clinical and experimental evidence has emerged that points towards the involvement of the innate immune system in HD. In fact, an activated state of central nervous system (CNS) and peripheral myeloid cells precedes HD symptom onset in patients. Microglia - the resident parenchymal immune cells of the CNS - are phenotypically altered in both clinical and experimental settings of HD, but it is still not clear whether and how changes in microglia can contribute to HD pathogenesis.

To address this open question, two mouse models of HD were employed in this study. Firstly, the R6/2 mouse, which expresses a pathogenic human mHTT fragment in all cells of the body, was used to assess any changes that microglia undergo on a transcriptional level as a response to mHTT ubiquitous expression. The same model was used to deplete microglia and measure whether this could rescue disease progression. To take a closer look at the cell-autonomous effects mHTT has on microglia, I generated a novel mouse model in which the mHTT pathogenic fragment is targeted specifically to microglia (MG-HD). A series of cytometric, transcriptomic, imaging and behavioural analyses revealed that mHTT-expressing microglia display an activated phenotype *in vivo* in both mouse models. However, any cell-autonomous effects of mHTT on microglia observed in MG-HD mice were mild and transient and not sufficient to drive an HD-like neuropathological phenotype. Furthermore, depletion of microglia in the R6/2 mouse did not rescue the HD-like symptoms. The results suggest that microglia are affected in HD but are not primarily responsible for neurodegeneration.

Zusammenfassung

Die Huntington-Krankheit (HK) is eine chronische, autosomal-dominante neurodegenerative Erkrankung, die durch eine CAG Trinukleotidrepeatexpansion in Exon 1 des Huntingtin Gens verursacht wird. Bei HK Patienten werden oft progressive striatale Atrophie sowie kortikale Ausdünnung beobachtet, die zu Bewegungs-, psychiatrischen und kognitiven Störungen führen. Es wird vermutet, dass die Erhöhung der CAG Repeats im Huntingtin Gen zu einem toxischen Funktionszugewinn führt, der in der Folge für die Ansammlung von nukleären und zuytoplasmatischen Einschlusskörpern und für progressive Neurodegeneration verantwortlich ist. Die genauen Mechanismen, mit denen das mutierte Huntingtin Gen Neurotoxizität verursacht, sind jedoch bisher weitestgehend unbekannt.

Klinische und experimentelle Beweise der letzten Jahre deuten auf eine Beteiligung des angeborenen Immunsystems in der HK hin. Es konnte gezeigt werden, dass dem Auftreten der Symptome in Patienten ein aktivierter Zustand von Zentralnervensystem (ZNS) und peripheren Myeloidzellen vorangeht. Mikroglia – die hirneigenen parenchymalen Immunzellen des ZNS – sind sowohl in klinischen, als auch in experimentellen Formen der HK phänotypisch verändert. Noch ist jedoch unklar, ob und in wiefern Veränderungen der Mikroglia zur Pathogenese der HK beitragen.

Um diese Frage zu beantworten wurden in der vorliegenden Studie 2 Mausmodelle der HK eingesetzt. Zuerst wurde die R6/2 Maus, die in allen Körperzellen ein pathogenes menschliches mHTT-Fragment exprimiert, verwendet, um jegliche Veränderungen der Mikroglia auf transkriptionaler Ebene festzustellen, die als Folge der ubiquitären mHTT Expression auftreten. Das gleiche Modell wurde benutzt, um Mikroglia zu entziehen und um zu messen, ob der Entzug das Fortschreiten der Krankheit verhindern kann. Um die zellautonomen Effekte von mHTT auf Mikrolglia genauer zu untersuchen, habe ich ein neuartiges Mausmodell generiert, in dem das pathogene mHTT-Fragment spezifisch auf Mikroglia abgezielt ist (MG-HD). Eine Reihe von zytometrischen, transkriptomischen, bildgebenden und Verhaltensanalysen haben gezeigt, dass Mikroglia, die mHTT exprimieren, in beiden Mausmodellen einen aktivierten Phänotyp in vivo aufweisen. Jegliche zellautonome Effekte von mHTT auf Mikroglia, die in MG-HD Mäusen beobachtet wurden, waren jedoch mild und flüchtig, und nicht ausreichend, um einen HK-ähnlichen neuropathologischen Phänotyp hervorzurufen. Außerdem konnte der Entzug von Mikroglia in der R6/2 Maus die HK-ähnlichen Symptome nicht abschwächen. Diese Ergebnisse deuten darauf hin, dass Mikroglia in der HK zwar beeinträchtigt sind, dass sie aber nicht primär für die Neurodegeneration verantwortlich sind.

2. Introduction

2.1 Aetiology, epidemiology and clinical presentation of Huntington's disease

2.1.1 Aetiology of Huntington's Disease

Although genealogical studies have suggested the existence of Huntington's disease (HD) in America (and elsewhere) at least since the late seventeenth century, clear descriptions of hereditary chorea were only reported in the late nineteenth century and the disease was not generally recognised until a detailed description was published by George Huntington in 1872 (Lanska, 2000). In his original account, George Huntington described distinct features of the disease, i.e. its symptomatology, its hereditary nature, its gradual, midlife manifestation and its progressive course stating that 'Once it begins it clings to the bitter end' (Huntington, 1872).

HD is indeed a fatal monogenic neurological disorder caused by an autosomal, dominantly inherited mutation in the huntingtin gene (*HTT,* GeneBank accession number: NM_002111). This mutation in the IT15 gene on the short arm of chromosome 4 (4p16.3 locus) was discovered to be a CAG trinucleotide repeat expansion that translates to an abnormally long polyglutamine (polyQ) stretch at the N-terminus of the HTT protein (The Huntington's Disease Collaborative Research Group, 1993). People with greater than 39 repeats are certain to develop the disease within a normal lifespan (Pagan et al., 2017). Variable penetrance is observed in carriers of a CAG repeat expansion in the 36-39 repeat range, meaning that they may develop the disease in later life or not at all (Rubinsztein et al., 1996). Interestingly, subtle neurological abnormalities have been observed in some individuals with a CAG expansion in the range of 27-35, although this is not always the case (Pagan et al., 2017).

2.1.2 Epidemiology of Huntington's Disease

HD exists worldwide, but the prevalence of HD can vary across ethnic groups and, therefore, the global incidence of HD remains unclear. This variance depends on the extent of the CAG expansion at the *HTT* locus within different populations. For example, people with East Asian ancestry have an average of 17.5-17.7 CAG repeats while people with African and European ancestry have an average of 16.9-17.4 and 18.4-18.7 repeats, respectively. Prevalence studies that took both genetic testing and neurological evaluations into account showed that 10.6-13.7 individuals per 100,000 are affected with HD in the Western world. 'Pockets' of particularly high prevalence have been identified in the Maracaibo region of Venezuela, where hundreds of related

patients were traced back to a single ancestor and, on the contrary, a much lower incidence (1-7 per million) has been documented in Japan, Taiwan and Hong Kong (Bates et al., 2015 and Kay et al., 2017).

When passed from parent to child, CAG repeat length may expand, contract, or be stably transmitted. Intermediate length alleles (27-35 CAG repeats) are prone to stepwise expansion of the CAG repeat length due to germline CAG instability resulting in earlier disease onset, a process termed *anticipation*. Anticipation - i.e. CAG repeat length expansion observed over successive generations - is seen when the mutation is passed down through the paternal line, since male sperm shows greater repeat variability and larger repeat sizes than somatic tissues (Telenius et al., 1994 and Semaka et al., 2013).

2.1.3 Clinical presentation of Huntington's Disease

Huntington's disease presents as a combination of motor, cognitive and/or psychiatric symptoms that progress over 15 to 20 years and eventually result in death (Bates et al., 2015). As previously implied, the extent of the CAG expansion inversely correlates with the age of onset of HD. Carriers of 36-39 CAG repeats may never develop HD, while, in the rare occurrence of a CAG repeat length above 55, juvenile HD can occur with an age of onset younger than 20 years of age. In typical cases of HD, onset occurs mid-life (45 years of age on average) and is clinically defined by the presence of definite motor signs. For about 10-15 years prior to 'manifest-HD' onset, patients experience 'prodromal' symptoms (Ghosh and Tabrizi, 2018). In both the prodromal and the manifest stages of HD, symptoms are heterogeneous among patients both in terms of their balance and in terms of their nature. This clinical variability is especially clear in monozygotic twins that have identical HD genes but clear differences in their symptomatology (e.g. Georgiou et al., 1999, Friedman et al., 2005 and Gómez-Esteban et al., 2007).

The most common and perhaps most striking motor symptom of HD is chorea, defined as short-lived, involuntary, excessive movements, which are semi-purposeful and resemble dancing motions – thus the name, *chorea*, from the Greek word *χορεία* which means dance (Ghosh and Tabrizi, 2018). Chorea is one of many motor disturbances observed in HD patients, and cognitive and psychiatric symptoms can be just as variable. To shed light on the commonalities and differences HD symptomatology across patients, various largescale multi-center studies were performed. For example, the REGISTRY (Orth et al., 2010), COHORT (Huntington Study Group COHORT Investigators and Dorsey, 2012) and PHAROS (Kayson et al., 2019) trials tracked

motor, cognitive and behavioral variables in HD while the PREDICT, TRACK-HD and Track-On HD trials have focused on narrower questions regarding the transition from the pre-manifest to the manifest stage (Paulsen et al., 2014, Tabrizi et al., 2012 and Klöppel et al., 2015, respectively). Detailed descriptions of the clinical features of HD are offered by McColgan and Tabrizi, 2018 and Ghosh and Tabrizi, 2018.

2.2 Pathobiology of Huntington's Disease

2.2.1 Mutant huntingtin – a toxic gain-of-function

Native huntingtin is a 348 kDa protein (polyQ repeat length of 23) that is expressed throughout the human body at different levels depending to the cell type (Gutekunst et al., PNAS 1995). It is proteolytically processed and located both in the cytoplasm and in the nucleus. It's normal function is still not entirely understood but it appears to act in several key cellular mechanisms that include microtubule-based transport, F-actin-based trafficking, Rab11 function and the transport of Rab proteins, BDNF transport, ciliogenesis, transcription and chromatin modification, regulation of post-transcriptional gene expression, neurogenesis, synaptogenesis and synaptic plasticity, cell signaling, cellular responses to stress, selective macroautophagy and DNA-damage repair (Liu and Zeitlin, 2017). Mice that are null for the murine *HTT* homolog do not survive past embryonic day 8.5, indicating that the protein is developmentally indispensable (Duyao et al., 1995, Nasir et al., 1995 and Zeitlin et al., 1995). Furthermore, expression of mutant HTT (mHTT) results in neurodevelopmental defects in human fetuses (Barnat et al., Science 2020). HTT may also play a role in central nervous system (CNS) maintenance since the selective depletion of *HTT* in the CNS during embryogenesis or soon after birth results in progressive neurodegenerative phenotypes in adult mice (Dragatsis et al., 2000 and Dietrich et al., 2009). Interestingly, the selective ablation of *HTT* in the adult murine brain does not result in overt motor and neuropathological deficits (Wang et al., 2016), which suggests that the disease does not result solely from the loss of HTT function. Indeed, HD is primarily a toxic gain-of-function disease where novel actions of huntingtin are brought on by the polyQ repeat expansion. This is further supported by the fact that HD shares many features with other incapacitating neurodegenerative disorders - e.g. spinobulbar muscular atrophy and the spinocerebellar ataxias - that result from trinucleotide expansions elsewhere in the genome (reviewed in: Orr and Zoghbi, 2007).

2.2.2 Molecular pathogenesis of Huntington's Disease: cell-autonomous mechanisms of mutant huntingtin toxicity

Even though it is anticipated that increased CAG repeats in *HTT* result in a toxic gain of function of mHTT and subsequent neurotoxicity, the multiple mechanisms through which mHTT activates its pathogenic cascade are complex and remain somewhat unclear. Initial work in the field of HD identified striatal medium-spiny neurons (MSNs) and, at later stages, cortical pyramidal neurons as being particularly vulnerable to degeneration caused by mHTT (Reiner et al., 1988). In line with this, progressive striatal atrophy and cortical thinning are consistently observed in HD patients (Niccolini and Politis, 2014). But how does the mutant protein actually cause this neuronal degeneration and how can the vulnerability of particular neuron subtypes be explained?

Early studies in HD mouse models identified intraneuronal aggregates of mHTT as a pathognomic feature of HD (Davies et al., 1997) and this finding was upheld in histological assessments of HD patient brains (DiFiglia et al., 1997). It led scientists to hypothesize that the identified mHTT- and ubiquitin- immunoreactive inclusion bodies (IBs) might actually cause HD. However, while some studies have implied a pathogenic role of IBs in HD, others have indicated that IB formation is one of the coping mechanisms of cells (together with the ubiquitin-proteasome and autophagy systems) that might help to reduce the levels of diffuse, toxic mHTT (Arrasate and Finkbeiner, 2012).

While the definitive role of IBs in HD is not yet clear, multiple lines of evidence support an alternative mechanism as the elicitor the mHTT-induced pathogenic cascade. The "toxic fragment hypothesis" states that the toxicity of mHTT is not caused by its aggregation but rather by its fragmentation. mHTT fragmentation is either the result of proteolytic cleavage of the protein due to a conformational change elicited by the polyQ stretch (Kim, 2013) or the result of alternative splicing of exon 1 of *HTT* due to the CAG repeat expansion (Sathasivam et al., 2013). Of the mHTT fragments released, N-terminal fragments that contain the polyQ stretch are particularly toxic. They activate additional proteolytic caspases leading to further fragmentation and tend to accumulate, generating fibrils that can cause cellular dysfunction similar to amyloid or α-synuclein structures in Alzheimer's or Parkinson's disease (Ross and Poirier, 2004). In both Drosophila and mouse models of HD, expression of human *mHTT* exon 1 (the toxic N-terminal fragment) is sufficient to cause overt neurological phenotypes (Barbaro et al., 2015 and Mangiarini et al., 1996). According to this evidence, it seems that soluble misfolded monomers or small soluble oligomeric species of mHTT are sufficient to cause cellular dysfunction or even cell death (Ross et al., 2017).

A number of different cellular functions are interrupted by mHTT. One key mechanism affected is the clearance of mHTT by the ubiquitin-proteasome and autophagy systems, leading to altered proteostasis and the gradual accumulation of the toxic protein and its fragments (Bennett et al., 2007 and Martinez-Vicente et al., 2010). The accumulation of aberrant mHTT species results in their binding to various other proteins, altering their function. One such downstream effect is transcriptional dysregulation. mHTT accumulates in the nucleus affecting key transcription factors such as CREB-binding protein (CBP) (Steffan et al., 2000) and repressor element 1/neuron restrictive silencing factor repressor complex (REST/NRSF) (Zuccato et al., 2003). It inhibits histone acetyltransferase activity, causing chromatin condensation and transcriptional downregulation (Butler and Bates, 2006).

Importantly, mHTT also interferes with the expression of brain-derived neurotrophic factor (BDNF) through the loss of binding of the mutant protein to REST/NRSF (Zuccato et al., 2001). BDNF is an important neuromodulator and trophic factor that promotes the survival of striatal medium spiny neurons. It is produced by the cerebral cortex and anterogradely transported along the corticostriatal tract to striatal MSNs. Yet, the reduced level of striatal BNDF observed across animal models of HD and in HD patient tissue is only partly due to its transcriptional depletion caused by mHTT (Zuccato and Cattaneo, 2009). Native HTT has been shown to regulate vesicle transport and recycling and the expression of the mutant form of the protein disrupts these processes (Pardo et al., 2010, Li et al., 2003). The interruption of cytoskeleton signaling and vesicular trafficking caused by mHTT affects the vesicular transport of BDNF from the cortex to the striatum, thus contributing to the decreased BDNF levels observed in HD striata (Gauthier et al., 2004, Roux et al., 2012). Interestingly, genetically engineered mice lacking BDNF expression in the cortex developed brain atrophy, motor dysfunction and gene expression abnormalities similar to those observed in HD mouse models (Baquet et al., 2004 and Strand et al., 2007). These findings further implicated reduced cortical BDNF support as a major pathway contributing to striatal degeneration in HD.

In addition to the pathogenic mechanisms outlined above, mitochondrial dysfunction has also been observed in HD (Polyzos and McMurray, 2017). mHTT disrupts mitochondrial function indirectly, by interfering with axonal transport of the organelles, and directly, by impairing the transcription of nuclear genes necessary for mitochondrial calcium handling and respiration (Jin and Johnson, 2010). An overview of pathogenic cellular mechanisms in HD can be found in **Figure 1**.

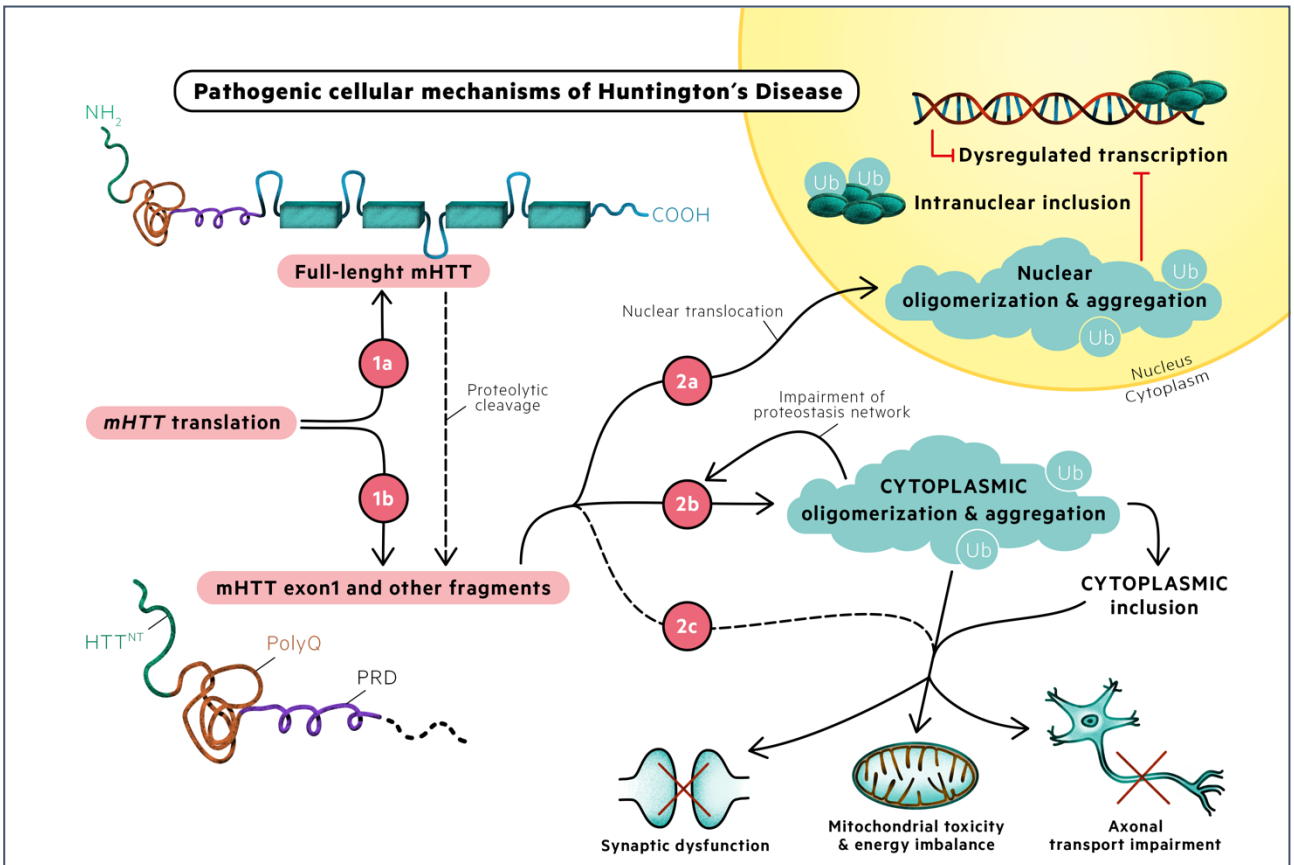

Figure 1 | **Pathogenic cellular mechanisms in Huntington's disease (adapted from Bates et al., 2015).** Translation of *mHTT* can give rise either to full-length mHTT (1a) or to exon1-mHTT and other fragments as a result of aberrant splicing of exon 1 of *mHTT* due to the CAG repeat expansion (1b). Full-length mHTT undergoes proteolytic cleavage to generate additional protein fragments. mHTT protein fragments can translocate to the nucleus (2a), where oligomerization and aggregation of the protein occurs which results in the formation of intranuclear inclusions that interfere with transcription. Cytoplasmic mHTT fragments either interfere directly with cellular processes (2c) or they self-associate, causing cytoplasmic oligomerization and the formation of protein aggregates in the cytoplasm that can also interfere with cellular functions (2b). Interference of various mHTT forms with cellular processed can cause global cell impairments that include synaptic dysfunction, mitochondrial damage and a decrease in the efficiency of axonal transport. PRD: Proline rich domain; Ub: ubiquitin. HTT^{NT}: huntingtin N-terminal sequence.

2.2.3 Involvement of non-neuronal cells in HD pathology

Many of the cellular processes affected in HD cannot be attributed entirely to the expression of mHTT in MSNs and are not even restricted to the corticostriatal system. For instance, excitotoxicity, that has long been implicated in the pathogenesis of HD, is caused by excessive stimulation of N-methyl-D-aspartate (NMDA) receptors due to excessive exposure to glutamate. This increase in striatal glutamate levels comes from corticostriatal inputs, but it is also due to the inadequate uptake of excess glutamate in the synaptic cleft by astrocytes through the glutamate

transporter (Gray, 2019). To get a more complete understanding of HD pathology, efforts in the last years have focused on understanding how non-cell-autonomous mechanisms contribute to HD (reviewed in: Creus-Muncunill and Ehrlich, 2019).

Most studies aimed at deciphering non-cell-autonomous alterations caused by mHTT have utilized mouse lines with targeted expression or deletion of mHTT in specific cell types or brain regions. Initially, mHTT expression was targeted or deleted from vulnerable neuronal subtypes and, interestingly, not all features of the murine HD phenotype were recapitulated or rescued respectively. The specific expression of mHTT in MSNs resulted in mHTT accumulation and minor glutamatergic NMDA receptor alterations but did not result in overt motor deficits (Gu et al., 2007), while deleting mHTT expression in striatal cells in the BACHD pan-cellular model of HD only mildly improved the disease phenotype in terms of motor deficits, behavioural symptoms and neurodegeneration (Wang et al., 2014). Similarly, when mHTT expression was targeted to cortical projection neurons, mHTT aggregation occurred in cortical neurons but no electrophysiological or motor abnormalities were observed (Gu et al., 2005) and, again, deleting mHTT expression in cortical pyramidal neurons in the BACHD model of HD improved some, but not all of HD-like phenotypes (Wang et al., 2014). Combining mHTT deletion in both striatal MSNs and cortical pyramidal neurons resulted in the greatest improvement of the HD-like phenotype, but the disease was not entirely reversed (Wang et al., 2014). These results suggest a possible contribution from other cell types of the brain such as glia, that are normally responsible for maintaining a healthy neuronal milieu.

The intrinsic properties of glial cells render them vulnerable to unique types of dysfunction and research in the past years has focused on understanding their role in HD pathology. For example, selectively expressing mHTT in astrocytes resulted in striatal neuron death *in vitro* (Shin et al., 2005) and decreased survival, neurological deficits, weight loss and reactive gliosis *in vivo* (Bradford et al., 2009). These effects resulted, at least in part, from reduced glutamate transporter (Faideau et al., 2010) and Kir4.1 potassium ion channel expression in mHTT-expressing astrocytes (Tong et al., 2014). The selective expression of mHTT in oligodendrocytes also caused progressive neurological symptoms, age-dependent demyelination, decreased expression of myelin genes and decreased survival of mice (Huang et al., 2015).

While important findings have emerged from looking at astrocyte and oligodendrocyte contributions to the pathobiology of HD (reviewed in: Gray, 2019 and Creus-Muncunill and Ehrlich, 2019), this study focuses on the particular role of microglia, the resident innate immune cells of the CNS.

2.3 The role of microglia in Huntington's Disease

2.3.1 Microglia in the developing brain

Microglia are part of the mononuclear phagocyte system and, in mice, they arise from c-Kit^{lo}CD41^{lo} erythro-myeloid progenitors in the primitive yolk sac at embryonic day 7.25 (Ginhoux et al., 2010 and Prinz et al., 2019). These pre-macrophages migrate into the bloodstream and travel through the vascular system to eventually seed the brain rudiment (Ginhoux et al., 2010 and Stremmel et al., 2018). Under homeostatic conditions in the adult CNS, microglia can be long-lived (Askew et al., 2017 and Réu et al., 2017) and have the capacity to self-renew locally and independently of bone-marrow driven cell-replenishment (Ajami et al., 2007 and Mildner et al., 2007).

The microenvironment in which microglia reside varies greatly from one developmental stage to the next. This means that microglia need to adapt to the different functional demands of their surrounding tissue, which is reflected in distinct transcriptomic signatures of embryonic, early postnatal and adult microglia (Matcovitch-Natan et al., 2016 and Masuda et al., 2019). Until the first post-natal week, microglia have an amoeboid morphology and undergo proliferation at rates much higher than those observed in the adult CNS (Askew et al., 2017, Kierdorf et al., 2013 and Réu et al., 2017). Microglia arise at around the same time as neural precursors, when other glia are still absent, and they play a central role in development of the intricate CNS architecture. More specifically, they regulate the number and the fate of neural precursors in the embryonic and early post-natal CNS by stimulating or preventing their apoptosis, by phagocytosing dead or dying cells, by directing neural differentiation and by providing trophic support for developing astrocytes, oligodendrocytes and vasculature (Frost and Schafer, 2016). Furthermore, microglia contribute to the establishment of functional neural circuits by guiding the wiring of the developing brain and by regulating synapse remodelling, which involves microglia-mediated engulfment of inactive synapses and microglia-mediated prevention of excessive pruning (Prinz et al., 2019).

2.3.2 Microglia in the adult brain

Microglia in the adult CNS that reside behind a mature blood-brain barrier (BBB) are quite different from their embryonic and early post-natal counterparts and this is reflected in their distinct transcriptomic profile (Matcovitch-Natan et al., 2016; Masuda et al., 2019). In post-natal steady state conditions, microglia switch from expansion to homeostatic proliferation by which a remarkably steady population is maintained through adulthood (Askew et al., 2017). They account

for 5-12% of glia in the adult mouse brain (Lawson et al., 1990) and for 0.5-16.6% of the total cell number in the adult human brain depending on the region examined (Mittelbronn et al., 2001). At any given time-point, 0.075%-1.04% of microglia are proliferating in the adult mouse (Askew et al., 2017, Lawson et al., 1992, Shankaran et al., 2007 and Tay et al., 2017), while in humans, their daily median renewal rate was estimated to be 0.08% (Réu et al., 2017).

Early research described regional heterogeneity of microglia with distinct cell distributions and morphologies according the brain region examined (Lawson et al., 1990). This was confirmed in a recent study that used advanced morphological modelling to describe microglia morphometric heterogeneities (Verdonk et al., 2016). Microglia heterogeneity was also detected in recent genomic studies (Grabert et al., Nat Neurosci 2016; Ayata et al., Nat Neurosci 2018; Sankowski et al., Nat Neurosci 2019) and mass cytometric studies (Böttcher et al., Nat Neurosci 2019). However, it is still not clear whether morphological and distributional heterogeneities of microglia in different brain regions reflect an environment-specific functional imprint or rather a spectrum of transient activation states of these cells (Kettenmann et al., 2013 and Prinz et al., 2019).

In general, unchallenged or "resting" microglia in the adult brain have relatively static cell somata from which long processes extend with fine ramifications. Their processes constantly lengthen and retract, allowing them to dynamically scan an area more than ten times larger than their own cell body (Davalos et al., 2005 and Nimmerjahn et al., 2005) and establish frequent transient contacts with neighbouring neurons and astrocytes (Kettenmann et al., 2013). As the resident innate immune cells of the CNS, the main role of microglia is to sense and respond to damage. However, even in the absence of any pathological insult, microglia still function as the resident phagocytes of the CNS responsible for routine, non-inflammatory clearance of dead brain cells. For instance, in neurogenic areas of the hippocampus where only a fraction of new-born neuroblasts mature into neurons, microglia engage in apoptosis-coupled phagocytosis that maintains the homeostasis of the baseline neurogenic cascade (Sierra et al., 2010). There is also emerging evidence of microglia playing a role in plasticity in the adult CNS. Resting microglia make multiple transient contacts with synapses (Tremblay et al., 2010 and Paolicelli et al., 2011) and, upon contact, they can sense the condition of the synapse and are able to engulf and phagocytose presynaptic terminals or postsynaptic spines in a process termed synaptic remodelling or pruning (Kettenmann et al., 2013 and Wake et al., 2013).

Perhaps the most characteristic feature of microglia that was already described the Spanish neuroscientist Pío del Río Hortega in the early 20th century is their transformation in response to CNS pathology. As primary effector cells of the CNS, they rapidly respond to changes in the CNS

microenvironment and shift into an "activated" state. This shift, termed reactive microgliosis, occurs as a continuum of changes in gene expression, morphology, motility, migration, metabolism, sensome, secretome, phagocytosis, proliferation and death that depend upon the type and the stage of the CNS insult (Prinz et al., 2019).

2.3.3 Current understanding of the role of microglia in Huntington's disease

Persistent microglial activation and the sustained release of proinflammatory factors are observed in several neurodegenerative diseases (Prinz et al., 2019). However, it is still unclear whether microglial activation occurs as a response to neuronal dysfunction and/or represents a cell-autonomous phenotype of dysfunctional microglia that can actually cause or contribute to neurodegenerative pathologies (Aguzzi et al., 2013). In the context of HD, the evidence of neuronal dysfunction occurring as a result of mHTT expression is unequivocal and extensive (see section 2.2). At the same time, changes in microglia as a response to mHTT have also been demonstrated both in patients and in mouse models of HD, an overview of which can be found in **Figure 2**.

2.3.3.1 Evidence of microglia changes in HD patients

Post-mortem neuropathological assessment of the HD brain and positron emission tomography (PET) in individuals with HD have shown that microglial activation is an early event in HD pathology (Sapp et al., 2001, Tai et al., 2007 and Politis et al., 2015). It can be observed in patients up to 15 years before the predicted age of onset and persists as the disease progresses, directly correlating with striatal dopamine D2 receptor dysfunction and disease severity (Pavese et al., 2006 and Tai et al., 2007). In the brains of patients with HD, microglia acquire an altered "dystrophic" morphology (Sapp et al., 2001) and progressively accumulate the iron storage protein ferritin, possibly indicating disturbances in iron regulation (Simmons et al., 2007). In addition, mHTT nuclear inclusions were recently identified in post-mortem HD microglia - albeit in lower proportions than in neurons, suggesting that the cell-autonomous dysfunction imposed by mHTT on neurons could also apply to microglia (Jansen et al., 2017).

Markers of oxidative stress such as protein carbonyls are increased in the HD brain, as are other antioxidant defence proteins such as peroxiredoxins and glutathione peroxidases (Sorolla et al., 2008). Furthermore, there is evidence of increased reactive nitrogen species and iron, a metal

involved in reactive oxygen species generation, both accumulating in the brains of HD patients (Browne et al., 1997 and van den Bogaard et al., 2013). These effects could be directly linked with metabolic dysfunction caused by mHTT or could, alternatively, be a reflection of concomitant processes such as inflammation.

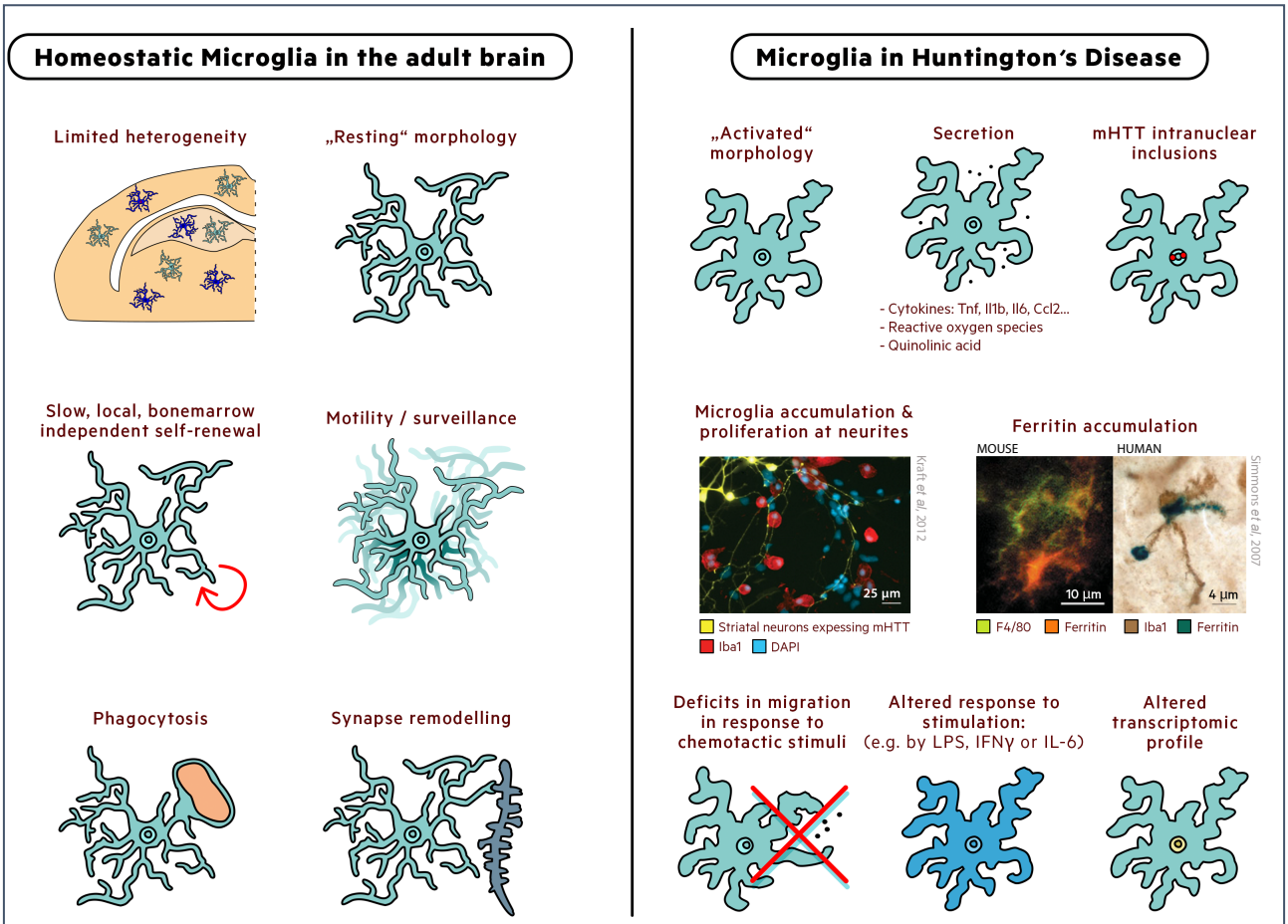

Figure 2 | **Microglia in the adult homeostatic and the HD brain**. **Left:** Features of microglia in the homeostatic brain include limited heterogeneity across brain regions, a "resting" morphology with thin, ramified processes and small somata and slow, local, bone marrow independent self-renewal. Microglia in the healthy brain are highly motile and they constantly scan the surrounding tissue for damage. They are able to phagocytose damaged or dead cells and they play a role synapse remodelling. (adapted from Prinz et al., 2019). **Right:** Microglia in the adult HD brain adopt an "activated" morphology with enlarged somata and short, thick processes. They secrete various molecules in response to mHTT toxicity such as pro-inflammatory cytokines, reactive oxygen species and quinolinic acid. Furthermore, mHTT intranuclear inclusions have been observed in a fraction of both mouse and human HD microglia. "Healthy" microglia ($Iba1^+$ cells) transplanted onto corticostriatal cultures in which mHTT was expressed in neurons accumulated and proliferated around neurites (Kraft et al., 2012). In addition, microglia ($Iba1^+$ or $F4/80^+$) have been shown to accumulate ferritin in mouse models of HD and in human microglia (Simmons et al., 2007). Finally, microglia that express mHTT exhibit deficits in migration in response to chemotactic stimuli, altered responses to various forms of stimulation and an altered transcriptional profile. Details and references of these findings can be found in **sections 2.3.3.1 and 2.3.3.2**.

HD patients show increased levels of various inflammatory molecules (e.g. IL-6, IL-8 and TNFα) in the striatum, cortex, cerebellum and cerebrospinal fluid (Björkqvist et al., 2008 and Silvestroni et al., 2009). In addition, a study that examined mRNA expression profiles of whole-tissue prefrontal-cortex homogenates from 20 HD patients revealed a prominent enrichment of genes involved in innate immune responses and neuroinflammation (Labadorf et al., 2015). Elevated levels of inflammatory molecules have also been documented in patient blood plasma and they correlate with disease progression in HD (Silajdžić and Björkqvist, 2018). Interestingly, mHTT fragment levels in monocytes have been significantly associated with disease burden score and caudate atrophy rates in HD patients, which suggests a potential relevance of mHTT expression in the periphery to pathogenic and clinical events in the CNS (Weiss et al., 2012). It therefore might be the case that elevated cytokine levels in the HD brain originate from peripheral blood plasma due to leakage of the BBB in HD (Drouin-Ouellet et al., 2015), although the generally accepted opinion is that cytokines are rapidly broken down after their release in peripheral blood and there is currently no evidence of infiltration of circulating innate or adaptive immune cells in post-mortem HD brain samples (Silvestroni et al., 2009).

2.3.3.2 Further insights on the role of microglia in HD from animal models

The immune cell dysregulation observed in HD patients is recapitulated in commonly used mouse models of the disease. An overview of different HD mouse lines and whether they were checked for microglia changes can be found in Creus-Muncunill & Ehrlich, 2019. Most importantly, mHTT nuclear inclusions were identified in cortical and striatal microglia of three different HD mouse lines (Jansen et al., 2017) and age-dependent changes in striatal microglial morphology were reported in mouse models of HD (Franciosi et al., 2012). The increased proinflammatory cytokine profile observed in HD patient blood has also been documented in R6/2 mouse serum (Björkqvist et al., 2008) and, in mice, an increased secretion of inflammatory molecules in the brain has specifically been attributed to microglia (Crotti et al., 2014).

Experimental work on animal models of HD has provided further insight into the specific effects that mHTT expression in neurons has on microglia. In primary neuronal cultures and corticostriatal brain slices from rats and mice with selective mHTT expression in neurons, microglia accumulated around irregular neurites and proliferated, adopting an amoeboid morphology (Kraft et al., 2012). A mechanism for neuron-driven microglia activation was proposed by Khoshnan *et al*. who showed that mHTT expression in neurons results in neuronal IL-34 secretion, which is a major

driver of microglial expansion (Khoshnan et al., 2017). These studies provide evidence of non-cell autonomous mechanisms of microglia activation in HD, with microglia responding to the neuronal mHTT-induced dysfunction.

At the same time, there is accumulating evidence of cell-autonomous microglial dysfunction that comes from mHTT expression in microglia themselves. For instance, microglia isolated from YAC128 transgenic mice that express the full-length human mHTT exhibit deficits in migration towards chemotactic stimuli (Kwan et al., 2012). In addition, microglia isolated from R6/2 transgenic mice expressing exon 1 of human mHTT are hyperactive in response to combined interferon-γ and lipopolysaccharide (LPS) stimulation (Björkqvist et al., 2008). A recent study refined the latter observation by showing that different stimuli elicit different but genotype-specific responses in mHTT-expressing microglia (Donley et al., 2019). The response of mHTT-expressing microglia to LPS stimulation was dampened compared to controls, while, on the contrary, the same cells exhibited a potentiated response to IL-6 stimulation (Donley et al., 2019). Furthermore, the exaggerated cytokine release of microglia expressing mHTT in response to certain inflammatory stimuli seems to be a cell-autonomous response, since it does not occur when microglia overexpress native HTT and it can fully be rescued by knocking-down mHTT (Connolly et al., 2016).

Various molecular mechanisms have been proposed to mediate microglial altered states in HD that include activation of the NFκB signaling cascade (Khoshnan and Patterson, 2011), the cannabinoid receptor pathway (Palazuelos et al., 2009), the kynurenine pathway (Giorgini et al., 2008) and P2X7 receptor signalling (Díaz-Hernández et al., 2009). A recent study proposed a molecular mechanism for the cell-autonomous activation of microglia as a response to mHTT expression that involves increased transcriptional activities of the myeloid lineage-determining factors PU.1 and CCAAT-enhancer binding protein (C/EBP)-α,β (Crotti et al., 2014). mHTT expression in cultured microglia resulted in increased expression genes adjacent to PU.1 and (C/EBP)-α,β, such as *Il6* and *Tnfa,* further advocating for autonomous activation of mHTT-expressing microglia that is independent of neuronal stimuli.

There is currently enough data from human patients and animal models of HD to suggest that mHTT expression affects microglial functions. Nevertheless, the question of whether these responses are neurotoxic and can contribute to the pathogenesis of HD has not been answered. Interestingly, mHTT-expressing microglia exerted toxicity on wild-type neurons *in vivo* only when combined with intraventricular LPS-induced neuroinflammation (Crotti et al., 2014).

There is no current treatment available for the management of HD progression and, therefore, understanding cell type-specific contributions to HD could potentially uncover treatment targets. It has already been shown in mouse models of HD that dampening the response of microglia can be protective (Paldino et al., 2019 and Siew et al., 2019). The current study attempts to uncover whether and how the expression in mHTT in microglia can contribute to HD pathogenesis.

3. Aims of the study

Considering the mounting evidence of an altered state of microglia in HD along with the fact that the involvement of microglia in neurodegeneration is poorly understood, the question of whether and how microglia contribute to neurodegeneration and HD pathogenesis remains to be resolved. Here, a mouse model of HD with ubiquitous expression of mHTT and a mouse model with selective targeting of the mutant protein to microglia are employed to address the following key questions:

1. What are the changes of microglia in HD?

2. Which of the changes observed in microglia in HD are cell-autonomous?

3. Do changes in microglia contribute to HD pathogenesis?

4. Materials & Methods

4.1 Materials

4.1.1 Animals

Strain	Provider	Stock No	Reference
B6.129-*Gt(ROSA)26Sor*$^{tm1(HD*103Q)Xwy}$/J	The Jackson Laboratory	007708	(Gu et al., 2005)
B6CBA-Tg(HDexon1)62Gpb/3J	The Jackson Laboratory	006494	(Mangiarini et al., 1996)
B6CBAF1/J	The Jackson Laboratory	100011	
C57Bl/6J	The Jackson Laboratory	005304	
Cx3cr1$^{tm2.1(cre/ERT2)Jung}$/J	The Jackson Laboratory	020940	(Yona et al., 2013)

4.1.2 Veterinary drugs and anaesthetics

Product	Provider
Isoflurane	Forene, Abbott
Ketamine Hydrochloride	Pfitzer, Pharmacia GmbH
Xylazine Hydrochloride	Bayer AG

4.1.3 Chemicals and reagents

Product	Provider
2-log DNA ladder	New England BioLabs
4‘,6‘-Diamidino-2-Phenylindole (DAPI)	Sigma-Aldrich
50 bp DNA ladder	New England BioLabs
Ampuwa distilled water	Fresenius Kabi Deutschland GmbH
Agarose NEEO Ultra-Qualität	Roth
BLZ945 (CSF-1R inhibitor)	Novartis
Bovine serum albumin (BSA)	Sigma-Aldrich
Chloroform	Sigma-Aldrich
Corn Oil	Sigma-Aldrich
D-(+)-Glucose	Sigma-Aldrich

Decosept AF	Dr. Schumacher GmbH
Diethyl dicarbonate (DEPC)	Roth
dNTP-Mix	Promega
Ethanol (absolute)	J.T. Barker
Ethylenediaminetetraacetic acid (EDTA) (E6511)	Sigma-Aldrich
FluorSave Reagent®	Merck
Gel Loading Dye, Orange (6X)	Biolabs
GelRed®	Biotium Inc.
Hematoxylin Solution, Mayer's	Sigma-Aldrich
Isopropanol	Sigma-Aldrich
Linear acrylamide, AM9520	Ambion
Normal donkey serum (NDS)	Biozol
Paraformaldehyde, pure	Roth
Percoll® (GE17-0891-02)	Sigma-Aldrich
Phenol:Chloroform:Isoamyl Alcohol (25:24:1)	Invitrogen
Radom primers (Invitrogen™, 48190011)	Thermo Fisher Scientific
Random Primers	Promega
RQ1 DNase stop solution	Promega
RQ1 DNase, RNase free	Promega
RQ1 RNase-Free DNase	Promega
Sodium hydroxide	Roth
Sodium acetate (C2H3NaO2)	Roth
Sodium azide	Roth
Sodium bicarbonate (NaHCO3)	Roth
Sodium chloride	Roth
Sodium citrate	Roth
Sucrose	Sigma-Aldrich
Tamoxifen	Sigma-Aldrich (T5648)
Tris-Base	Sigma-Aldrich

Triton-X-100	Sigma-Aldrich
TRIzol™ Reagent	Thermo Fisher Scientific
Tween 20	Sigma-Aldrich

4.1.4 Media and buffers

Name	Provider
0.2 M Phosphate Buffer (PB), pH 7.4	1 l ddH_2O 21.8 g Na_2HPO_4 6.4 g NaH_2PO_4
4% PFA in PB, pH 7.4	225 ml ddH_2O 250 ml 0.2 M PB 20 g PFA add 1M NaOH until clear
BD Pharm Lyse™	BD Biosciences
DEPC-H2O	1 ml DEPC in 1 l H_2O
Gibco® Dulbecco's Phosphate Buffered Saline (DPBS)	Thermo Fisher Scientific
Gibco® High Glucose DMEM	Thermo Fisher Scientific
Modified PBS	10 ml DPBS 0.1g D-Glucose 0.07g $NaHCO_3$ 90 ml ddH_2O
Sodium Citrate Buffer	10mM Sodium Citrate 0.05% Tween 20 pH=6.0
Sorting buffer	1 x DPBS 2 mM EDTA 0.5 % BSA w/v 900 ml ddH_2O
TAE Buffer (50x), pH 7.8	121.1 g Tris-Base

	10.25 g $C_2H_3NaO_2$
	50 ml 0.5 mM EDTA in ddH_2O
TBS, pH 7,4	42 mM Tris HCl
	8 mM Tris Base
	154 mM NaCl
TBST	TBS
	0.3 % Triton-X-100

4.1.5 PCR primers sequences

4.1.5.1 Conventional PCR primer sequences

Mouse strain	Primer sequences	Product size
B6.129-*Gt(ROSA)26Sor*$^{tm1(HD*103Q)Xwy}$/J	5‘- GCGAAGAGTTTGTCCTCAACC-3‘	Wt: 603 bp
	5‘-AAAGTCGCTCTGAGTTGTTAT-3‘	Ho: 300 bp
	5’- GGAGCGGGAGAAATGGATATG-3’	
B6CBA-Tg(HDexon1)62Gpb/3J	5’-CCGCTCAGGTTCTGCTTTTA-3’	172 bp
	5’-GAGTCCCTCAAGTCCTTCCA-3’	
Cx3cr1$^{tm2.1(cre/ERT2)Jung}$/J	5’-CCTCTAAGACTCACGTGGACCTG-3’	Wt: 692 bp
	5’-GACTTCCGAGTTGCGGAGCAC-3’	Ho: 304 bp
	5’-GCCGCCCACGACCGGCAAAC-3’	

4.1.5.2 qPCR primer sequences

Gene	Primer sequences	Product size
Human *Htt*	5’-GTGCTGAGCGGCGCCGCGAGTC-3’	114 bp
	5’-GGACTTGAGGGACTCGAAGGC-3’	
Murine *Actb*	5’-ACCCACACTGTGCCCATCTA-3’	342 bp
	5’-GCCACAGGATTCCATACCCA-3’	
Murine *Bdnf*	5’- CCTCCTCTACTCTTTCTGCTG-3’	299 bp
	5’- TGCCTTTTGTCTATGCCCC-3’	
Murine *Drd1*	5’- ATGGCTCCTAACACTTCTACCA-3’	124 bp

	5’- GGGTATTCCCTAAGAGAGTGGAC-3’	
Murine *Drd2*	5’-AAGCGTCGGAAGCGGGTCAAC-3’	174 bp
	5’- TCGGCGGGCAGCATCCATTCT-3’	
Murine *Gapdh*	5’-AGATTGTCAGCAATGCATCCTGC-3’	348 bp
	5’- CCAAGTATGATGACATCAAGAAGG-3’	
Murine *Hprt*	5’-GTTATTGGTGGAGATGATCTCTC-3’	230 bp
	5’-GGCATATCCAACAACAAACTTGTC-3’	
Murine *Nr4a1*	5’- AGCTTGGGTGTTGATGTTCC-3’	111 bp
	5’- AATGCGATTCTGCAGCTCTT-3’	

4.1.6 Antibodies

4.1.6.1 Antibodies for flow cytometry

Antigen	Working conc. (µg/ml)	Product no.	Provider	Clone
mouse CD11b	2	101212	Biolegend	M1/70
mouse CD11c	2	117323	Biolegend	N418
mouse CD16/CD32	5	101320	Biolegend	clone 93
mouse CD3	5	100214	Biolegend	17A2
mouse CD45	5	103108	Biolegend	30-F11
mouse Ly6C	2	128012	Biolegend	HK1.4
mouse Ly6G	2	127618	Biolegend	1A8
mouse MHCII (I-A/I-E)	2	557000	BD Biosciences	M5/114.15.2

4.1.6.2 Antibodies for immunohistochemistry

Antigen	Dilution	Product no.	Provider	Clone/Host
Primary antibodies				
Mouse CD45	1:250	550539	BD Pharmigen	30-F11/rat
Mouse Darpp-32	1:200	2306	Cell Signaling	19A3/rabbit
Mouse D2R	1:100	D2R-Rb-Af960	Frontier	Polyclonal/rabbit
Mouse GFAP	1:500	13-0300	Invitrogen	2.2B10/rat

Mouse Iba1	1:500	ab5076	Abcam	Polyclonal/goat
Mouse Iba1	1:400	019-1974	Wako	Polyclonal/rabbit
Mouse Ki67	1:200	ab15580	Abcam	Polyclonal/rabbit
Human/mouse $P2Y_{12}$ receptor	1:200	HPA014518	Sigma	Polyclonal/rabbit
Mouse PSD-95	1:100	ab195006	Abcam	EP2652Y/rabbit
Secondary antibodies				
Goat IgG - H&L (Alexa Fluor® 488)	1:500	ab150129	Abcam	donkey
Rat IgG – H&L) (Biotinylated)	1:200	BA-9400	Vector Labs	goat
Rat IgG H&L (Alexa Fluor® 568)	1:500	ab175475	Abcam	donkey
Rabbit IgG - H&L (Alexa Fluor® 488)	1:500	ab150073	Abcam	donkey
Rabbit IgG H&L (Alexa Fluor® 568)	1:500	ab175470	Abcam	donkey
Rabbit IgG H&L (Alexa Fluor® 647)	1:500	ab150075	Abcam	donkey

4.1.7 Commercial kits

Product	Provider
REDExtract-N-Amp™Tissue PCR Kit	Sigma-Aldrich
DNA 1000 Kit (5067-1504)	Agilent
Dynabeads® mRNA DIRECT™ Kit	Life Technologies
LightCycler® FastStart Essential DNA Green Master	Roche
Nucleospin RNA XS Kit	Macherey-Nagel
RNA 6000 Pico Kit (5067-1513)	Agilent
Roti®-Histokitt	Roth

SuperScript™ II Reverse Transcriptase (18064)	Thermo Fisher Scientific
Vectastain ABC Elite Kit	Vector Labs

4.1.8 Laboratory consumables

Product	Provider
100-µm, 70-µm, 40-µm cell strainer	BD Falcon
15ml, 50ml BD Falcon™ tube, dome-seal screw cap	BD Falcon
1ml, 2ml, 5ml syringe	BD Discardit
5ml, 10ml, 25ml BD Falcon™ serological pipets, individually wrapped	BD Falcon
BD Falcon™ 12x75(mm) tube with and without cell strainer cap	BD Falcon
Electronic scale JJ3000 A	G&G GmbH
Electrophoresis chambers	Biorad
Eppendorf® Safe-Lock microcentrifuge tubes, 0.5, 1.5, 2 mL	Eppendorf
Erlenmeyer flasks	Schott Duran
Glass cover slips (24 x 50 mm)	Roth
Microscope slides (SuperFrost Plus)	R. Langenbrinck
qPCR 96-well plates	Eppendorf
RNAse free tubes individually packed	Eppendorf
Sterile scalpel #21	B. Braun Aesculap

4.1.9 Machines

Product	Provider
2100 Bioanalyzer	Agilent
Burker 7 T PharmaScan® 70/16	Bruker BioSpin
Centrifuge: Biofuge Pico	Heraeus
Centrifuge: Universal 30 F	Hettich

Centrifuge: Universal 32 R Type 1610	Hettich
Centrifuge: Universal 320 R Type 1460	Hettich
Electrophoresis chamber	BioRad Laboratories
FACSAriaII cell sorter	BD Biosciences
FACS Canto II	BD Biosciences
Fluorescence microscope DMRA2 Leica	Leica
Gel documentation camera	Intas GDS
Leica DMI8 with an SPE scan-head	Leica microsystems
LightCylcer® 96 Real-Time PCR System	Roche
MasterCycler® Gradient	Eppendorf
Microwave	Clatronic
MultiGuard barrier tips	Sorenson BioScience
NanoDrop ND2000 spectrophotometer	Thermo Fisher Scientific
PCR soft-tubes 0,2 ml	Biozym
pH meter pH100	VWR International
Pipette tips	Starstedt
Process Control RotaRod 3375 series	TSE systems GmbH
Small Animal Monitoring and Gating System	SA Instruments
Thermomixer Compact	Eppendorf
TSE SP5 confocal microscope	Leica
Vibrating microtome	MICROM 650V
Video camera CCTV	Panasonic

4.1.10 Software

Software	Developer
Adobe Illustrator® CC (24.1.2)	Adobe®
Analyze 10.0	AnalyzeDirect, Inc.
BD FACSDIVA	BD Biosciences
Fiji	1.42q Wayne Rasband
FlowJo	Treestar

GraphPad Prism 5 und 6	GraphPad Software
Imaris Microscopy Image Analysis Software	Bitplane
LightCycler 96 LightCylcer® 96 Real-Time PCR System Software	Roche
Matlab	MathWorks
Paravision 5.1	Bruker BioSpin
Stere Investigator	MicroBrightField
R and R Studio	R Core Team
VideoMot2 Systems, Version 5.68	TSE systems GmbH

4.2 Methods

4.2.1 Details of experimental models

4.2.1.1 Ethics statement, experimental reporting & study design

This study was performed in strict accordance with national and international guidelines for the care and use of laboratory animals (Tierschutzgesetz der Bundesrepublik Deutschland, European directive 2010/63/EU, as well as GV-SOLAS and FELASA guidelines and recommendations for laboratory animal welfare). The animal experiment permission was obtained from the Landesamt für Gesundheit und Soziales (LAGeSo, permission number: G0048-13, 2013) and every effort was made to minimize the number of animals used and their suffering. The reporting of this study was done following the ARRIVE guidelines for reporting *in vivo* experiments.

4.2.1.2 Mouse strains

For details of the mouse strains used in this study please refer to section 4.1.1.

4.2.1.3 Housing and husbandry

Mice were bred and housed at specific pathogen-free (SPF) animal facilities of the *Charité* - Universitätsmedizin Berlin in standard conditions under a 12-hour light cycle (lights on between 06:00 and 18:00) with experiments carried out during the “lights-on” phase. Mice had access to food *ad libitum* and cages were lined with chip bedding and enriched with a mouse tunnel and

igloo (Plexx BV).

B6CBA-Tg(HDexon1)62Gpb/3J males were backcrossed with B6CBAF1/J females to generate hemizygous R6/2 mice and non-transgenic littermates that were used as controls. Homozygous B6.129-*Gt(ROSA)26Sor*$^{tm1(HD*103Q)Xwy}$/J mice were crossed with homozygous *Cx3cr1*$^{tm2.1(cre/ERT2)Jung}$/J mice to generate hemizygous offspring which, following injection with tamoxifen (details in section 4.2.1.5), are referred to as MG-HD mice in this thesis.

4.2.1.4 Genotyping

Genotyping was performed on DNA extracted from ear punches of 5-week-old mice using the REDExtract N-AMP™ Tissue PCR Kit. PCRs were carried out on Mastercycler® Gradient using primer sequences reported in section 4.1.5.1. Amplified products were separated by electrophoresis in a 2% agarose gel (w/v in 1 x TAE buffer) and product size was confirmed against a DNA ladder. Electrophoretically separated PCR products were visualized by adding GelRed® and documented by an Intas GDS® system.

4.2.1.5 Induction of Cre recombinase activity

To induce the activity of Cre recombinase and thus the selective expression of mHTT in microglia, 5- to 7-week-old hemizygous B6.129-*Gt(ROSA)26Sor*$^{tm1(HD*103Q)Xwy}$/J x *Cx3cr1*$^{tm2.1(cre/ERT2)Jung}$/J mice were injected subcutaneously with a total of 4 mg of tamoxifen (T-5648, Sigma) in 200 µl corn-oil over two time-points - 48 hours apart - as previously described (Goldmann et al., 2013).

4.2.1.6 Gender and controls

For all experiments with R6/2 mice, R6/2 males were backcrossed with B6CBAF1/J females to generate hemizygous R6/2 mice and non-transgenic littermates that were used as controls.

For assessment of weight changes, behavioral experiments, TR-FRET mHTT protein quantification, magnetic resonance imaging (MRI), qPCR for *BDNF*, *Nr4a1*, *Drd2* and *Drd1* and all 22-month-experiments, hemizygous B6.129-*Gt(ROSA)26Sor*$^{tm1(HD*103Q)Xwy}$/J mice injected with tamoxifen were used as controls. For qPCR of *mHTT*, hemizygous *Cx3cr1*$^{tm2.1(cre/ERT2)Jung}$/J mice were used as controls. For histology, flow cytometry and RNA sequencing at 3, 6, 12 months hemizygous B6.129-*Gt(ROSA)26Sor*$^{tm1(HD*103Q)Xwy}$/J x *Cx3cr1*$^{tm2.1(cre/ERT2)Jung}$/J mice injected with

corn oil were used as controls. Both male and female mice were used in this study.

4.2.2 Cell isolation for flow cytometry

Mice were deeply anesthetized with a combination of Ketamine (50 mg/kg) and Xylazine (7.5 mg/kg) and transcardially perfused with ice-cold DPBS + 10 mM EDTA (E6511, Sigma).

4.2.2.1 Microglia isolation and fluorescence-activated cell sorting

Brains were dissected, and the olfactory bulb and cerebellum were removed. The remaining brain was minced and filtered through a 70 µm cell strainer in ice-cold high-glucose DMEM (FG0435, Sigma). The cell suspension was centrifuged at 2,000 rpm at 4°C for 5 minutes and the pellet was resuspended in 5 ml of 35% Percoll® (17-0891-02, GE Healthcare) in sterile modified DPBS (10 ml DPBS + 0.1g D-Glucose + 0.07g $NaHCO_3$ + 90 ml ddH_2O) and transferred to a 15-ml centrifuge tube. Tubes were centrifuged at 800 g for 25 minutes at 14°C with no acceleration nor break (Centrifuge: Universal 320 R Type 1460). Leukocyte-containing cell pellets were either washed once in 5 ml DPBS, snap-frozen in liquid nitrogen and stored for TR-FRET mHTT protein quantification or further processed for fluorescence-activated cell sorting (FACS) and subsequent RNA sequencing or *mHTT* qPCR. Further processing involved washing cells with 5 ml sterile sorting buffer (100ml DDPBS + 2 mM EDTA + 0.5 % BSA w/v + 900 ml ddH_2O) and the pellet was subsequently incubated on ice for 10 minutes in 50 µl sorting buffer containing 5 µg/µl antibody against CD16/CD32 (clone 93). A further 50 µl of sorting buffer was then added to the mix that contained fluorescence-conjugated antibodies against the following antigens: CD45 (clone 30-F11; 5 µg/µl), CD11b (clone M1/70; 2 µg/µl), MHCII (clone M5/114.15.2; 2 µg/µl), Ly6G (clone 1A8; 2 µg/µl), Ly6C (clone HK1.4; 2 µg/µl), CD3 (clone 17A2; 5 µg/µl) and CD11c (clone N418; 2 µg/µl). Cells were incubated for 20 minutes at 4° in the dark, washed once with 1 ml sorting buffer. All washing steps were performed at 300 g at 4°C for 10 minutes unless otherwise stated.

Microglia were then flow sorted using the BD FACSAriaII cell sorter at the Flow Cytometry and Mass Cytometry Core Unit of the Berlin Center for Regenerative Therapies (BD Biosciences, BD Diva Software) with the gating strategy shown below (**Fig. 3a).** The purity of the sorted samples was checked check and found to be 86,44 ± 3,51% purity without gating (**Fig. 3b**).

10^4-10^5 singlet $CD45^{lo}CD11b^{+}MHCII^{-}Ly6G^{-}Ly6C^{-}CD3^{-}CD11c^{-}$ microglia were sorted into 100 µl lysis/binding buffer (Dynabeads® mRNA DIRECT™ Kit, Life Technologies) for RNA sequencing

or into 100 µl RA1 + 2 µl TCEP (Nucleospin RNA XS Kit, Macherey-Nagel) for qPCR of *mHTT* and stored at -80°C. Flow cytometry data was analysed with FlowJo (Treestar).

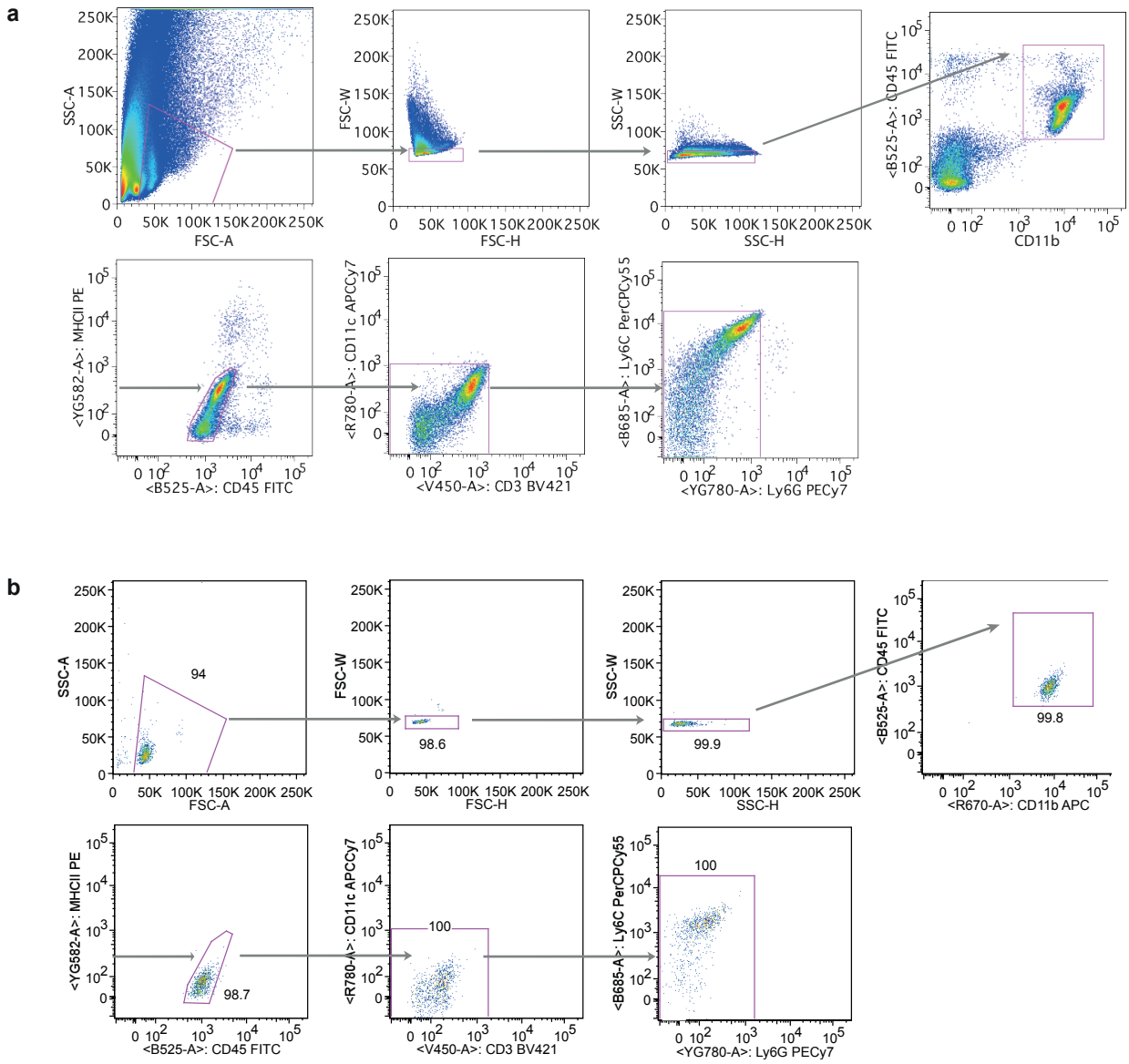

Figure 3 | **Gating strategy (representative snapshot of raw data) for FACS-sorted CD45^{lo}CD11b^{+}MHCII^{-}Ly6G^{-}Ly6C^{-}CD3^{-}CD11c^{-} microglia from Percoll-enriched mouse brain leukocytes (a).** (**b**) Sort-check (representative snapshot of raw data) of CD45^{lo}CD11b^{+}MHCII^{-}Ly6G^{-}Ly6C^{-}CD3^{-}CD11c^{-} microglia from Percoll-enriched mouse brain leukocytes. CD45^{lo}CD11b^{+}MHCII^{-}Ly6G^{-}Ly6C^{-}CD3^{-}CD11c^{-} microglia were sorted at a purity of 86,44 ± 3,51%. Of note, microglia are known to be autofluorescent in various channels, positive signals were defined against unstained or isotype controls for each antibody.

4.2.2.2 Splenocyte isolation and fluorescence-activated cell sorting

Whole spleens were dissected and passed through a 100 µm cell strainer in ice-cold DPBS. Cells

were spun down and pellets were resuspended in lysing buffer (BD Biosciences, 555899) for 8 minutes at room-temperature. Cells were centrifuged at 300 g for 10 minutes at 4ºC and stained with antibodies against CD45 and CD11b as described above (4.2.2.1). Single $CD45^+$ $CD11b^+$ cells were sorted with BD FACSAriaII cell sorter (BD Biosciences, BD Diva Software), and pellets were snap-frozen for mHTT quantification by TR-FRET (see section 4.2.8).

4.2.3 RNA sequencing and data analysis

4.2.3.1 RNA sequencing

mRNA from 10^4-10^5 sorted microglia (see section 4.2.2.1) was bound with Dynabead oligo(dT) (Life Technologies) according to the guidelines of the manufacturer. Library preparation and sequencing was performed by our collaborators at the Weizmann Institute for Science in Israel (group of Dr. Ido Amit; experimental design by Dr. Alexander Mildner) as previously described (Lavin et al., 2014). A modified version of MARS-seq was followed (Jaitin et al., 2014) and the details of the modifications to the original protocol have already been described (Mildner et al., 2017b). RNA-Seq libraries were sequenced with Illumina NextSeq-500.

4.2.3.2 RNA sequencing – data analysis

RNA sequencing analysis was performed by Dr. Kajetan Bentele from the Berlin Institute for Health Core Unit Bioinformatics. In brief, sequencing reads were aligned against the NCBI37/mm9 genome using STAR (Dobin et al., 2013). Gene expression levels were calculated using HOMER makeTagDirectory program (parameters - unique -flip) and analyzeRepeats.pl (parameters - count exons -condenseGenes -strand + -raw) (Heinz et al., 2010). Alignment statistics reported by STAR were used to detect samples with numbers of unmapped reads above threshold, leading to the exclusion of three samples. Principal component analysis of regularized log transformed counts of the top 500 varying genes was used to identify a single outlier that was removed from the analysis. For differential expression analysis, the R package DESeq2 was used (Love et al., 2014). Only protein coding genes were included in the analysis, allowing for outlier detection and independent filtering using the mean of normalized counts as a filter statistic. Finally, FDR adjusted p-values of < 0.05 (5%) were used from the Wald tests and $|\log2|$ fold-changes of 0.5 to filter for differentially expressed genes. To test for the enrichment of Gene Ontology terms with differential expressed genes, the topGO R package was used (Alexa et al., 2006). We used

the "Fisher.classic" method to evaluate enrichment of general nodes and the "Fisher.elim" method to retain enrichment of more specific nodes.

4.2.4. Depletion of microglia with BLZ945

BLZ945 (Novartis) was dissolved in 20% (2-hydroxypropyl)-β-cyclodextrin. Mice were fed a normal diet and, starting at 8 weeks of age and for 12 consecutive days, were given 100 µl total volume of vehicle or BLZ945 by oral gavage. A dose of 200 mg/kg bodyweight was used.

4.2.5 Microscopy

4.2.5.1 Tissue preparation

Mice were deeply anesthetized with a combination of Ketamine (50 mg/kg) and Xylazine (7.5 mg/kg) and perfused transcardially using a pump for 3 minutes with ice-cold 0.9 % NaCl solution and 5 minutes with 4% paraformaldehyde (PFA) in phosphate buffer (PB). Brains (excl. cerebelli) were post-fixed overnight in 4% PFA in 0.1 M PB and transferred to 0.05% sodium azide in 0.1M PB. 35 µm coronal sections were cut using a vibratome (MICROM 650V) and stained as free-floating sections. Cerebelli were also post-fixed overnight in 4% paraformaldehyde (PFA) in phosphate buffer (PB). They were then cryoprotected by 3 x overnight incubation in 30 % sucrose, cryosectioned with a cryostat (30 µm sagittal) and mounted directly to slides for staining.

4.2.5.2 Immunohistochemistry

All immunohistochemistry with the exception of $CD45^{hi}$ quantification using stereology (Section 4.2.5.3) was performed as described here. Sections were washed for 5 min at room-temperature (RT) in TBS (0.15 M NaCl, 0.1 M Tris HCL, 0.02 M Tris base, pH 7.4) and transferred to TBS-T (TBS + 0.3 % Triton-X-100) for a second wash. Antigen retrieval was only performed for PSD-95 and D2R stainings by placing sections in sodium citrate buffer (10mM Sodium Citrate, 0.05% Tween 20; pH=6.0) for 30 minutes in a steamer at 95-100°C. Sections were blocked in 20 % normal donkey serum (NDS) in TBS-T for 1 hour at RT and incubated overnight at 4°C in primary antibody diluted in TBS-T + 2 % NDS/NGS. Sections were then washed 3 x 30 minutes in TBST and incubated overnight at 4°C with appropriate secondary antibodies conjugated to Alexa Fluor dyes (Invitrogen) diluted in TBS-T + 2 % NDS/NGS. For detailed list of primary and secondary antibodies and their working concentrations refer to section 4.1.6.2. Nuclei were stained with

DAPI at a 0.5 mg/ml in phosphate-buffered saline (DPBS). After washing, sections were mounted with FluorSave reagent (Calbiochem).

4.2.5.3 Staining and quantification of $CD45^{hi}$ cells in the MG-HD brain

Free-floating 35 µm coronal brain sections at 5.22 and 4.54 mm interaural (see below) and pre-mounted 30 µm cerebellar sections (2.88 interaural – see below) were washed for 5 minutes at RT in TBS. Sections were quenched with 0.3% H_2O_2 in TBS for 20 minutes and washed 3 x 5 minutes at RT with TBS. This was followed by blocking in 10 % normal goat serum (NGS – v/v) in TBS-T for 1 hour at RT and incubating the sections overnight at 4ºC in primary anti-CD45 antibody diluted in TBS-T + 2 % NDS (v/v). After washing the sections three times in TBS-T for 10 min, they were incubated for 2 h with the biotinylated secondary antibody goat-anti-rat IgG (Vector Laboratories) at a dilution of 1: 200 in TBST. The sections were then washed three times for 10 min in TBS and incubated for 90 min in an avidin-biotin-peroxidase complex at RT (Vectastain ABC Elite Kit). The final visualization of the binding of the antibody to CD45 was done by incubating for 20 minutes at RT with 0.5 % (w/v) DAB Black working solution (9.3 ml ddH_2O + 0.5 ml of 0.1M TB + 0.1ml of 1M Imadazol + 0,1 ml DAB 50mg/ml) and adding 25µl of 3% $(NH_4)_2Ni(SO_4)_2$ followed by 5µl 30% H_2O_2 for 1 minute. Sections were then washed in TBS (1 x 10 min) and ddH_2O (2 x 10 min) and incubated with filtered Hematoxylin solution (Meyer's) for 90 second. Sections were washed 3 x 2 min in ddH_2O, transferred to glass slides dried overnight at RT. The following day, the sections were placed in ethanol step solutions for 1 min each (70%, 96%, 100%, Rotihistol) and embedded in Roti®-Histokitt (Roth). $CD45^{hi}$ immunopositive cells were quantified in various brain regions (cortex, hippocampus, striatum, corpus callosum, midbrain, cerebellum) using the semi-automatic stereology system Stereoinvestigator (Version 10, MicroBrightField). Of note, with the anti-CD45 antibody used here, only $CD45^{hi}$ cells can be visualized and $CD45^{lo}$ microglia are not visualized. The results are given as total $CD45^{hi}$ cells/mm^2.

4.2.5.4 Imaging

All imaging was performed was performed on an upright TSE SP5 confocal microscope unless stated otherwise.

Imaging for the assessment of microglia depletion by BLZ945 (Sections 4.2.4 and 5.2) was performed on two cortical and two striatal single-stack 183.69 x 183.69 µm images from four consecutive sections starting at 4.54 mm interaural.

Imaging locations for the histological assessment of MG-HD mice are described below with brain locations are given by Paxinos and Franklin (Paxinos and Franklin, 2004) and are shown here:

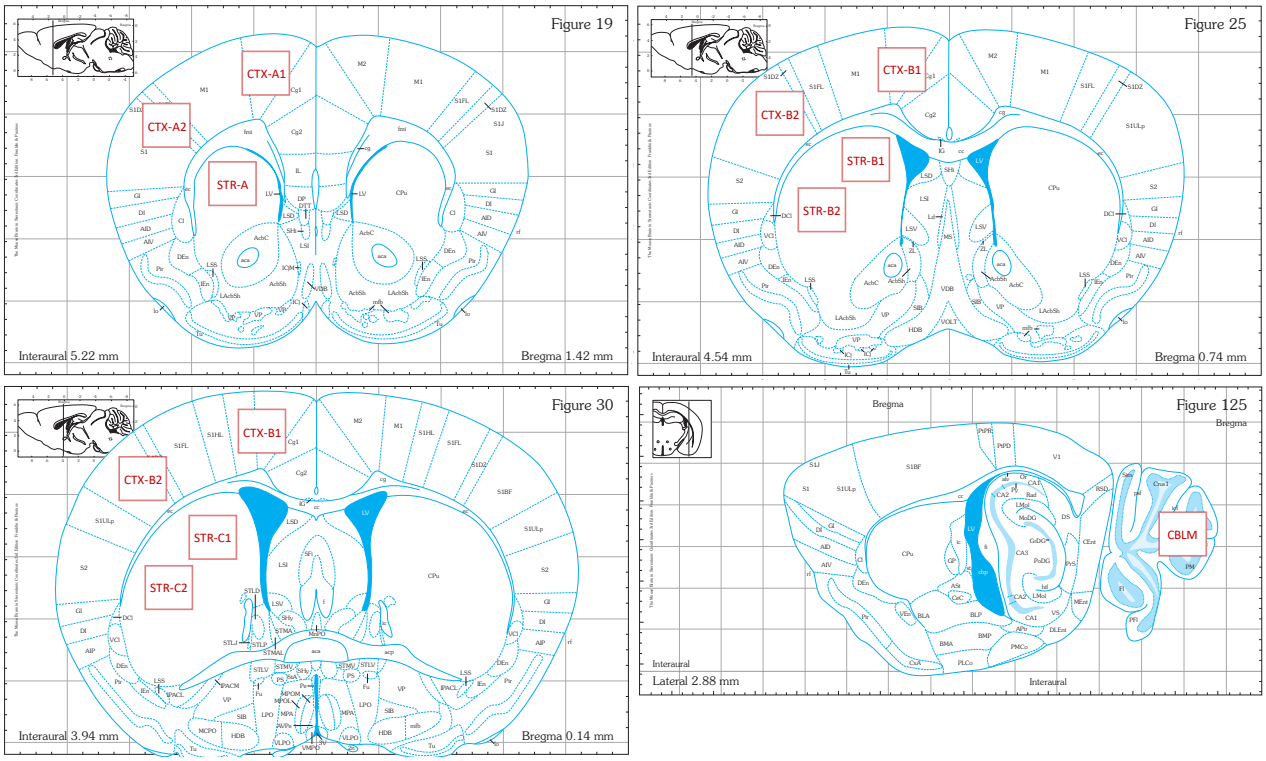

Striatal microglia: Striatal Iba1$^+$ cells were imaged at five locations – STR-A: caudate putamen 5.22 mm interaural, STR-B1: medial caudate putamen 4.54 mm interaural, STR-B2: lateral caudate putamen 4.59 mm interaural, STR-C1: medial caudate putamen 3.94 mm interaural and STR-C2: lateral caudate putamen 3.94 mm interaural. 734 x 734 µm serial plane images were acquired from a single hemisphere over a depth of 10 µm with 0.64 µm z-stack intervals. For $P2Y_{12}$ receptor intensity analyses and correlation of GFAP-coverage with Iba1$^+$ cell density (Fig. 12c, 18c), only imaging from areas STR-B1 and STR-B2 was used.

Cortical microglia: Iba1$^+$ cells were imaged in the same way as striatal microglia at six locations – CTX-A1: Primary/secondary motor cortex 5.22 mm interaural, CTX-A2: Somatosensory cortex 5.22 mm interaural, CTX-B1: Primary/secondary motor cortex 4.54 mm interaural CTX-B2: Somatosensory cortex 4.59 mm interaural CTX-C1: Primary/secondary motor cortex 3.94 mm interaural CTX-C2: Somatosensory cortex 3.94 mm interaural. For $P2Y_{12}$ receptor intensity analyses and correlation of GFAP-coverage with Iba1$^+$ cell density (Fig. 12c, 18c), only imaging from areas STR-B1 and STR-B2 was used.

Cerebellar microglia: Imaging for microglia density (Iba1$^+$ cells) in the cerebellum was done as described for the striatum and cortex on three serial sagittal sections starting at 2.88 mm interaural.

Cortical and striatal astrocytes and measurement of proliferation: To compensate for the inconsistent distributions of GFAP-immunoreactive astroglia and Ki67-immunoreactive proliferating microglia in the adult mouse brain, we scanned whole cortices and striata at 4.54 mm interaural and the cerebelli (sagittal) at 2.88 mm with an Inverted Leica DMI8 with an SPE scan-head (Leica microsystems, Wetzlar, Germany). The regions imaged can be seen here for cortex and striatum (A) and for cerebellum (B) and were defined as annotated by the numbering:

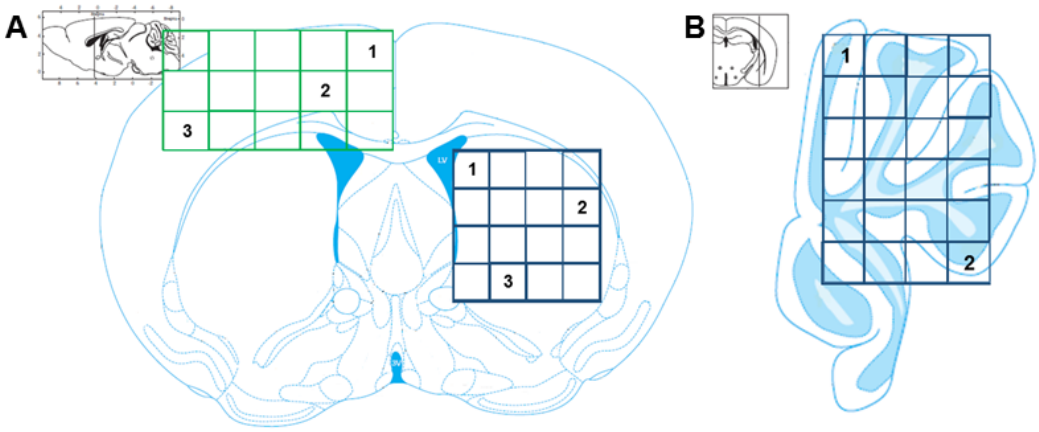

Panoramic images were created by autonomous stitching at 10 % of the tile scans with statistical overlap blending (Fig. 9d, 12b, 17d, 18b).

Striatal neurons: For the calculation of the mean minimum distance between striatal neurons (Darpp-32^{+}) a single plane image with 508 x 508 µm dimensions was acquired at each of the five striatal locations mentioned above. The intensity of D2R signal was calculated from a single plane image with 234.32 x 234.32 µm dimensions at STR-B1 and STR-B2. Two single plane images of area STR-B caudate putamen were taken with 46 x 46 µm dimensions for PSD-95 imaging.

4.2.5.5 Image processing and quantitative analyses

All image processing was done with Fiji (Schindelin et al., 2012). Matlab scripts (MathWorks) were used to for image randomization and blinding and to extract data from Imaris Microscopy Image Analysis Software (Bitplane).

Only for the quantification of microglia depletion by BLZ945, Iba1^{+}DAPI^{+} positive cells were quantified manually using Fiji. For the rest of the striatal and cortical Iba1^{+} cell density quantifications, Imaris Microscopy Image Analysis Software (Bitplane) was used. For this, a co-localization channel was created for DAPI/Iba1 overlapping signal. Then, the built-in Imaris spot-detection algorithm was used to identify spots of a 10 µm dimeter in this channel with the threshold

being manually determined for each image.

Striatal and cortical Iba1$^+$ cell volume was also quantified using Imaris with the built-in surface-detection algorithm with a surface grain size of 0.100 µm and a manually set threshold.

$P2Y_{12}$ receptor signal intensities were calculated using Fiji. A manual threshold was set for each image to cover positive immunofluorescent signal and the mean intensity was obtained in arbitrary units.

For Iba1/Ki67 cell quantifications, the built-in Imaris spot-detection algorithm was used to count Iba1$^+$ microglia of a 10 µm in the Iba1 channel (individually adjusted for each image), while Iba1$^+$Ki67$^+$ were manually counted.

Darpp-32$^+$ striatal neurons were identified using the built-in spot-detection algorithm for Darpp-32 immunoreactive areas of 8 µm dimeter with the threshold being manually determined for each image. The Spots Closest Distance Xtension was subsequently used to calculate the mean minimum distance between spots (cells). A similar strategy was used to calculate the mean minimum distance between PSD-95-immunoreactive puncta, only the spot diameter in this case was set to 0.25 µm diameter.

The D2R-immonoreactive surface of the striatum was identified the built-in surface-detection algorithm of Imaris with the surface grain size set to 1 µm, allowing for the exclusion of striatal axon tracts from the analysis. The mean intensity of the D2R signal was then extracted.

For volumetric analysis of GFAP$^+$ areas in panoramic scans, the built-in surface-detection algorithm of Imaris was used (surface detail = 3 µm, threshold = 45) and adjusted individually for each image to estimate GFAP coverage as a percentage of the total volume scanned.

4.2.6 Weight monitoring and behavioural tests

4.2.6.1 Mouse acclimatization and weight monitoring

Prior to weight evaluation and behavioural testing, MG-HD mice and their respective controls were acclimated to the behavioural facility for 7 days under a regular dark-light cycle (lights on between 07:00 and 19:00) while a radio played constantly as background noise. During this acclimatization phase, animals were handled daily by the experimenter that performed the behavioural tests. Mice were weighed at 10:00 on the day of the Open field, RotaRod and Y-maze tests and were allowed to habituate for 1 hour in the experimentation room prior to testing.

4.2.6.2 Behavioural tests: Open field test, RotaRod & Y-maze test for spontaneous alternations

For the Open Field test, mice were placed in the center of a 50 x 50 cm arena surrounded by 39 cm tall walls. Their exploratory activity was recorded with a video camera (Panasonic, CCTV camera) and tracked with the VideoMot2 video tracking system (Version 5.68, TSE systems GmbH, Bad Homburg, Germany), with the central region defined as 50 % of the total area.

For the RotaRod test, mice were placed on an accelerating rod (Process Control RotaRod 3375 series, TSE systems GmbH) with the acceleration set from 4 to 40 rpm over 5 minutes. The time each mouse was able to stay on the rod was recorded for three trials with 10-minute intervals. Three trials were recorded per mouse with an interval of at least 15 min and the best performance was used for statistical analysis.

Short-term memory of R6/2 mice was assessed with the Y-Maze spontaneous alternation test. Testing took place in a Y-shaped maze with opaque plastic arms (length: 40 cm, height: 10.5 cm and width: 3 cm) at a 120º angle from each other (see below). Mice were placed in the center of the maze facing arm no. 1 and were allowed to freely explore the maze over 8 minutes. The arm entries were documented manually, and a video of each trial was recorded. Each arm entry was considered only if all four limbs of the animal were within the arm. Over the course of the multiple arm entries, the subject should show a tendency to enter the less recently visited arm. The entries of the mouse to each arm were recorded and the number of triplets of alternating arm entries were counted (see example below). Then, the percentage of alternation was then calculated:

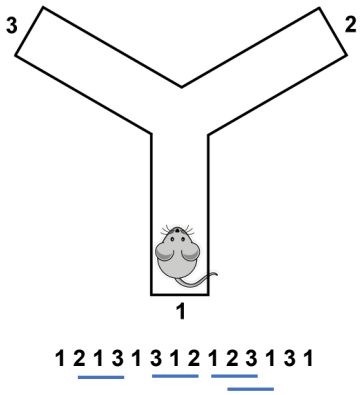

$$\%\ \text{Alternations} = \frac{\text{Number of triplets}}{\text{Total number of arm entries}} * 100$$

All behavioural tests (Open Field, RotaRod and Y-maze) were performed under dim light at 35 lux and instruments were thoroughly cleaned between runs with Decosept AF (Dr. Schumacher GmbH). All tests were

4.2.7 Quantitative polymerase chain reactions

4.2.7.1 RNA isolation, cDNA synthesis from FACS-sorted microglia

To confirm the expression of human mutant huntingtin in microglia of male MG-HD mice at 3, 6 and 12 months of age and 11-week-old male R6/2 mice, RNA was purified from sorted microglia (see section 4.2.2) using the Nucleospin® RNA XS Kit (Macherey-Nagel) with 1 µl of 5 µg linear acrylamide as a carrier (AM9520, Ambion). RNA was quantified with RNA 6000 Pico Kit on a 2100 Bioanalyzer (Agilent). cDNA was synthesized with Superscript II Reverse Transcriptase and random primers by Invitrogen (Thermo Fisher Scientific) following the manufacturer's protocols and quantified with a DNA 1000 Kit on a 2100 Bioanalyzer (Agilent).

4.2.7.2 RNA isolation, cDNA synthesis from whole brain lysates

Total RNA purification from snap-frozen whole-brain of male and female MG-HD mice and their respective controls at 12 months of age was performed using TRIzol™ following the manufacturer's protocol. Samples were resuspended in DEPC-H_2O and genomic DNA was digested with RQ1 RNase-Free DNase (Promega) according to the manufacturer's guidelines. Total RNA concentration was determined with NanoDrop (Thermo Scientific), and probes were uniformly diluted. cDNA was synthesized with Superscript II Reverse Transcriptase and random primers by Invitrogen (Thermo Fisher Scientific) following the manufacturer's protocols and quantified with a Nanodrop ND2000 Spectrophotometer (Thermo Fisher Scientific).

4.2.7.3 qPCRs

cDNA from sorted microglia or from whole brain lysates was used for qPCR of human *Htt* using human-specific primers (Liu et al., 2016) and *Gapdh* and *Hprt* as reference genes. cDNA from whole brain lysates was used for qPCR of *BDNF*, *Nr4a1*, *Drd2* and *Drd1* with *Gapdh*, *Hprt* and *Actb* as reference genes. Primer sequences can be found in section 4.1.5.2. All qPCRs were performed in duplicate using the LightCycler® FastStart Essential DNA Green Master (Roche) according to the manufacturer's protocol on a LightCylcer® 96 Real-Time PCR System (Roche). Amplification efficiencies were determined for each primer pair by a serial dilution curve and calculated using LightCycler 96 data analysis software. Polymerase chain reaction (PCR) was performed using the following program: 1) pre-incubation at 95°C for 10 minutes; 2) denaturation at 95°C for 10 seconds, annealing at primer-specific temperatures for 10 seconds, extension at

72°C for 15 sec (45 cycles); 3) final cooling step of 30 sec at 37°C. Specificity of amplified PCR products was confirmed with melting curve analysis (LightCycler Software) and electrophoresis using a 2% agarose gel with GelRed® nucleic acid intercalator as a stain. Samples were mixed with loading dye (Gel Loading Dye, Orange (6X), Biolabs), product size was confirmed against a DNA ladder and visualized using the Intas GDS® system.

Gene expression normalization factors were calculated for each sample based on the geometric mean of a of the reference genes through the use of the GeNorm algorithm (Pfaffl et al., 2004 & Vandesompele et al., 2002)

4.2.8 mHTT protein quantification by TR-FRET

Mice were deeply anesthetized with a combination of Ketamine (50 mg/kg) and Xylazine (7.5 mg/kg) and transcardially perfused with ice-cold PBS. Percoll® separation was performed on brain homogenates from male and female MG-HD mice and their respective control and the leukocyte fraction was snap-frozen and further processed for mHTT protein quantification (cell isolation procedure described in detail in section 4.2.2.1). $CD45^+CD11b^+$ splenocytes were collected as described in section 4.2.2.2. Snap-frozen pellets of brain leukocytes or $CD45^+CD11b^+$ splenocytes were processed and measured by TR-FRET by our collaborator Dr. Andreas Weiss as described previously (Weiss et al., 2012).

4.2.9 Magnetic resonance imaging and data analysis

4.2.9.1 Magnetic resonance image acquisition

MRI was performed on 12-month-old male MG-HD mice and their respective controls. Mice were fully anesthetized with 5 % isoflurane in 70 % N_20 and 30 % oxygen. Mice were then positioned and fixed in a plastic frame with a constant flow of 1-2 % isoflurane in 70 % N_20 and 30 % oxygen administered through a facemask for the duration of the scan. Temperature was kept stable with a heat blanket and mouse respiration rates were monitored (Small Animal Instruments, SA Instruments, Inc., Stony Brook, USA). Images were acquired on a Bruker 7 T PharmaScan® 70/16 (Bruker Biospin, Ettlingen, Germany) equipped with a ^{1}H-RF quadrature-volume resonator (RAPID Biomedical, Würzburg, Germany) with an inner diameter of 20 mm. Paravision 5.1 software (Bruker) software was used to control the scanner. T2 weighted MRI was obtained using a TurboRARE sequence (imaging parameters: field of view 2.56 x 2.56 cm, slice thickness:

0.5 mm, slice orientation: axial, TE: 36.0 ms, TR: 4200 ms, 32 slices). 20 axial slices were used to cover the area between the olfactory blub and the cerebellum.

4.2.9.2 Magnetic resonance image analysis

Analysis of the MRI data was performed by our collaborators Dr. Stefan Paul Koch and Dr. Philipp Boehm-Sturm from the Department of Experimental Neurology, Center for Stroke Research Berlin (CSB), Charité Core Facility. Atlas registration was performed in Matlab (MathWorks). First, the MSME-volume and T2-volume were co-registered to the T2-weighted volume (Rare) for each mouse. Then, the T2-weighted image volumes were co-registered to the Allen template using an initial rigid body transformation followed by an affine transformation with ELASTIX (Klein et al., 2010). When this failed, the co-registration was performed manually using a custom graphical user interface with an overlay of source and target volume. The affine co-registration step only extracted transformation parameters, which were later concatenated with parameters from non-linear transformation (warping) to allow a single combined transformation from mouse space into Allen space, avoiding artefacts from concatenated interpolations. The T2-weighted (T2w) image was then segmented into tissue compartments (grey matter, white matter, cerebrospinal fluid) using SPM's 'unified approach' (Ashburner and Friston, 2005) for segmentation and normalization (SPM8). For this step, the standard parameter settings and tissue probability maps (TPMs) from SPMMouse were used, the latter already in registration with the Allen template. Although non-linear transformation (warping) into target space is also conducted by SPM's unified approach, ELASTIX was used for warping due to its better performance for warping T2w images. For non-linear transformation with Elastix we used two synthetic images generated by linear combination of i) the three TPMs from SPMMouse as fixed image and ii) the three tissue compartment maps derived from the T2w-segmentation step as moving image. At the end of the warping step the concatenation of linear and non-linear transformation parameters allowed the transformation of the T2w image, the MSME-volume and the T2 volume into Allen space. To save memory, registered images were down-sampled to 70 µm isotropic resolution. Additionally, the determinant of the Jacobian matrix (JD) of the transformation was generated. This volume represents the voxel-wise local volume changes (tissue compression or expansion) from mouse space to Allen space. Statistically, two different approaches were tested. First, volume changes using JD image were statistically compared between the MG-HD and the control group using a voxel-wise two-sample t-test. The T2-map was similarly tested. As an independent approach, mean grey-level intensities (t2-relaxation time) of the T2-volume were statistically compared between the groups on the level

of anatomical labels (1204 anatomical labels based on the Allen atlas). The anatomical labelling approach revealed significant differences between groups in some cortical areas. However, this analysis is based on uncorrected t-statistics. To cope with the multiple comparison problem and to treat alpha-inflation, both Bonferroni-correction and false discovery rate (FDR) methods were independently applied.

4.2.10 Data generation, processing, statistical analyses and presentation

Steps were taken to minimize the effects of subjective bias when collecting and assessing results. Data was generated and processed with the experimenter being blinded to the genotype of the animals. In experiments utilizing the R6/2 strain, this was not possible due to a clear phenotype of these mice (weight loss, motor abnormalities, ventricular enlargement etc.). Statistical analyses for RNA sequencing and MRI have been described in the relevant Methods sections. For all other comparisons, statistical methods are described in the respective figure legends. This was an exploratory study so statistical analyses are indicative. All tests were two-sided and a significance level of $\alpha=0.05$ was applied. $P < 0.05$ was considered significant. No statistical methods were used to pre-determine sample sizes, but our sample sizes are similar to those generally employed in the field (e.g.: Crotti et al., 2014; Kwan et al., 2012; Petkau et al., 2019; Siew et al., 2019). The number of biological replicates is shown as n=x in figure legends. Representative images shown are those closest to the relevant quantified mean per group. Data in figures were presented as scatterplots using Prism 6.0 software (GraphPad) and Adobe Illustrator® was used to compose figure panels. This was an exploratory study (Kimmelman et al., 2014), therefore no further adjustments were applied for multiple testing.

5. Results

5.1 Transcriptomic profile of microglia isolated from the R6/2 mouse model of HD

The R6/2 line is transgenic for the 5' end of the human HD gene, carrying a single copy insertion of mHTT-exon1 with approximately 120 +/- 5 CAG repeats (https://www.jax.org/strain/006494). The transgene insertion site is within an intron of the predicted gene *Gm12695* on mouse chromosome 4 and the transgene is ubiquitously expressed (Cowin et al., 2011). R6/2 mice show a progressive neurological phenotype that recapitulates some clinical features of HD (Mangiarini et al., 1996). Symptoms start at around 7 weeks when mice start to lose weight and develop involuntary stereotypic movements, tremor and mHTT intranuclear inclusions, among other symptoms (Cowin et al., 2011 and Mangiarini et al., 1996). R6/2 mice die prematurely at 10-13 weeks of age (Mangiarini et al., 1996).

So far, transcriptomic changes of microglia in animal models of HD have only been identified by looking specifically at the expression levels of individual candidate genes such as *Il6* or *Tnf* (e.g. Björkqvist et al., 2008 and Crotti et al., 2014). We took an unbiased approach and performed RNA sequencing on $CD45^{lo}CD11b^{+}MHCII^{-}Ly6G^{-}Ly6C^{-}CD3^{-}CD11c^{-}$ FACS-sorted microglia from male 10-week-old R6/2 mice and their non-transgenic littermates (see **Fig. 3** in section 4.2.2 for sorting strategy and sort-check). The sorted population included microglia from all brain regions with the exclusion of the cerebellum and the olfactory bulb. The resulting sorted cells had the gene signature of myeloid cells (e.g. *Itgam, Cx3cr1, Csf1r, Aif1, Cd68*) and more specifically genes that are known to be specifically upregulated in microglia (e.g. *Olfml3, P2ry12, Tmem119*). Furthermore, the sorted population did not express genes typically expressed by possible contaminating populations such as macrophages or monocytes (e.g. *Fabp4, Serpinb2, Ly6c2*), oligodendrocytes (e.g. *Tpp3*), astrocytes (*Gfap*), neurons (e.g. *Rbfox3, Thy1*), B cells (e.g. *CD19*), T cells (e.g. *CD3e*), and granulocytes (e.g. *Mmp9*), indicating that the sorted population was highly pure for microglia (**Fig. 4a**).

Microglia sorted from 10-week-old R6/2 mice exhibited a transcriptional phenotype of 128 upregulated and 213 downregulated genes compared to their respective controls (log2-fold change larger than 0.5 with an adjusted *p* value of 0.05 or lower; **Table 2**).

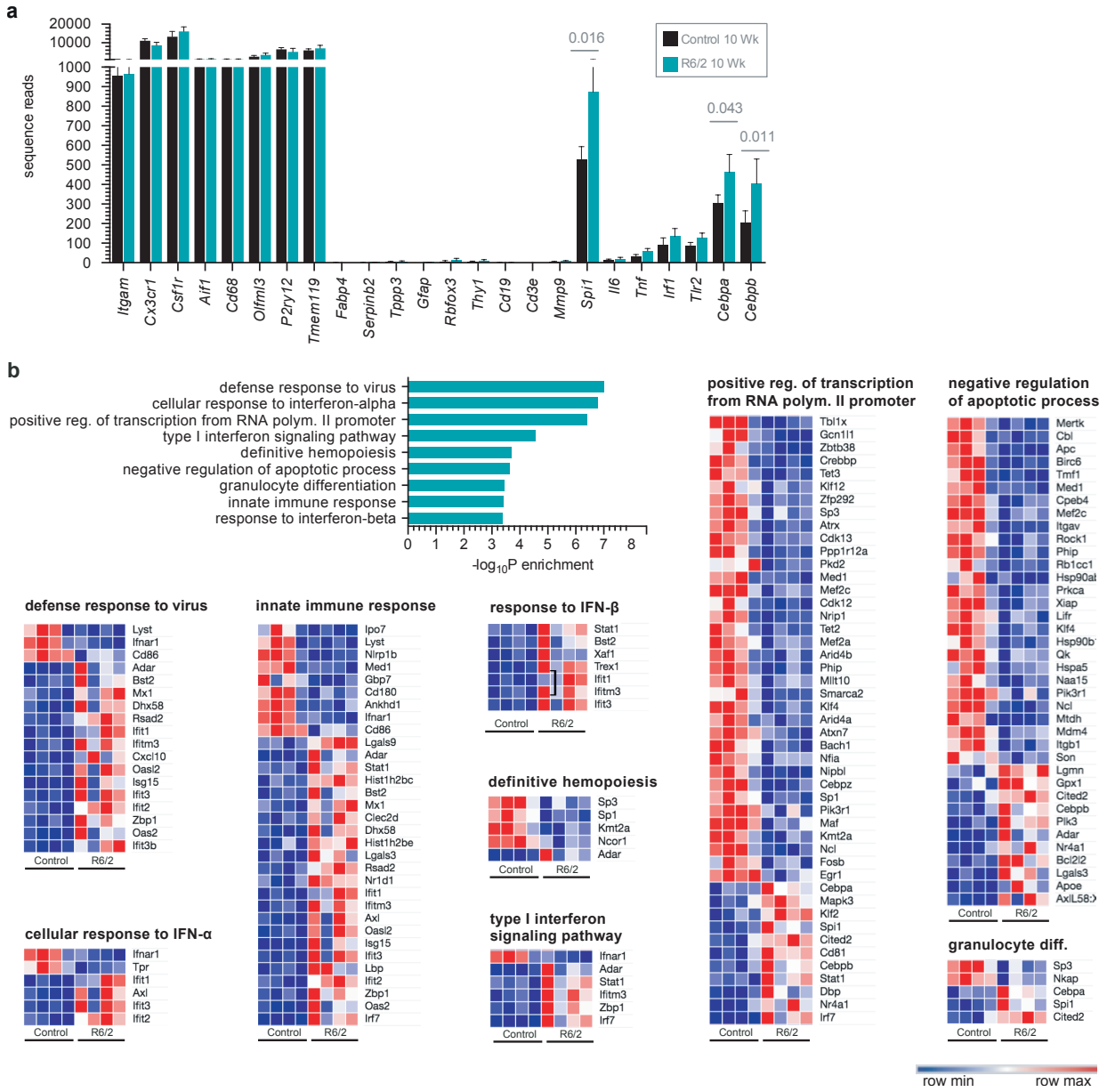

Figure 4 | **Transcriptional profile of microglia isolated from male 10-week-old R6/2 mice and their non-transgenic littermate controls.** (**a**) mRNA expression levels of selected genes in microglia FACS-sorted from 10-week-old R6/2 mice compared to controls (n=4). Data in shown as mean sequence reads ± SD with FDR-adjusted *p* values from the Wald tests. (**b**) Gene Ontology (GO) analysis of differentially expressed genes in 10-week-old R6/2 – only highly enriched and biologically relevant annotations shown. Heatmaps are of differentially genes differentially expressed within each GO term.

The myeloid lineage-determining factors *Spi1*, *Cebpa* and *Cebpb*, were increased in R6/2 mice compared to their non-transgenic littermates, as previously reported (Crotti et al., 2014). However, changes in the expression of downstream target genes (e.g. *Il6*, *Tnf*, *Irf2* or *Tlr2*) did not reach statistical significance (**Fig. 4a**).

Gene Ontology analysis of the entire set of differentially expressed genes indicated significant enrichment in terms related four broad categories: (a) type I interferon signalling, (b) transcriptional dysregulation, (c) regulation of apoptosis, and (d) hematopoietic lineage/granulocyte differentiation ("Fisher.elim" method of topGO R package with $p < 10^{-2.5}$; **Fig 4b**). Selected highly enriched and biologically meaningful GO terms and the genes identified to be differentially expressed within these terms can be seen in **Fig. 4b**. This data provides insight into transcriptomic changes that take place in microglia in the R6/2 brain. It is not possible to decipher, from this data, which of these effects occur cell-autonomously due to mHTT expression in microglia and which occur as a response to mHTT expression in surrounding cells.

Table 1 | **List of differentially expressed genes in microglia of 10-week-old R6/2 mice relative to their respective controls.** For details on the data analysis strategy please refer to section 4.2.2.1.

Downregulated Genes

Gene name	log2-Fold Change	Adjusted p-value
Wdfy2	-3.955	5.802E-03
Itgae	-3.522	1.186E-02
Ipo7	-2.954	2.755E-02
Ipcef1	-2.949	2.974E-02
Tbl1x	-2.506	7.587E-04
Hmbox1	-2.467	6.183E-03
Tulp4	-2.351	2.301E-02
Vps13c	-2.349	1.728E-02
Zbed6	-2.318	7.835E-04
Arhgap32	-2.214	3.433E-02
Lyst	-2.173	2.755E-02
Trip11	-2.094	5.797E-04
Tmem245	-1.988	2.695E-03
Gcn1l1	-1.966	1.829E-03
Mertk	-1.867	2.559E-05
Rlf	-1.866	2.393E-04
Rab5a	-1.859	7.155E-03
Chd9	-1.822	7.587E-04
Zbtb38	-1.821	2.695E-03
Hnrnpul1	-1.819	2.045E-02
Gatad2b	-1.771	3.469E-02
Srcap	-1.761	4.723E-02
Zfp518a	-1.760	6.258E-03
Abca9	-1.750	3.803E-04
Fam208b	-1.714	2.821E-02
Casp8ap2	-1.710	9.014E-03
Ranbp2	-1.695	6.933E-04
Nlrp1b	-1.692	1.328E-03
Tnfrsf13b	-1.674	8.372E-03
Prrc2c	-1.662	3.211E-04
Zfp638	-1.640	2.521E-03
Myo9a	-1.624	7.587E-04
Tshz1	-1.569	1.214E-02
Crebbp	-1.554	5.320E-03
Arhgap5	-1.551	7.587E-04
Pard3b	-1.549	3.583E-02
Tet3	-1.504	1.133E-03
Upf2	-1.492	1.728E-02
Fam208a	-1.487	7.587E-04
Cbl	-1.470	1.099E-02

Upregulated Genes

Gene name	log2-Fold Change	Adjusted p-value
Slc2a6	3.600	5.333E-03
Ifit3b	3.430	3.711E-03
Irf7	3.412	5.069E-12
Ifi27l2a	3.313	4.996E-15
Rtp4	3.291	3.569E-21
Oas2	3.121	1.152E-03
Zbp1	3.020	7.371E-03
Ifit2	2.813	2.711E-04
Slfn2	2.610	2.604E-10
Hap1	2.580	4.687E-02
Lbp	2.563	1.287E-02
Ifit3	2.554	4.861E-05
Isg15	2.489	7.549E-06
Oasl2	2.476	3.173E-03
Cxcl10	2.438	8.372E-03
Axl	2.356	4.522E-03
Apoe	2.309	1.532E-03
Ifitm3	2.273	1.892E-05
Sdc3	2.246	1.115E-03
Usp18	2.240	7.587E-04
Pyhin1	2.225	4.455E-02
Adgrg5	2.182	2.711E-04
Lgals3bp	2.156	1.508E-11
Ifit1	2.070	2.624E-02
Nr1d1	2.056	2.695E-03
Rsad2	2.050	1.422E-02
Qsox1	1.879	3.384E-03
Lgals3	1.832	6.183E-03
H1f0	1.821	2.442E-09
Hist1h3a	1.810	3.679E-02
Trex1	1.771	1.872E-10
Hist1h2be	1.759	5.025E-03
Dhx58	1.758	4.779E-03
Ly6a	1.722	4.610E-02
Clec2d	1.643	1.152E-03
Bcl2l2	1.618	3.908E-02
Mx1	1.607	4.496E-02
Bbc3	1.559	4.985E-02
Hist2h2aa2	1.542	1.823E-02
Hist2h2aa1	1.542	1.728E-02

Apc	-1.445	1.345E-04	*Xaf1*	1.533	7.371E-03
Klf12	-1.440	4.610E-02	*Nr4a1*	1.499	2.431E-02
Zfp292	-1.438	7.587E-04	*Phf11b*	1.434	1.987E-03
Atp11c	-1.422	4.426E-02	*Tmem205*	1.433	2.705E-02
Birc6	-1.421	1.197E-03	*Smarcd3*	1.397	4.288E-02
Fam13b	-1.412	4.178E-02	*Dbp*	1.386	3.621E-03
Macf1	-1.405	1.006E-03	*Bst2*	1.356	7.487E-03
Prpf40a	-1.401	1.816E-03	*Rac3*	1.352	1.659E-02
Sp3	-1.397	1.374E-02	*Tmed1*	1.341	1.251E-02
Atrx	-1.391	5.654E-04	*S100a4*	1.318	4.610E-02
Hsp90aa1	-1.385	1.628E-02	*Dedd2*	1.294	4.178E-02
Zfp397	-1.383	3.679E-02	*Mmp14*	1.269	1.408E-02
Bod1l	-1.365	3.803E-04	*Hist1h2bc*	1.253	4.825E-05
Cdk13	-1.362	4.016E-03	*Fgl2*	1.229	2.050E-02
Ptprj	-1.360	3.588E-02	*Tmod1*	1.221	3.439E-02
Rgs7bp	-1.341	8.372E-03	*H2-K1*	1.216	1.905E-04
Cep170	-1.333	2.045E-02	*Anxa5*	1.154	1.099E-02
Ppp1r12a	-1.326	4.485E-03	*Tspan33*	1.141	2.331E-02
Cwf19l2	-1.323	3.389E-02	*Sepw1*	1.139	1.405E-02
Thoc2	-1.305	1.133E-03	*Stat1*	1.124	3.758E-03
Eif3a	-1.303	1.152E-03	*Inppl1*	1.122	5.802E-03
Morc2a	-1.283	3.534E-02	*Rce1*	1.103	3.671E-02
Bmp2k	-1.283	5.693E-03	*Cnp*	1.093	6.544E-03
Tmf1	-1.269	4.522E-03	*Cd34*	1.083	4.225E-02
Pkd2	-1.260	1.105E-02	*Ier2*	1.083	1.345E-02
Smg1	-1.246	4.522E-03	*Ccdc85b*	1.066	8.825E-03
Ppig	-1.237	2.370E-04	*Acads*	1.022	2.477E-02
Kdm5b	-1.235	4.178E-02	*Bckdha*	1.008	1.630E-04
Pdzd8	-1.235	1.267E-02	*Arpc1b*	0.985	1.405E-02
Cpeb4	-1.233	6.310E-03	*Adar*	0.984	2.154E-02
Med1	-1.229	2.301E-02	*Plk3*	0.980	1.101E-03
Rock2	-1.226	1.133E-03	*1500012F01Rik*	0.974	5.565E-03
Tgs1	-1.226	7.430E-03	*Cebpb*	0.968	1.079E-02
Slc8a1	-1.213	5.535E-04	*Abca7*	0.960	2.624E-02
Gbp7	-1.213	8.454E-03	*Ifi35*	0.952	3.217E-03
Mef2c	-1.202	7.587E-04	*Cd81*	0.947	7.587E-04
Wapl	-1.184	1.398E-02	*Ly6e*	0.931	5.535E-04
Mga	-1.182	7.063E-03	*Epsti1*	0.929	1.398E-02
Nemf	-1.176	5.594E-03	*Pafah1b3*	0.917	1.141E-02
Cdk12	-1.173	4.178E-02	*Calm3*	0.871	3.551E-02
Nrip1	-1.163	4.477E-03	*Cd82*	0.870	2.695E-03
Ankhd1	-1.163	4.446E-02	*Wdr74*	0.858	4.610E-02
Cd180	-1.162	4.165E-02	*Bmyc*	0.847	1.383E-02
Zc3h13	-1.159	2.949E-02	*Adamts10*	0.841	1.507E-02
Pcmtd1	-1.153	7.155E-03	*1600014C10Rik*	0.833	3.679E-02
5730455P16Rik	-1.150	5.574E-03	*Dopey2*	0.831	1.632E-02
Prr14l	-1.150	3.208E-02	*Rasa4*	0.823	3.507E-03
Cep350	-1.142	1.642E-02	*Cd9*	0.821	8.454E-03
Fcho2	-1.142	3.534E-02	*Hpgd*	0.769	1.079E-02
Prpf4b	-1.132	5.744E-03	*Ogfr*	0.768	3.679E-02
Spag9	-1.131	1.141E-02	*Cited2*	0.755	2.366E-02
Tet2	-1.130	4.288E-02	*Sema4g*	0.755	7.870E-03
Cep68	-1.124	1.492E-02	*Ypel3*	0.736	7.587E-04
Pcm1	-1.120	2.458E-03	*Szrd1*	0.733	3.220E-02
Zfp426	-1.119	3.348E-02	*Mpdu1*	0.733	2.331E-02
Map3k2	-1.117	5.565E-03	*Ctsz*	0.727	4.679E-03
BC005561	-1.116	4.964E-03	*Spi1*	0.727	1.628E-02
Phf20l1	-1.099	2.521E-03	*Col27a1*	0.723	5.170E-03
Golgb1	-1.090	3.627E-02	*Klf2*	0.709	3.173E-03
Mef2a	-1.085	1.050E-03	*Lgals9*	0.701	1.152E-03
Filip1l	-1.084	1.079E-02	*P2ry6*	0.699	3.439E-02
Itgav	-1.082	1.114E-02	*Scamp3*	0.699	4.496E-02
Rock1	-1.075	3.654E-03	*Cnppd1*	0.699	2.366E-02
Esf1	-1.072	4.602E-02	*Pgls*	0.697	3.681E-02
Ifnar1	-1.069	9.027E-03	*Map1lc3a*	0.693	4.153E-02
Bank1	-1.064	1.515E-02	*Klk8*	0.690	9.564E-03
Dnajc10	-1.064	3.165E-02	*Chmp4b*	0.689	2.525E-02
Rab8b	-1.062	4.985E-02	*Khk*	0.679	2.768E-02
Pkn2	-1.059	1.728E-02	*Gpr137*	0.674	1.301E-02
Arid4b	-1.058	3.166E-02	*Slc22a17*	0.671	3.457E-02
Nkap	-1.051	2.755E-02	*Mapk3*	0.663	3.583E-02
Pik3c2a	-1.043	4.178E-02	*Bsg*	0.660	1.006E-02

Phip	-1.041	8.372E-03	*Cdipt*	0.653	1.422E-02
Mllt10	-1.034	3.525E-02	*Tmem176a*	0.628	4.385E-02
Akap9	-1.031	1.715E-02	*Pck2*	0.625	4.892E-02
Pcf11	-1.030	1.728E-02	*Gpx1*	0.624	3.671E-02
Trim33	-1.030	4.337E-02	*Crybb1*	0.621	4.016E-02
Huwe1	-1.018	1.050E-03	*Cebpa*	0.606	4.248E-02
Rnf20	-1.014	2.416E-02	*Lgmn*	0.588	4.178E-02
Arhgap30	-1.006	8.893E-03	*Aldoa*	0.587	3.679E-02
Smarca2	-1.005	2.175E-03	*Pld4*	0.584	4.337E-02
Rb1cc1	-1.001	2.463E-02	*Tubb5*	0.583	3.744E-02
Top1	-0.999	3.621E-03	*Tns1*	0.575	4.153E-02
Rsf1	-0.996	2.045E-02	*Ccdc107*	0.555	3.031E-02
Tpr	-0.995	5.827E-03	*Ctss*	0.548	3.287E-02
Kdm5a	-0.994	2.246E-02	*Dhrs3*	0.541	4.521E-02
Sbno1	-0.993	9.536E-03	*Rhog*	0.537	3.166E-02
Hsp90ab1	-0.987	4.153E-02	*Gnas*	0.500	4.951E-02
Hook3	-0.984	1.306E-02			
Taf3	-0.981	2.366E-02			
2810474O19Rik	-0.981	2.046E-02			
Prkca	-0.978	2.020E-02			
Ankrd12	-0.962	1.489E-03			
Xiap	-0.960	1.186E-02			
Smc6	-0.957	3.201E-02			
Lifr	-0.951	2.525E-02			
Usp8	-0.944	3.758E-03			
Klf4	-0.942	7.587E-04			
Hsp90b1	-0.938	1.106E-03			
Wnk1	-0.926	6.498E-04			
Bptf	-0.926	7.430E-03			
Jmjd1c	-0.925	1.846E-03			
Arid4a	-0.922	2.386E-02			
Setd2	-0.922	2.525E-02			
Atxn7	-0.917	2.965E-02			
Slc12a2	-0.917	3.534E-02			
Secisbp2l	-0.916	1.398E-02			
Zmynd8	-0.915	1.374E-02			
Qk	-0.914	6.258E-03			
Aff4	-0.913	2.768E-02			
Acbd3	-0.911	3.736E-02			
Clasp2	-0.905	2.761E-02			
Trip12	-0.903	2.246E-02			
Bach1	-0.897	1.487E-02			
Adap2	-0.896	1.718E-02			
Rassf4	-0.896	2.331E-02			
Cd2ap	-0.890	4.084E-02			
Kmt2c	-0.884	1.839E-02			
Tmem131	-0.880	3.457E-02			
Hspa5	-0.877	3.433E-02			
Zfp869	-0.876	3.324E-02			
Eml4	-0.872	2.525E-02			
Nipbl	-0.871	3.649E-03			
Zyg11b	-0.871	2.431E-02			
Naa15	-0.870	2.525E-02			
Zcchc11	-0.869	3.456E-02			
Nfia	-0.869	4.496E-02			
Srrm1	-0.866	1.100E-02			
Wasf2	-0.865	4.521E-02			
Nav1	-0.853	4.602E-02			
Tnrc6b	-0.846	4.165E-02			
Fam120a	-0.844	3.076E-02			
Srrm2	-0.842	3.439E-02			
Ttc28	-0.841	1.727E-02			
Slc25a37	-0.838	1.216E-02			
Hnrnpu	-0.836	1.186E-02			
Sp1	-0.822	1.610E-02			
Cebpz	-0.821	4.863E-03			
Pik3r1	-0.807	2.830E-02			
Mycbp2	-0.805	1.995E-02			
Magt1	-0.792	2.525E-02			
Kmt2e	-0.790	7.461E-03			
Ythdc1	-0.779	4.165E-02			
Hpgds	-0.776	5.802E-03			

Gxylt1	-0.772	4.610E-02
Maf	-0.768	3.621E-03
Scaf11	-0.767	3.534E-02
P4ha1	-0.759	3.648E-02
Snrnp70	-0.757	4.248E-02
Pde3b	-0.754	9.205E-03
Zfp445	-0.751	3.593E-02
Kmt2a	-0.744	1.995E-02
Srsf11	-0.734	1.405E-02
Cntrl	-0.732	4.178E-02
Galnt12	-0.717	4.496E-02
Ncl	-0.708	1.105E-02
Ddx6	-0.702	3.332E-02
Mtdh	-0.699	3.571E-02
Fosb	-0.686	3.525E-02
Ncor1	-0.677	2.525E-02
Egr1	-0.667	3.106E-03
Rbbp6	-0.661	4.892E-02
Mdm4	-0.658	4.178E-02
Epb41l2	-0.650	4.238E-03
Acp2	-0.631	1.374E-02
Itgb1	-0.621	2.559E-02
Glul	-0.619	4.496E-02
Tab2	-0.614	2.020E-02
Pip4k2a	-0.610	1.628E-02
Akap13	-0.596	4.063E-02
Cd86	-0.589	4.915E-02
Son	-0.563	4.602E-02
Srgap2	-0.503	2.331E-02

5.2 Depletion of microglia in the R6/2 mouse model of HD

We further examined microglia in the R6/2 model by attempting to eliminate them from the R6/2 brain and assessing whether this could modify the disease phenotype. Depletion of microglia from the R6/2 brain can be achieved pharmacologically by administering the potent colony-stimulating factor 1 receptor kinase inhibitor (CSF-1Ri), BLZ945 (Hagemeyer et al., 2017). CSF1R signalling is essential to microglia survival and blocking it has become a thoroughly tested target for the elimination of microglia (e.g. Elmore et al., 2014 and Hagemeyer et al., 2017)

To evaluate the dependency of microglia on CSF1R signalling in R6/2 mice, the CSF-1R inhibitor BLZ945 (200 mg/kg) or vehicle was administered daily by oral gavage to 8-week-old R6/2 mice and non-transgenic littermates for 12 days (**Fig. 5a**). Immunohistochemistry was performed on brains collected from these mice two days after cessation of BLZ945 treatment. The myeloid marker Iba1 was used to identify and quantify microglia at 10 weeks of age and this revealed a significant decrease in $Iba1^+$ cell density in non-transgenic controls that received BLZ945 compared to those that only received the vehicle (**Fig 5b**; $\Delta = 54.9 \pm 8.8$ %; p=0.002; one-way ANOVA with Turkey correction). Similarly, a significant decrease in $Iba1^+$ cell density was observed in R6/2 mice that received BLZ945 compared to those that only received the vehicle (**Fig 5b**; $\Delta = 41.8 \pm 11.7$ %; p=0.023; one-way ANOVA with Turkey correction). There was no

significant difference in Iba1$^+$ cell densities between R6/2 mice and non-transgenic controls, although microglia in the R6/2 mice did generally appear larger, with shorter processes.

Complete depletion of microglia was either not achieved with this protocol, or repopulation took place in the two days between BLZ945 cessation and tissue collection. In any case, the Iba1$^+$ cells after BLZ945 treatment appeared activated, with enlarged somata and fewer, shorter processes (**Fig. 5c**).

Over the course of 14 days from the first day of gavage, weight of R6/2 mice was monitored to assess whether BLZ945 treatment would rescue the weight loss observed in R6/2 mice. No differences were observed in the weight of untreated R6/2 mice that received no treatment, vehicle or BLZ945 over this two-week period (**Fig. 6a**). After 12 days of BLZ945 administration through oral gavage, a battery of behavioural tests was performed to examine the effect of the treatment on the locomotor and cognitive performance of R6/2 mice (**Fig. 5a** for experimental overview).

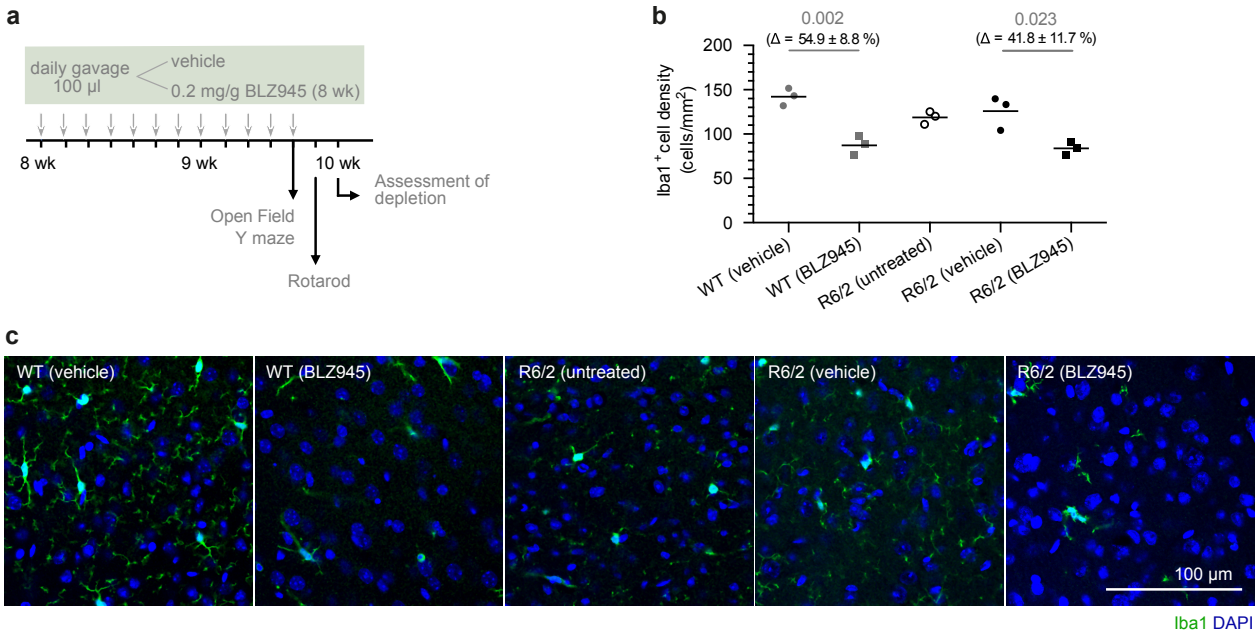

Figure 5 | **Assessment BLZ945-mediated depletion of microglia in female R6/2 mice and non-transgenic littermate controls.** (**a**) Scheme of experimental setup. 8-week-old female R6/2 mice and non-transgenic littermate controls (WT) were treated with BLZ945 for 12 consecutive days by oral gavage. Immunohistochemical assessment of microglia depletion was performed 48 hours after the last application. (**b**) Iba1$^+$ cell density (cells/mm^2) in female R6/2 mice and non-transgenic littermate controls (WT) 48 hours after a 12-day BLZ945 treatment regimen. Data shown as means (n=3). Statistics were done by one-way ANOVA and corrected with the Turkey method for multiple comparisons. (**c**) Representative confocal microscopy images of microglia identified by Iba1 staining. Scale bar: 100 µm.

BLZ945 treatment did not affect the latency of R6/2 mice to fall off a RotaRod, indicating that the motor disturbances assessed by this test were not rescued (**Fig. 6b**). Furthermore, mice from the three groups (R6/2 – untreated, R6/2 + vehicle, R6/2 + BLZ945) exhibited a similar willingness to explore and had similar locomotor activity levels in the Open Field test (**Fig. 6c**). There was also no indication of changes in the anxiety levels in the mice that received BLZ945 treatment, as measured by time that they spent in the centre of the Open Field (**Fig. 6d**). Finally, the cognitive performance of mice that received BLZ945 was measured by the Y Maze test for spontaneous alternations. This test reflects the tendency of mice to spontaneously explore and can mirror deficits in short-term memory. Again, mice from the three treatment groups exhibited similar behaviours (**Fig. 6e**), suggesting that, at least with respect to these readouts and following this treatment regime at this time-point, BLZ945-induced microglia elimination is not protective in the R6/2 mouse model of HD.

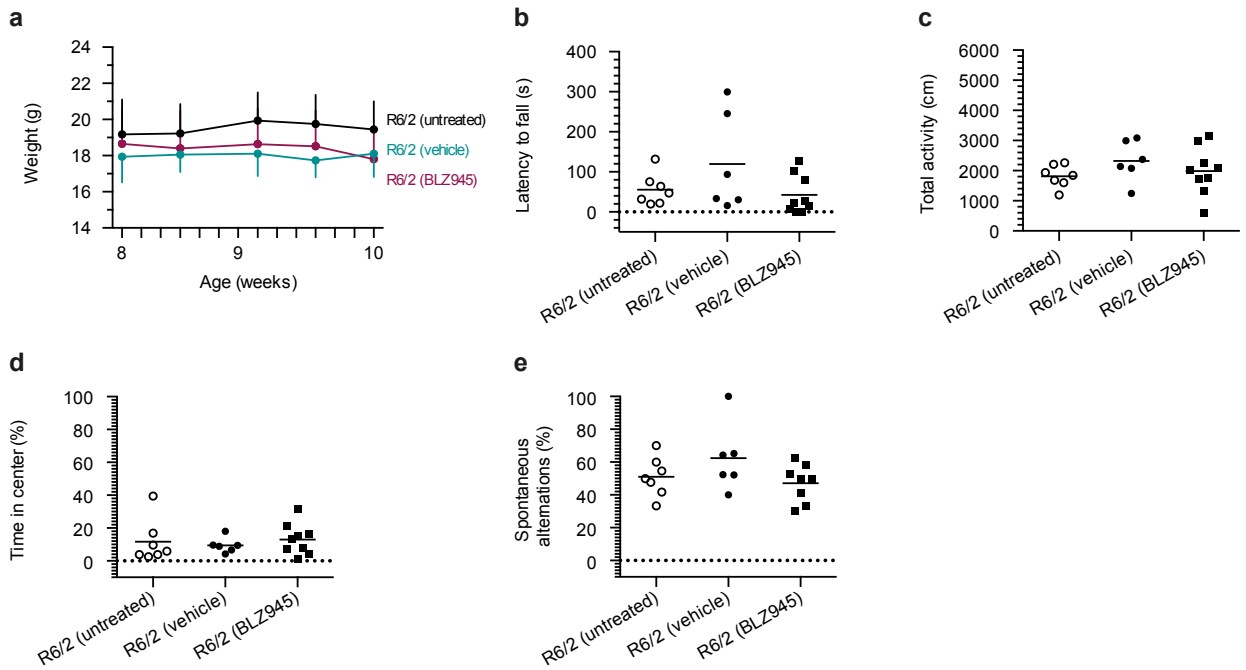

Figure 6 | **Effects of BLZ945-mediated depletion of microglia on R6/2 mice and their non-transgenic littermates.** Tests were performed on female 10-week-old R6/2 mice that received no treatment (n=7), R6/2 mice that received 100 µl daily gavage of vehicle over 12 days (n=6) and R6/2 mice that received daily gavage of 100 µl vehicle + 0.2mg/g BLZ945 over 12 days (n=9). See Fig. 5a for scheme of experimental setup. (**a**) Weight monitoring of untreated R6/2 mice, vehicle-treated R6/2 mice and BLZ945-treated R6/2 mice for the duration of the BLZ945 treatment. Data shown as means ± SD; groups were compared at each time test with multiple t-tests, corrected for multiple comparisons with the Holm-Šídák method. No significant differences were measured. (**b**) Latency to fall off a RotaRod (best of three trials) for untreated R6/2 mice, vehicle-treated R6/2 mice and BLZ945-treated R6/2 mice. (**c**) Distance travelled in an open field by female untreated R6/2 mice, vehicle-treated R6/2 mice and BLZ945-treated

R6/2 mice. (**d**) Proportion of time spent in the centre of an open field by untreated R6/2 mice, vehicle-treated R6/2 mice and BLZ945-treated R6/2 mice. (**e**) Assessment of short-term memory using a Y-maze. The percentage of spontaneous alternations were measured in untreated R6/2 mice, vehicle-treated R6/2 mice and BLZ945-treated R6/2 mice. Data are shown as means (± SD only for (a)) and statistics were done by one-way ANOVA and corrected with the Turkey method for multiple comparisons unless otherwise specified.

5.3 Selective mHTT expression in microglia

5.3.1 The MG-HD mouse model

Examining microglia in R6/2 mice where the mutant protein is ubiquitously expressed does not allow one to distinguish whether these changes are cell-autonomous (i.e. microglia-initiated), reactive (i.e. response of microglia surrounding dysfunctional cells), or both.

In order to take a closer look at the cell-autonomous effect of mHTT expression in microglia, we generated a mouse model in which the mutant protein is specifically targeted to microglia. Cx3cr1$^{tm2.1(cre/ERT2)Jung}$/J mice were crossed with B6.129-Gt(ROSA)26Sor$^{tm1(HD*103Q)Xwy}$/J mice to generate MG-HD mice in which the expression of *HTT*-exon1 with 103 CAG repeats can be activated by tamoxifen-induced Cre-recombinase activity (**Fig. 7a;** refer to section 4.1.1 for mouse line details and section 4.2.1 for details on housing, husbandry and tamoxifen induction of Cre-recombinase activity).

We opted for inducible over constitutive Cre expression to circumvent mHTT expression in peripheral short-lived *Cx3cr1*-expressing myeloid cells (Goldmann et al., 2013) and in neurons, which transiently express *Cx3cr1* during development (https://www.jax.org/strain/025524). Cre-recombinase translocation to the nucleus and subsequent mHTT expression in microglia was induced by subcutaneous administration of tamoxifen to 5-7-week-old MG-HD mice (**Fig. 7a**).

mHTT mRNA was measured at relatively constant levels over time in sorted microglia from 3-, 6- and 12-month-old MG-HD mice (**Fig. 7b**). Notably, the levels of *mHTT* in the MG-HD model were much lower than those measured in sorted microglia from R6/2 transgenic mice that ubiquitously express human mHTT under its native IT15 promoter and exhibit a very robust phenotype (Mangiarini et al., 1996; **Fig. 7b**).

To ensure that mHTT expression was eliminated from peripheral *Cx3cr1*-expressing myeloid cells, protein levels of mHTT were measured by TR-FRET in CD45$^+$CD11b$^+$ splenocytes 3 months after tamoxifen injection. As expected, mHTT expression was undetectable in splenocytes of MG-HD mice, since a tamoxifen pulse is not sufficient to maintain long-term expression of mHTT in

Cx3cr1-expressing peripheral myeloid cells that are constantly replaced by bone-marrow or splenic precursors (**Fig. 7c**). On the contrary, high levels of mHTT expression were detected in $CD45^{+}CD11b^{+}$ splenocytes of a 10-week-old R6/2 positive control mice that constitutively express mHTT in all cells of the body.

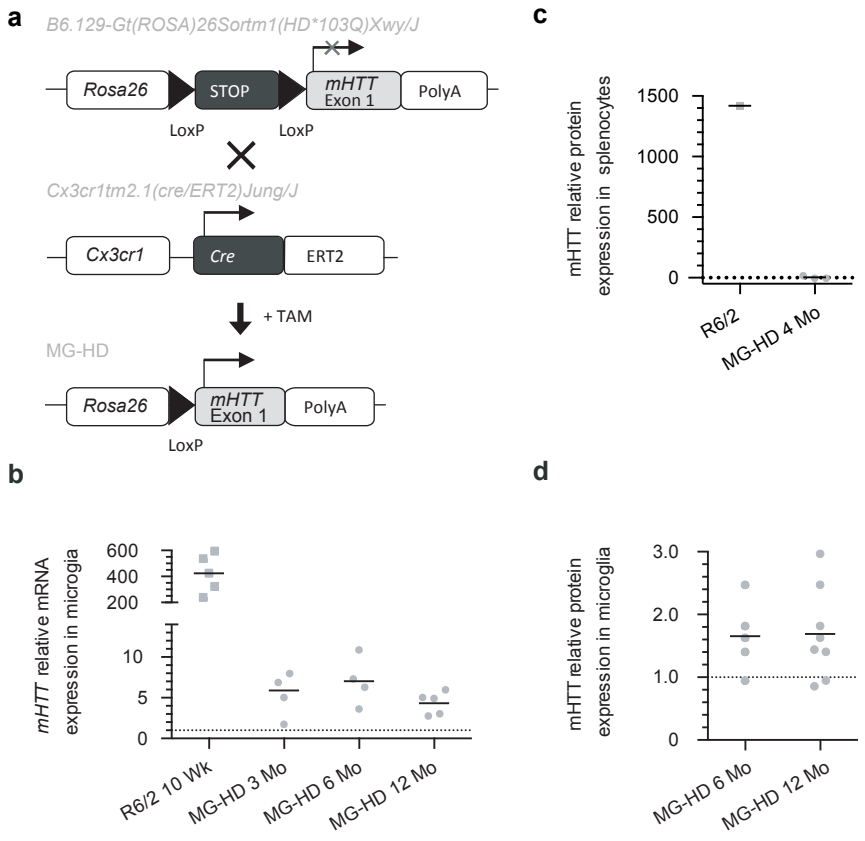

Figure 7 | **Targeting expression of mHTT to microglia in MG-HD mice.** (**a**) Breeding scheme for conditional MG-HD mice in which expression of mHTT-exon1 is targeted to the Rosa26 locus that contains the endogenous *Rosa26* promoter, a loxP flanked transcriptional STOP sequence and *mHTT-exon1* with 103 mixed CAA/CAG repeats encoding a polyglutamine expansion. The expression of *mHTT-exon1* was dependent on *Cx3cr1*-driven Cre recombinase activation and recombination was induced with subcutaneous tamoxifen (TAM) injections in 5-7-week-old mice. (**b**) qPCR for relative *mHTT* mRNA expression in FACS-sorted microglia from 10-week-old R6/2 mice (n=5) and 3, 6 and 12-month- old MG-HD mice (n=4, 4 and 5 respectively) over their respective controls (n=4). (**c**) TR-FRET for mHTT protein expression in FACS-sorted $CD11b^{+}$ splenocytes from 12-week-old R6/2 mice (n=1) and 4-month-old MG-HD mice (n=3). (**d**) TR-FRET for relative mHTT protein expression in Percoll-enriched microglia from 6 and 12-month-old MG-HD mice (n=5 and 8) and their respective controls (n=3 and 5). Data shown as means of expression levels in test groups over their respective controls.

5.3.2 Brain immune cell composition of MG-HD mice

Infiltration of peripheral immune cells to the CNS has been shown in various neurological diseases (Ransohoff, 2016). To examine whether mHTT expression in microglia alone can induce the infiltration of peripheral immune cells into the CNS, we examined the CNS immune cell composition of MG-HD mice.

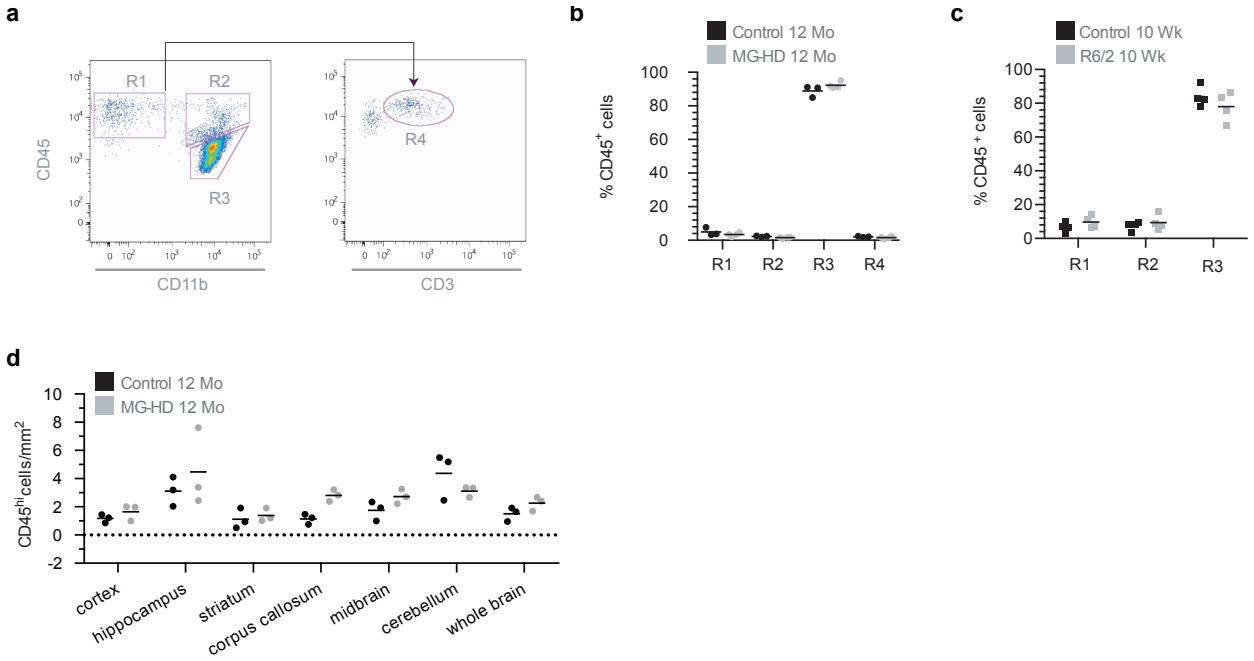

Figure 8 | **Peripheral immune cells do not infiltrate the brains of 12-month-old MG-HD mice and 10-week-old R6/2 mice.** (**a**) Flow cytometry gating strategy for $CD45^{+}CD11b^{-}$ leukocytes (R1), $CD45^{hi}CD11b^{+}$ (R2) myeloid cells $CD45^{lo}$ $CD11b^{+}$ (R3) microglia, $CD45^{+}CD11b^{-}CD3^{+}$ T cells (R4). Example taken from control 12-month-old MG-HD mice. (**b**) Flow cytometry analysis of *ex vivo* isolated brain leukocytes from 12-month-old MG-HD mice (n=4) and their respective controls (n=3) showing relative proportions of main brain leukocyte populations defined in (a). Graphs show representative data from three independent experiments. (**c**) Flow cytometry analysis of *ex vivo* isolated brain leukocytes from 10-week-old R6/2 mice (n=4) and their respective controls (n=4) showing relative proportions of main brain leukocyte populations defined in (a). (**d**) Quantification of $CD45^{hi}$ cells in histological sections of the brain of 12-month-old MG-HD mice and their respective controls (n=3). Sections at 5.22 and 4.54 mm interaural were examined for all brain regions except the cerebellum (2.88 mm interaural). Data shown as means, unpaired Student *t* tests corrected with the Holm-Šídák method for multiple comparisons were performed and no statistical significance was measured.

Isolated immune cells from the brains of 12-month-old MG-HD mice were analysed by flow cytometry (**Fig. 8**). The relative proportions of microglia, myeloid cells and $CD11b^{-}$ non-myeloid leukocytes were comparable between MG-HD mice and controls (**Fig. 8b**). Similar results were

observed in the brains of 10-week-old R6/2 mice and controls (**Fig. 8c**). In addition, brain sections from 12-month-old MG-HD mice were stained with an anti-CD45 antibody and $CD45^{hi}$ cells were counted in various brain regions. No statistically significant increase in $CD45^{hi}$ cells was observed in brains of these mice compared with controls, indicating that peripheral immune cells do not infiltrate into the MG-HD brain at 12 months (**Fig. 8d**). These results in the R6/2 model of HD are in line with human data in which no evidence of peripheral immune cell infiltration was apparent (Silvestroni et al., 2009). They come to show that the microglial transcriptional responses described in 5.1 are a result of local brain changes rather than a response to the infiltration of immune cells from the periphery.

5.3.3 Changes in microglia morphology, distribution and P2Y12 receptor expression

Microglia responses commonly present as changes in cell morphology and distribution (for review: Perry, 2010 and Ransohoff, 2016), which prompted us to investigate microglia of 12-month-old MG-HD mice by histology. In 12-month-old MG-HD mouse brains, $Iba1^+$ microglia with enlarged somata and thick ramifications were detected both in the striatum and in the cortex (**Fig. 9a**), areas that are most affected in HD. In these regions, there was also an increase of $Iba1^+$ cell density (**Fig. 9b**) and volume coverage of microglia (**Fig. 9c**). These changes were more pronounced in the striatum than in the cortex, but not present in the cerebellum (**Fig. 9b, c**). This suggests regional effects in affected brain regions.

The increased density of microglia in the striata and cortices of MG-HD mice may result from greater levels of cell proliferation. To examine this, the fraction of proliferating $Iba1^+$ cells that also exhibited Ki67 immunoreactivity was quantified. No significant differences in Iba^+Ki67^+ double-positive cells were observed in the cortex, striatum and cerebellum of MG-HD mice at 12 months of age compared to controls (**Fig. 9d**).

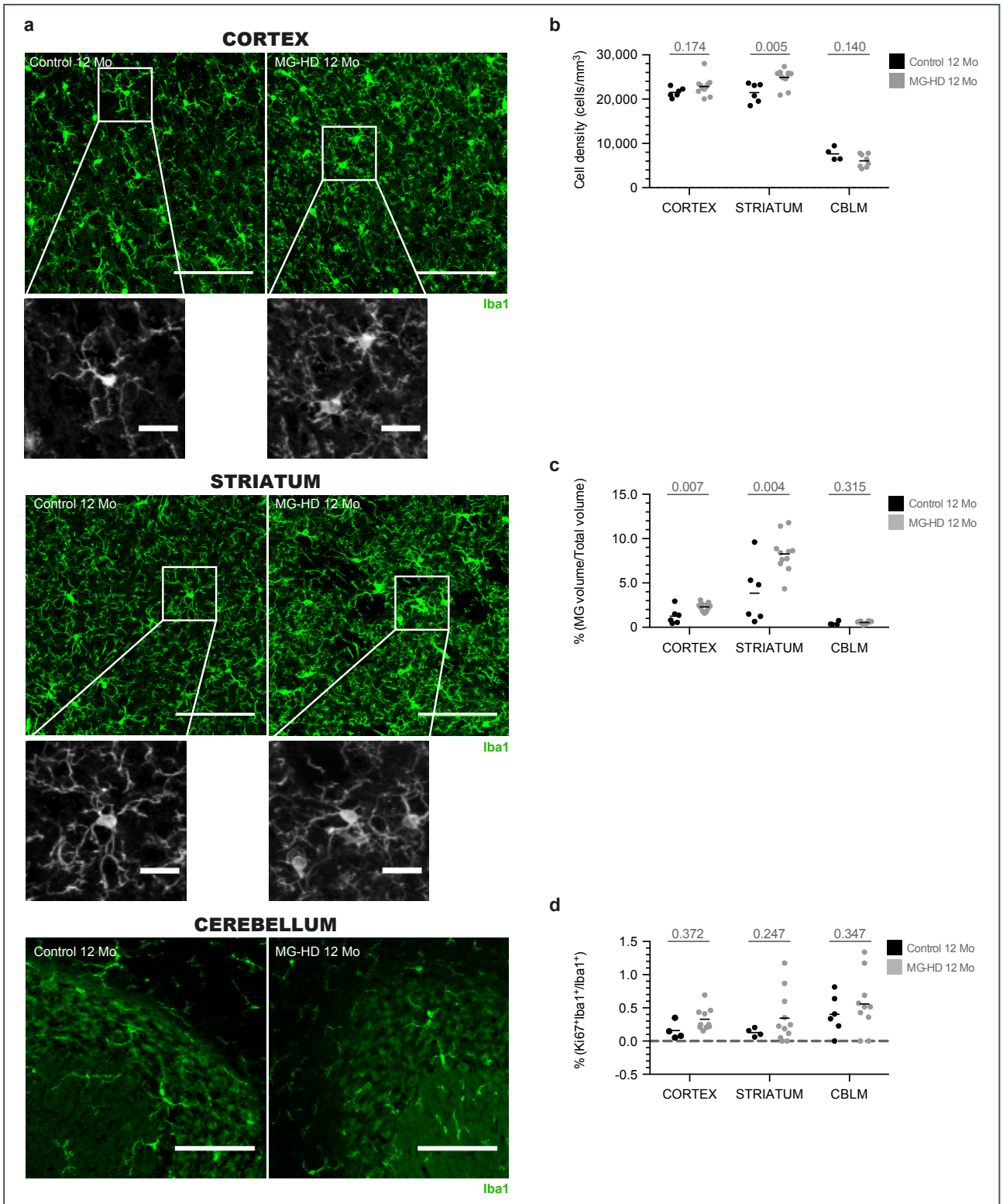

Figure 9 | **Targeted mHTT expression in microglia causes changes in cell morphology and distribution.** (**a**) Representative images of microglia identified by Iba1 staining in the cortex, striatum and cerebellum of 12-month-old MG-HD mice and their respective controls. Scale bars: 100 µm (20 µm for magnifications). (**b**) Density of microglia ($Iba1^+DAPI^+$ nuclei) in the cortex, striatum and cerebellum of 12-month-old mice (n=6 and 11 for control and MG-HD, respectively). (**c**) Relative coverage of microglia (Iba1-immunoreactive volume) in the cortex, striatum and cerebellum of 12-onth-old mice (n=6 and 11 for control and MG-HD, respectively). (**d**) Quantification of the

proportion of proliferating microglia ($Iba1^{+}Ki67^{+}$) in the cortex, striatum and cerebellum of MG-HD microglia (n=11) and their respective controls (n=6). Data shown as means, all *p* values were determined by unpaired Student *t* tests and corrected with the Holm-Šídák method for multiple comparisons.

Recent work from our lab has revealed decreased $P2Y_{12}$ immunoreactivity in microglia from Alzheimer's disease or multiple sclerosis brains (Mildner et al., 2017a). Therefore, I proceeded to examine whether a similar effect could be seen in microglia from 12-month-old MG-HD mice. I measured a decrease of $P2Y_{12}$ signal intensity in the cortex and in the striatum of 12-month-old MG-HD mice compared with controls (**Fig. 10a, b**).

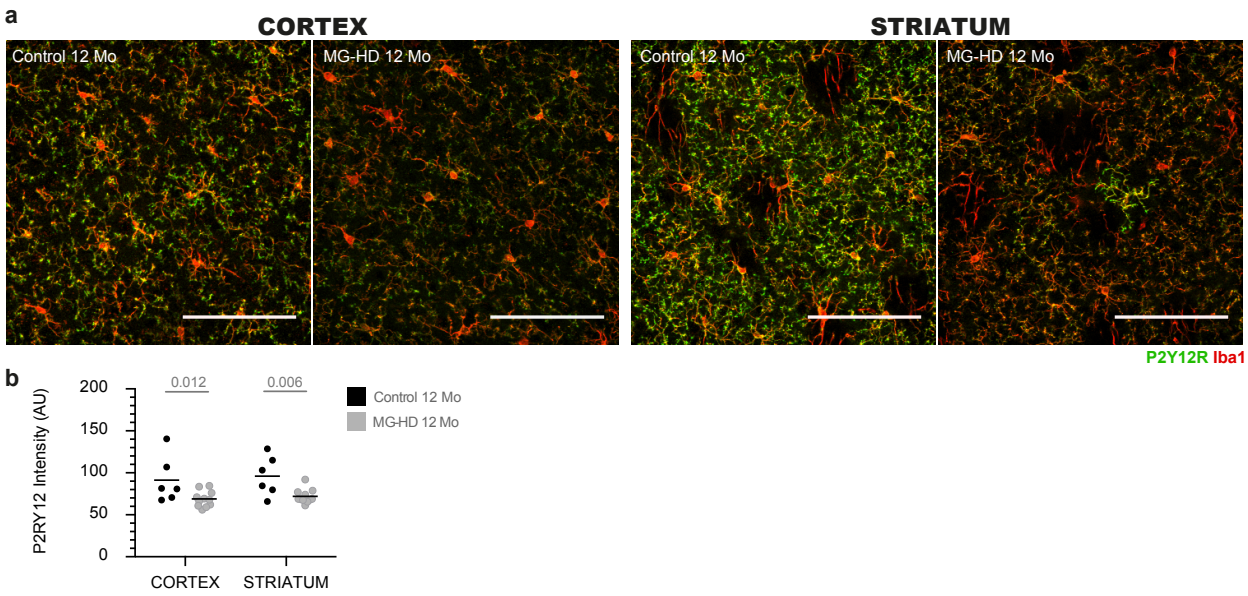

Figure 10 | **Targeted expression of mHTT to microglia results in decreased cell-surface expression of $P2Y_{12}$ receptor.** (**a**) Representative images of P2Y12 receptor (green) and Iba1 (red) expression in MG-HD microglia in the cortex and striatum of 12-month-old MG-HD mice and their respective controls. Scale bars: 100 µm. (**b**) Computational threshold analysis of P2Y12 receptor signal intensity in the cortex and the striatum (shown in (a), n=6 and 11 for control and MG-HD, respectively). Data shown as means, all *p* values were determined by unpaired Student *t* tests and corrected with the Holm-Šídák method for multiple comparisons. AU: arbitraty units.

5.3.4 Transcriptomic profiles of microglia isolated from MG-HD mice

I performed RNA sequencing of microglia isolated from MG-HD mice at 3, 6 and 12 months of age following the same methodology as with R6/2 mice (**Fig. 4**). Importantly, I did not observe any changes in the transcriptomic profile of microglia from MG-HD mice compared to controls (**Fig. 11a-c**). With time, the expression levels of *Spi1*, *Cebpa* and *Cebpb* did increase, but this effect did not reach statistical significance.

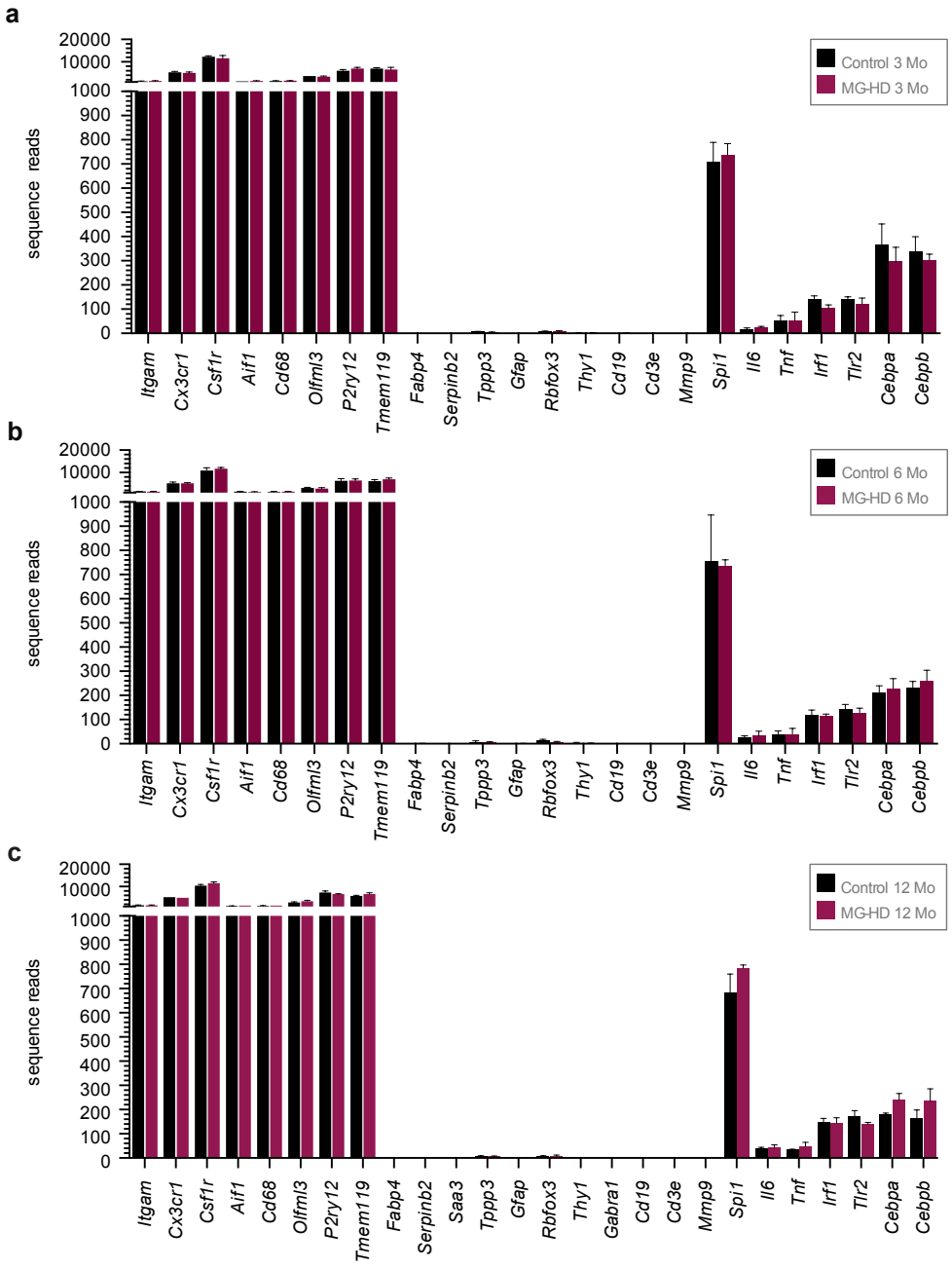

Figure 11 | **Transcriptional profiles of microglia isolated from 3-, 6-, and 12-month-old MG-HD mice and their respective controls.** (**a**) mRNA expression levels of selected genes in microglia sorted from 3-month-old MG-HD mice (n=4) compared to controls (n=4). (**b**) mRNA expression levels of selected genes in microglia sorted from 6-month-old MG-HD mice (n=4) compared to controls (n=4). (**c**) mRNA expression levels of selected genes in microglia sorted from 12-month-old MG-HD (n=3) mice compared to controls (n=4). Data in shown as mean sequence reads ± SD with FDR-adjusted *p* values from the Wald tests.

5.3.5 *Expression of mHTT in microglia: Effect on astrocytes*

I extended the histological analysis to astrocytes in the cortex and the striatum to assess whether mHTT expression in microglia could influence other cell types as a secondary effect.

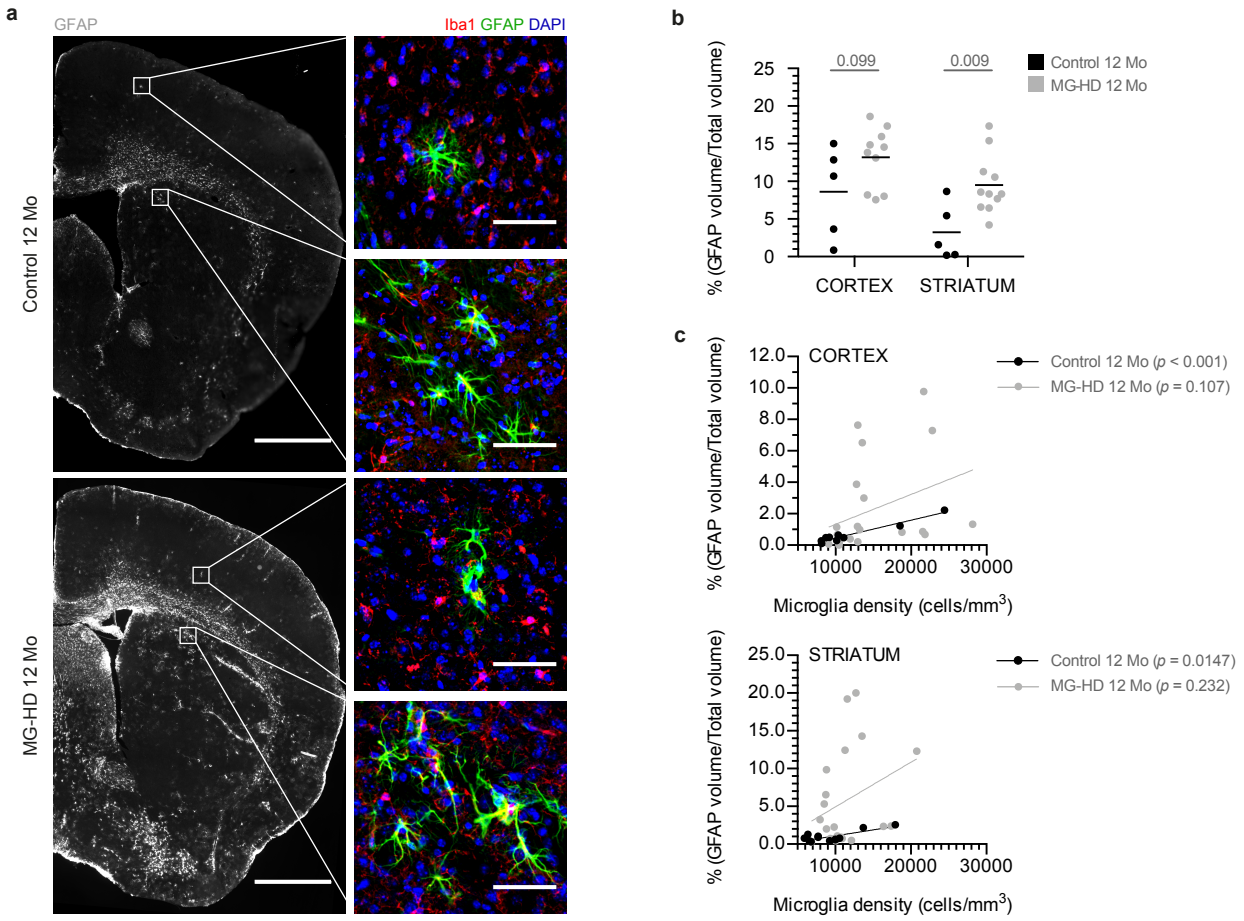

Figure 12 | **Effects of targeted expression of mHTT to microglia on astrocytes at 12 months of age.** (**a**) Left: representative immunofluorescent images of GFAP immunoreactivity in MG-HD mice (bottom) and their respective controls (top). Right: Magnifications of GFAP immunoreactive astrocytes (green) and Iba1 immunoreactive microglia (red) in the cortex or the striatum of MG-HD mice and controls. Scale bars: 1mm for images of whole hemispheres (left) and 50 µm for magnifications (right). (**b**) Relative coverage of astrocytes - GFAP-immunoreactive volume shown in (a) - in the cortex and the striatum of 12-month-old MG-HD mice with panoramic imaging (see methods). 5 control and 10 MG-HD mice were used for quantification and each point represents the mean GFAP coverage per mouse. (**c**) Correlation of GFAP-immunoreactive volume and microglia density in two areas of the cortex (CTX-B1 and CTX-B2 – see methods; top) and two areas of the striatum (STR-B1 and STR-B2 see methods; bottom) in 12-month-old MG-HD mice (n=5) and their respective controls (n=11), points represents GFAP coverage and microglia density in each region imaged. Data shown as means for per mouse (b) or as individual image measures (c), *p* values were determined by unpaired Student *t* tests for (b) and by Spearman correlation for (c).

Clusters of GFAP-immunoreactive astrocytes were present in the cortex and in the striatum of MG-HD mice at 12 months of age (**Fig. 12a**). In MG-HD mice, the total volume coverage of GFAP immunoreactivity was significantly increased compared to controls in the striatum when panoramic imaging was performed (**Fig. 12b**). These results suggest that astrocytes respond to mHTT-induced microglia changes in the MG-HD brain.

To assess whether specific areas of increased GFAP-immunoreactivity were associated with greater densities (clusters) of microglia, we measured percentage GFAP coverage in relation to microglia density in two areas of the cortex and two areas of the striatum (CTX-B1, -B2 and STR-B1, -B2; see Methods). In control mice at 12 months of age, microglia density positively correlated with GFAP immunoreactivity in the cortex and the striatum ($p<0.001$ in cortex and $p=0.0147$, respectively, **Fig. 12c**). In MG-HD mice this correlation was not significant, however, the slope remained positive (**Fig. 12c**)

5.3.6 Expression of mHTT in microglia: Effect on striatal neurons and gross behavioural/anatomical effects

5.3.6.1 Secondary effects of microglia mHTT expression on neurons in 12-month old MG-HD mice

Next, we assessed possible neuronal changes caused by mHTT expression in microglia in the striata of 12-month-old MG-HD mice.

Striatal medium spiny neurons (MSNs) are a particularly vulnerable population in HD and a marked MSN loss occurs as the disease progresses (Reiner et al., 1988). MSNs in the striatum can be visualized by immunohistochemistry using an anti-DARPP-32 antibody. We quantified the minimum distance between DARPP-32^+ cell bodies in the striatal grey matter and observed no change in the average minimum distance between DARPP-32^+ neurons in the striatum of 12-month-old MG-HD mice (**Fig. 13a, b**), indicating that the density/distribution of these cells remained constant.

Another measure of cortical or striatal neuron loss or dysfunction in HD might be reflected in the number of corticostriatal synapses of MG-HD mice in comparison to their respective controls. We investigated this with immunohistochemistry using an antibody raised against the post-synaptic marker PSD-95. Immunoreactive puncta representative of single synaptic termini were imaged at

high resolution (**Fig. 13c**). We found no evidence of synaptic loss when quantifying the average minimum distance between termini in the striatum (**Fig. 13d**).

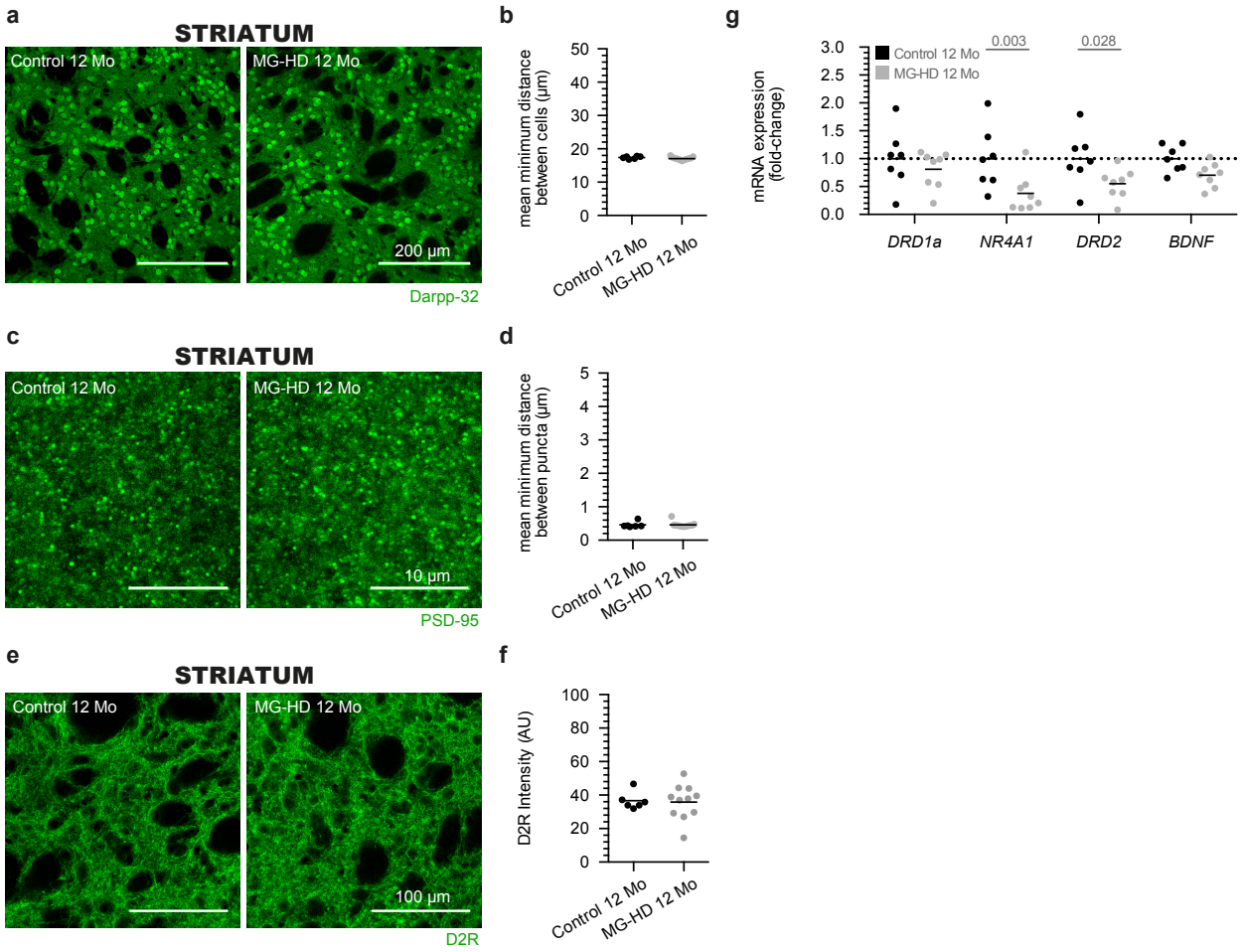

Figure 13 | **Targeted expression of mHTT to microglia: effect on striatal neurons and gross behavioural/anatomical effects.** (**a**) Representative immunofluorescent images of striatal `medium spiny neurons (Darpp32^{+}) in 12-month-old MG-HD mice and controls. Scale bars: 200 µm. (**b**) Quantification of the mean minimum distance between striatal medium spiny neurons (Darpp32^{+}) shown in (a), 6 control and 11 MG-HD mice were used for quantification. (**c**) Representative immunofluorescent images of PSD-95 immunoreactivity in the striatum of 12-month-old MG-HD mice and their respective controls. Scale bars: 10 µm. (**d**) Mean minimum between PSD-95 immunoreactive post-synaptic puncta (shown in b), 6 control and 11 MG-HD mice were used for quantification. (**e**) Representative immunofluorescent images of D2R immunoreactivity in the striatum of 12-month-old MG-HD mice and their respective controls. Scale bars: 100 µm. (**f**) Quantification of D2R signal intensity shown in (e) in the striatum of 6 control and 11 MG-HD. (**g**) qPCR for *Drd1a, Nr4a1, Drd2, Bdnf* mRNA expression in whole brain lysates of 3, 6 and 12-month-old MG-HD mice (n=9) and their respective controls (n=7). Data shown as means. For Statistics were done by unpaired Student *t* tests and corrected with the Holm-Šídák method for multiple comparisons. AU: arbitrary units.

As a further means of measuring neuronal dysfunction, we measured the levels of dopamine D2 receptor in the striatum of 12-month-old MG-HD mice. Decreased dopamine D2 receptor (D2R) in the striatum is characteristic of patients with HD and this observation has been recapitulated on an mRNA level in R6/1, R6/2 and YAC128 mouse models of HD (for review see: Cepeda et al., 2014). We observed no reduction in D2 receptor signal intensity in the striatum of 12- month-old MG-HD mice by immunohistochemistry indicating that on a protein level, expression levels are not affected (**Fig. 13e, f**). Nevertheless, on a transcriptional level, *Drd2* and also other neuronal genes commonly affected in HD (*Drd1*, *Nr4a1*, and *Bdnf*) were downregulated in whole brain lysates at 12 months of age (**Fig. 13g**).

5.3.6.2 Weight monitoring and motor performance of MG-HD mice

HD patients suffer weight loss and exhibit motor abnormalities as their disease progresses and these effects are recapitulated widely in mouse models of HD (e.g. R6/2, YAC128) where the mutant protein is ubiquitously expressed in all cells of the body (Sawiak et al., 2012).

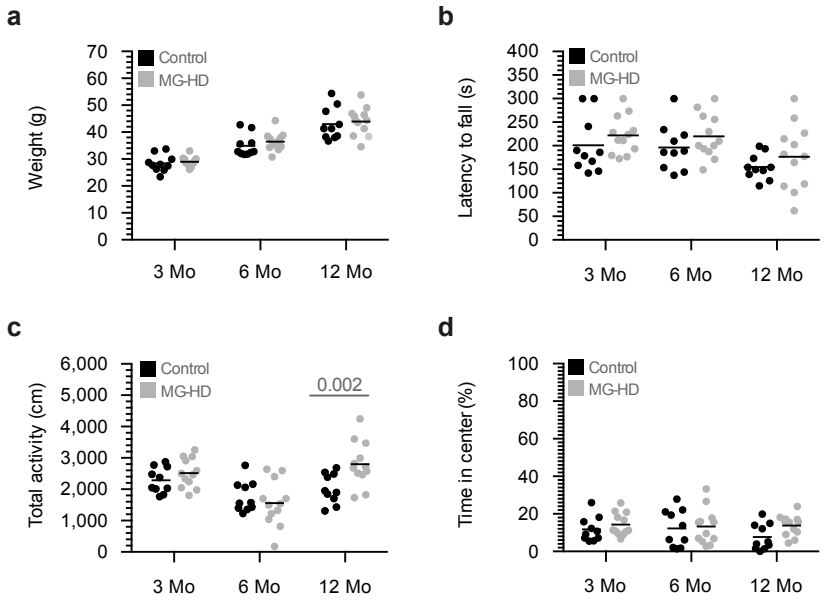

Figure 14 | **Weight monitoring and motor performance of male MG-HD mice.** (**a**) Weight monitoring of male MG-HD (n=12) mice and their respective controls (n=10) at 3, 6 and 12 months of age. (**b**) Latency to fall off a RotaRod (best of three trials) for male MG-HD (n=12) mice and their respective controls (n=10) at 3, 6 and 12 months of age. (**c**) Distance travelled in an open field by male MG-HD (n=12) mice and their respective controls (n=10) at 3, 6 and 12 months of age. (**d**) Time spent in the center of an open field by male MG-HD (n=12) mice and their respective controls (n=10) at 3, 6 and 12 months of age. Data shown as means. Statistics were done by 2-way ANOVA and corrected with the Šídák method for multiple comparisons.

Weight monitoring was performed for male MG-HD mice over time (3,6 and 12 months of age), but there was no evidence of progressive weight loss (**Fig. 14a**). The motor performance of MG-HD mice was also monitored over time through the use of the RotaRod and Open Field behavioural tests. The RotaRod test read-out, measured as the latency of mice to fall off the RotaRod over three consecutive trials, would reflect changes in motor coordination. We observed no changes in the performance of MG-HD mice on the RotaRod as a result of mHTT expression in microglia alone (**Fig. 14b**).

When assessing the locomotor activity of MG-HD mice over time and their tendency to explore through the Open Field test, no changes were observed when compared to controls. Although an increase was observed at 12-month of age in the distance travelled by MG-DH mice (**Fig. 14c**), this increase was not observed in a second cohort of male mice in which behavioural tests were performed at 12, 18 and 22 months of age (**Fig. 19h**) nor in female MG-HD mice at 3, 6 and 12 months (**Fig. 15c)**. Finally, the proportion of time MG-HD spent in centre and most exposed region of the Open Field, that would possibly reflect alterations in anxiety levels of these mice, also remained unchanged (**Fig. 14d**).

A separate cohort of female MG-HD mice and their respective controls at 3, 6 and 12 months of age was also assessed for any overt behavioural phenotypes to check if there was an effect of gender on these results. Again, weight, performance of the mice in the Open Field (both in terms of total distance travelled and in terms of the proportion of the time the mice spent in the center of the field) and performance of the mice on a RotaRod were similar in the two groups over time (**Fig. 15a-d**). The increased total distance travelled in the Open Field in the male MG-HD cohort (**Fig. 14c**) at 12 months of age was not seen in the female mice (**Fig. 15c**).

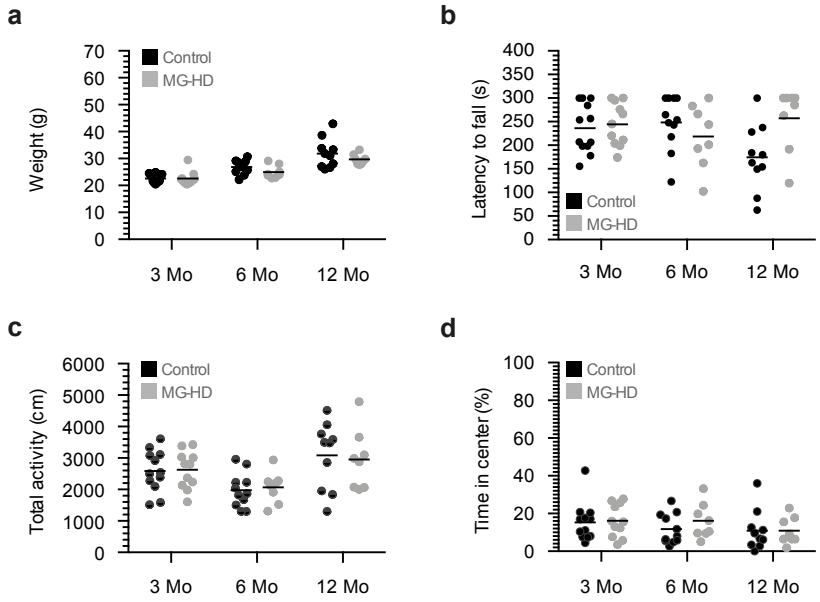

Figure 15 | **Weight monitoring and motor performance of female MG-HD mice.** (**a**) Weight monitoring of female MG-HD (n=8) mice and their respective controls (n=10) at 3, 6 and 12 months of age. (**b**) Latency to fall off a RotaRod (best of three trials) for female MG-HD (n=10-12) mice and their respective controls (n=8-10) at 3, 6 and 12 months of age. (**c**) Distance travelled in an open field by male MG-HD (n=8-10) mice and their respective controls (n=10-12) at 3, 6 and 12 months of age. (**d**) Time spent in the center of an open field by female MG-HD (n=8-10) mice and their respective controls (n=10-12) at 3, 6 and 12 months of age. Data shown as means. Statistics were done by 2-way ANOVA and corrected with the Šídák method for multiple comparisons.

5.3.6.3 MRI of MG-HD mouse brains at 12 months of age

To further address whether mHTT expression in microglia can contribute to an HD-like neurological phenotype, we investigated hallmark neuroimaging changes. T2-weighted MRI of the brain is a method for quantifying gross neuroanatomical changes and disease progression in HD mice (Steventon et al., 2016). Representative MRI scans from 12-month-old MG-HD mice (n=10) and their respective controls (n=8) are shown in **Fig. 16**.

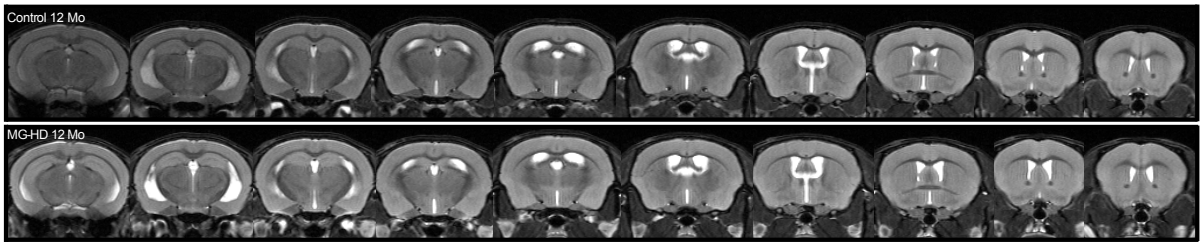

Figure 16 | **Representative T2-weighted magnetic resonance images of 12-month-old MG-HD mice and controls.**

At 12 months of age, there was no marked atrophy in the brain of MG-HD mice, nor any changes in T2-mean grey level intensities. This was determined by a meticulous analysis of the MRI scans for volume and T2-mean grey level intensity changes performed by our collaborators Dr. Stefan Paul Koch and Dr. Philipp Boehm-Sturm (Department of Experimental Neurology, Center for Stroke Research Berlin, Charité Core Facility). For all brain regions mapped by the Allen template, no significant differences in volume (determinant of the Jacobian matrix (JD) volume changes and T2 volume) were detected between groups with Family-Wise-Error correction (cluster threshold k=10) or FDR correction (less stringent control of Type I errors). The same anatomical labelling approach with both Bonferroni and FDR corrections also revealed no statistical differences in T2-mean grey level intensities for any anatomical region.

5.4 Effects of mHTT expression in microglia in aged mice

Our data so far did not exclude the possibility that an HD-like phenotype might develop in MG-HD mice at an older age. To examine whether any effects would accumulate over time, we extended some of our key analyses to aged mice.

In both control and MG-HD mice at 22 months, Iba1$^+$ microglia appeared less ramified than those in 12-month-old brains, with enlarged somata and thicker/shorter ramifications (**Fig. 17a** compared to **Fig. 9a**). When comparing MG-HD mice to controls, a significant reduction in microglia density was observed in the cortex, but not striatum or cerebellum (**Fig. 17b**). However, for all brain regions the volume covered by microglia was not different between genotypes (**Fig. 17c**). The proportion of proliferating Ki67$^+$Iba1$^+$ microglia were also comparable between the two groups (**Fig. 17d**) and we detected no difference the intensity of the $P2Y_{12}$ signal in microglia from cortex and striatum of 22-month-old MG-HD and control mice (**Fig. 17e**).

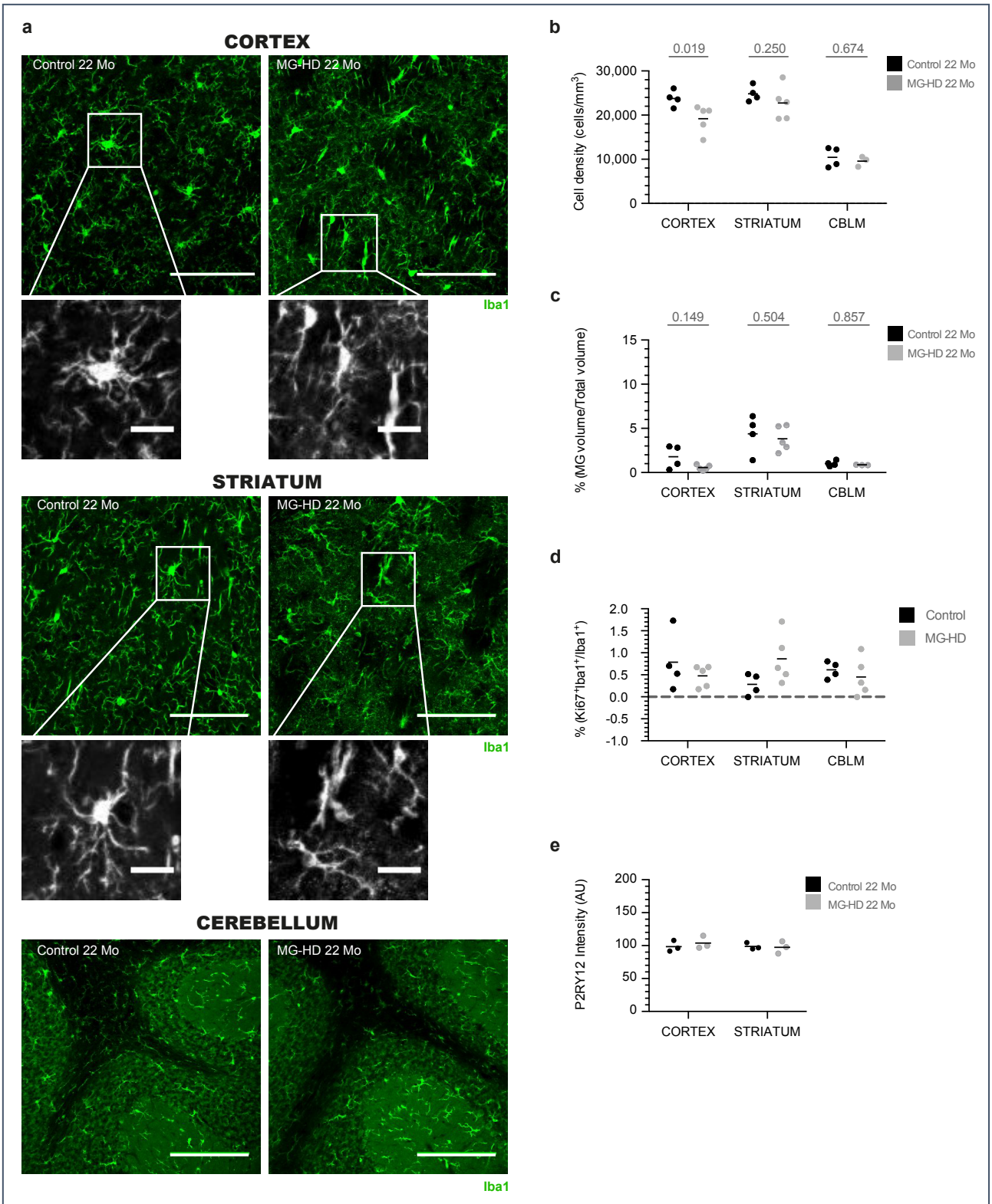

Figure 17 | **Microglia in 22-month-old MG-HD mice and their respective controls.** (**a**) Representative images of microglia identified by Iba1 staining in the cortex, striatum and cerebellum of 22-month-old MG-HD mice and their respective controls. Scale bars: 100 µm (20 µm for magnifications). (**b**) Density of microglia ($Iba1^+DAPI^+$ nuclei) in the cortex, striatum and cerebellum of 22-month-old mice (n=4 and 5 for control and MG-HD, respectively). (**c**) Relative coverage of microglia (Iba1-immunoreactive volume) in the cortex, striatum and cerebellum of 22-onth-old mice (n=4 and 3-5 for control and MG-HD, respectively). (**d**) Quantification of the proportion of proliferating

microglia ($Iba1^+Ki67^+$) in the cortex, striatum and cerebellum of MG-HD microglia (n=5) and their respective controls (n=4). (**e**) Computational threshold analysis of P2Y12 receptor signal intensity in the cortex and striatum of 22-month-old MG-HD mice and their respective controls (n=3). Data shown as means, all *p* values were determined by unpaired Student *t* tests and corrected with the Holm-Šídák method for multiple comparisons.

Next, we wanted to determine the effects of mHTT expression in microglia on astrocytes in 22-month-old mice. No significant differences were detected in the volumes covered by astrocytes in the cortex and striatum of 22-month-old MG-HD mice compared with controls (**Fig. 18a-b)**. It should be noted that the astrocyte coverage generally increased with age in the striatum (12-month control $GFAP^+$ volume: 3.23±3.71 %; 22-month control striatum $GFAP^+$ volume: 21.73±4.59 %) and in the cortex (12-month control $GFAP^+$ volume: 8.61±6.07 %; 22-month control striatum $GFAP^+$ volume: 29.17±11.69 %).

To examine whether areas of increased GFAP-immunoreactivity co-localized with areas where microglia were found in greater densities (clusters) in aged mice, we measured the percentage GFAP of coverage in relation to microglia density in two areas in the cortex and two areas in the striatum (CTX-B1, -B2 and STR-B1, -B2; see Methods). Microglia density positively correlated with GFAP immunoreactivity in the cortex and negatively correlated with GFAP immunoreactivity in the striatum in aged MG-HD and control mice, but none of this was statistically significant (**Fig 18c**).

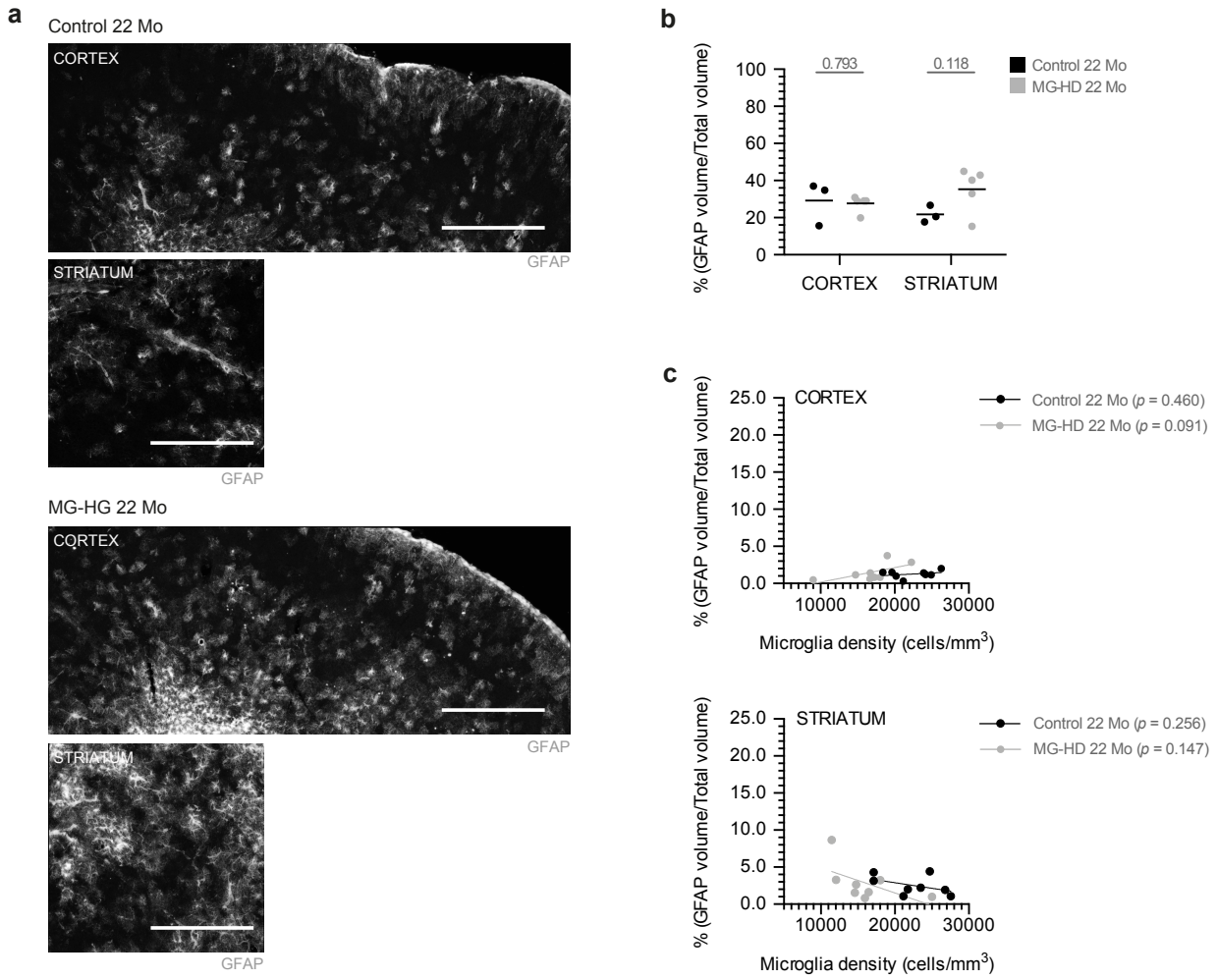

Figure 18 | **Effects of targeted expression of mHTT to microglia on astrocytes at 22 months of age.** (**a**) Representative immunofluorescent images of GFAP immunoreactivity in MG-HD mice (bottom) and their respective controls (top) at 22 months of age. Scale bars: 500 μm (**b**) Relative coverage of astrocytes - GFAP-immunoreactive volume shown in (a) - in the cortex and the striatum of 22-month-old MG-HD mice. 3 control and 5 MG-HD mice were used for quantification and each point represents the mean GFAP coverage per mouse (**c**) Correlation of GFAP-immunoreactive volume and microglia density in two areas of the cortex (CTX-B1 and CTX-B2 – see methods; top) and two areas of the striatum (STR-B1 and STR-B2 see methods; bottom) in 12-month-old MG-HD mice (n=4) and their respective controls (n=4), points represents GFAP coverage and microglia density in each region imaged. Data shown as means per mouse for (b) or as individual image measures (c), *p* values were determined by unpaired Student *t* tests for (b) and by Spearman correlation for (c).

We additionally checked for secondary effects of mHTT expression in microglia on striatal neurons at 22 months of age in MG-HD mice and detected no change in the density of Darpp-32^{+} striatal neurons (**Fig. 19a, b**), PSD-95^{+} synapse density (**Fig. 19c, d**), or the overall intensity of D2R immunoreactivity (**Fig. 19e, f**) in MG-HD mice compared with controls. Finally, no weight

loss (**Fig. 19g)** was observed in MG-HD aged mice and their behaviour in the open field test (**Fig. 19h-i**) as well as on the RotaRod (**Fig. 19j**) was comparable to that of controls.

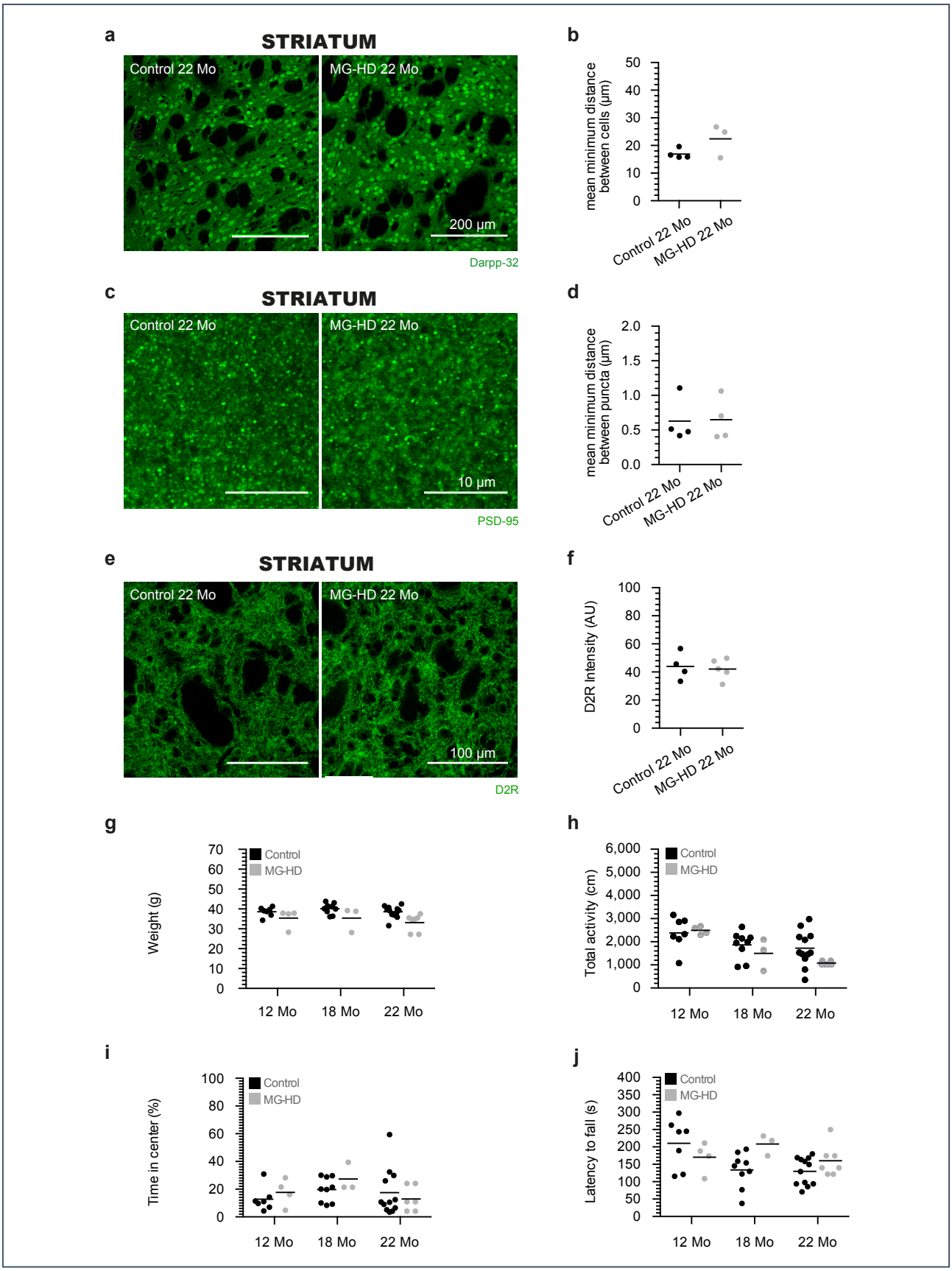

Figure 19 | **Targeted expression of mHTT to microglia: effect on striatal neurons and gross behavioural effects.** (**a**) Representative immunofluorescent images of striatal medium spiny neurons (Darpp32^{+}) in 22-month-old MG-HD mice and controls. Scale bars: 200 μm. (**b**) Quantification of the mean minimum distance between striatal medium spiny neurons (Darpp32^{+}) shown in (a), 4 control and 3 MG-HD mice were used for quantification. (**c**) Representative immunofluorescent images of PSD-95 immunoreactivity in the striatum of 22-month-old MG-HD mice and their respective controls. Scale bars: 10 μm. (**d**) Mean minimum between PSD-95 immunoreactive post-synaptic puncta (shown in b), 4 control and 4 MG-HD mice were used for quantification. (**e**) Representative immunofluorescent images of D2R immunoreactivity in the striatum of 22-month-old MG-HD mice and their respective controls. Scale bars: 100 μm. (**f**) Quantification of D2R signal intensity shown in (e) in the striatum of 4 control and 5 MG-HD. (**g**) Weight monitoring of male MG-HD mice and their respective controls at 12, 18 and 22 months of age. (**h**) Distance travelled in an open field by male MG-HD mice and their respective controls at 12, 18 and 22 months of age. (**i**) Time spent in the centre of an open field by male MG-HD mice and their respective controls at 12, 18 and 22 months of age. (**j**) Latency to fall off a RotaRod (best of three trials) for male MG-HD mice and their respective controls at 12, 18 and 22 months of age. For (b, d and f) statistics were done by unpaired Student *t* tests and corrected with the Holm-Šídák method for multiple comparisons. For (g-j) statistics were done by 2-way ANOVA and corrected with the Šídák method for multiple comparisons.

6. Discussion

This study aimed to directly address the question of how expression of mHTT in microglia contributes to HD pathogenesis and disease progression. The R6/2 model was used to examine microglia changes in response to ubiquitous mHTT expression and to assess whether HD core pathological features could be rescued upon microglia depletion. The MG-HD model was used to pinpoint cell-autonomous effects of mHTT expression in microglia and to examine whether these were sufficient to drive HD-like pathology.

6.1 Transcriptomic changes in microglia in HD mouse models

mRNA sequencing was performed on microglia from 10-week-old R6/2 mice to reveal the specific transcriptional changes that these cells undergo when mHTT is expressed ubiquitously. Until now, the transcriptional profile of purified microglia from R6/2 mice had only been examined by looking at individual candidate genes by qPCR (Crotti et al., 2014) or by extrapolating microglia-specific changes in gene expression from whole-tissue homogenate analyses (Crapser et al., 2019).

Microglia-specific gene enrichment and the absence of expression of genes from possible contaminating populations proved that sorted population was highly pure for microglia from adult symptomatic R6/2 brains (**Fig. 3 and 4a**). We detected a number of cellular processes that were affected in microglia from R6/2 mice, including an interferon type I signature that was particularly interesting (**Fig. 4b**). Type I interferons (IFNs) are major effector cytokines of the host immune response against foreign (e.g. viral) or self-derived nucleic acids. IFNs are secreted upon activation by various pattern-recognition receptors and they act on type I receptors (IFNAR1/2) to induce the transcription of over 300 genes called IFN-stimulated genes (ISGs) through the Janus kinase (JAK)/signal transducers and activators of the transcription (STAT) pathway (Schneider et al., 2014). Increased IFN signalling can lead to apoptosis and necroptosis and, in order to prevent this, cells produce negative feedback players such as ISG15 or USP18 (both upregulated in R6/2 microglia; **Table 2**) that are recruited for long-term desensitization to type I IFN signaling (Schneider et al., 2014).

Any mHTT-induced burden of nucleic acids, enhanced receptor sensing or loss of function of the feedback system could trigger the sterile inflammation via up-regulated IFN-I signalling seen in R6/2 microglia. Our data did not indicate changes in the production of interferons themselves (e.g. *Ifna1, Ifnb1*). However, various downstream signaling molecules were affected. For example, the

gene encoding the IFNα receptor 1 subunit - *Ifnar1* was downregulated (**Fig. 4b** and **Table 2**). In addition, expression levels of the gene encoding for the downstream signal STAT1 increased in R6/2 microglia, as did a number of ISGs (e.g. *Mx1*, *Irf7*, *Oas2*, *Oasl2*, *Ifit1*, *Ifit2*, *Ifit3;* **Fig. 4b** and **Table 2**). It is not possible to determine the mechanism of induction nor the consequences of this IFN-I signature from RNA sequencing data alone. However, in recent years, such a type I interferon signature has been described in a growing number of non-viral neurological disorders (Blank and Prinz, 2017) and has recently been shown to contribute to neurodegeneration in a model of prion disease (Nazmi et al., 2019). It would therefore be interesting to examine this in the context of HD in the future.

Another interesting finding from RNA sequencing of R6/2 microglia is related to the findings of Crotti et al. (2014) who reported a cell-autonomous pro-inflammatory transcriptional activation of microglia in various models that was dependent on the increased transcriptional activities of the myeloid-lineage determining factors PU.1 and C/EBPs. We found that microglia isolated from 10-week-old R6/2 mice upregulated genes encoding for these myeloid-lineage determining factors, namely *Cebpa, Cebpb* and *Spi1*. However, we did not detect significant changes in gene expression of downstream pro-inflammatory cytokines such as *Il6, Il1b, Ifng*. This discrepancy might be due to the different methodology used (qPCR vs. RNAseq) or the different age of the mice used for microglia isolation (p0 pups vs. 10-week-old R6/2 mice in our paradigm). In line with our findings, microglia isolated from 18-20-month-old $Hdh^{175/175}$ knock-in mice that ubiquitously express mHTT with a 175 CAG expansion and lack wild-type HTT (Crotti et al., 2014) showed increased gene expression of *Cebpa*, *Cebpb* and *Spi1* when compared to controls, but no changes of *Irf1*, *Tlr2*, *Il6* and *Il1b* mRNA expression. Finally, results similar to ours were recently published by Crapser *et al.* (2019) who performed RNA sequencing on striatum-homogenates from 11-week-old R6/2 mice and showed a strong IFN-signature, but no changes in cytokine transcript levels.

We additionally examined the gene expression profiles of MG-HD mice, to test the cell-autonomous effect of mHTT expression on the microglia tascriptome. The lack of significant transcriptomic changes in microglia isolated of 12-month-old MG-HD mice compared to controls (**Fig. 11**) may be due to the lower expression levels of mHTT in microglia from MG-HD mice compared to R6/2 mice, differences in CAG repeat length between the two models, and non-cell-autonomous effects in R6/2 mice with ubiquitous mHTT expression.

6.2 Microglia depletion in symptomatic R6/2 mice does not rescue the disease phenotype

To answer the question of whether the microglial response in HD mouse models is beneficial or detrimental to symptom progression, the CSF1R kinase inhibitor BLZ945 was administered to deplete microglia in symptomatic (8-week-old) R6/2 mice. A significant reduction of cortical and striatal microglia was measured 2 days after termination of the 12-day BLZ945 treatment protocol in both R6/2 mice and their non-transgenic littermates when compared to mice that received vehicle alone. Depletion levels in the cortex and striatum were similar to those observed in a previous study that used the same administration protocol for 7 consecutive days and analysed microglia densities in the cerebellum and the corpus callosum (Hagemeyer et al., 2017). We observed no improvement in a series of behavioural tests and weight monitoring that were used in previous studies as primary outcome measures for HD neuropathology (e.g. Paldino et al., 2019, Petkau et al., 2019 and Siew et al., 2019; **Fig. 6**).

It is possible that treatment at different time-points, e.g. before symptom onset, might have generated different results. A study was recently published in which an alternative FDA-approved CSF-1R kinase inhibitor was administered to R6/2 mice (PLX5622) starting at 6 weeks of age, before the occurrence of obvious symptomatology (Crapser et al., 2019). This study reiterated our results to some extent by showing that PLX5622 did not improve weight loss or the RotaRod performance of R6/2 mice. However, it also showed that microglial elimination mitigated disease-related grip strength and object recognition deficits, mHTT accumulation, astrogliosis and striatal volume loss, which are parameters that we did not test for. In the past, pharmacological interventions using agents that prevent microglial activation have given mixed results regarding HD-like pathology (Chen et al., 2000, Smith et al., 2003, Paldino et al., 2019 and Siew et al., 2019).

6.3 Selective expression of mHTT in microglia in vivo causes mild cellular changes that do not drive HD-like neuropathology

6.3.1 The MG-HD mouse model

In this thesis, I established a mouse model with conditional expression of mHTT in microglia to examine which effects of mHTT expression are cell-autonomous to microglia and whether they are sufficient to drive HD-like pathology.

In the so-called MG-HD mice, mHTT expression was specific to microglia and was not detected in peripheral myeloid cells (**Fig. 7c**), which is crucial since parabiosis experiments have indicated that circulating factors can drive ageing and influence cognitive and neural functions in mice (Villeda et al., 2014, Katsimpardi et al., 2014 and Smith et al., 2015). In the context of HD, intravenously administered mHTT fibrils are capable inducing an immune response (Masnata et al., 2019) and mHTT fragment levels in monocytes were significantly associated with disease burden score and caudate atrophy rates in HD patients (Weiss et al., 2012). In the MG-HD model, where mHTT is not peripherally expressed, the exclusive effects of mHTT in microglia can be examined independently. However, it should be noted that partial tamoxifen-independent Cre activity has also been demonstrated in this Cx3cr1$^{tm2.1(cre/ERT2)Jung}$/J (Zhao et al., 2019; Stifter et al., 2020).

mHTT expression in the MG-HD model was stable over time (**Fig. 7b and 7d**). However, expression levels of mHTT were markedly lower in MG-HD microglia compared to microglia isolated from R6/2 mice. It is unlikely that the lower expression levels are a result of inefficient recombination since in *Cx3Cre^{CreER}:R26-yfp* reporter mice the same induction protocol resulted in recombination efficiency of 80-90% and remained stable over time (Goldmann et al., 2013 and repeated independently in our lab). A possible explanation for the lower levels of expression of mHTT in microglia from MG-HD mice compared to those of R6/2 mice could be that the promoters involved in driving mHTT expression are different in the two lines. In the R6/2 mouse, mHTT expression is driven by the human IT15 promoter while in the MG-HD model, mHTT is transcribed from the endogenous Rosa26 locus, which is a weaker driver in microglia (Fonseca et al., 2017). From the many different mouse models of HD, it is still not clear which model recapitulates the human condition more closely.

6.3.2 mHTT expression in microglia does not trigger infiltration of peripheral immune cells into the brain

The blood-brain-barrier (BBB) is a semi-permeable border that prevents solutes and cells from peripheral blood from entering the CNS. Defective BBB and neurovascular disintegration are associated with various neurodegenerative diseases and may facilitate the access of peripheral cells to the CNS (Zlokovic, 2011). In R6/2 mice and in HD patients, there is evidence of ultrastructural, morphological and functional changes in cerebral blood vessels with alterations of the BBB (Sciacca and Cicchetti, 2017 and Drouin-Ouellet et al., 2015). However, no evidence of infiltration

of circulating innate or adaptive immune cells has been documented in post-mortem HD brain samples to date (Silvestroni et al., 2009, Drouin-Ouellet et al., 2015). In line with this, we did not detect any changes in the number of $CD45^{hi}$ cells in 12-month-old MG-HD mice compared to controls, nor in the immune cell composition in the brains of R6/2 and MG-HD mice (**Fig. 8**).

6.3.3 Microglia in the MG-HD mouse model exhibit a mild phenotype

The presence of morphologically distinct microglia, often observed in increased numbers and in combination with activated astrocytes that upregulate GFAP is a conspicuous feature of diverse CNS pathologies (for review: Perry, 2010 and Ransohoff, 2016). An altered morphological phenotype of microglia was observed by histology in MG-HD mice (**Fig. 9a-c**), which was most prominent in the striatum than in other investigated brain regions and was coupled to increased GFAP immunoreactivity at 12 months of age (**Fig. 12**). The observed increase in microglia density and coverage is in line with post-mortem data from HD brains that showed early and progressive accumulation of reactive microglia in the cortex and the striatum (Sapp et al., 2001). We observed region-specific changes in MG-HD mice with exclusion of less affected brain areas like the cerebellum (**Fig. 9-10**), suggesting that microglia do indeed respond to endogenous mHTT expression. The fact that a measurable transcriptional phenotype was not seen in the RNA sequencing data from MG-HD mice could be due to pooling of microglia from all brain regions which could mask mild, region-specific effects. Regional heterogeneity of microglia has previously been shown in the YAC128 mouse model of HD, where microglia isolated from different brain regions responded differently to IFNγ stimulation despite expressing similar levels of mHTT (Connolly et al., 2016). In the future, single-cell RNA sequencing might help to shed light on transcriptional changes caused by mHTT expression in individual microglia.

Microglia-driven astrocytic changes have previously been described (Liddelow et al., 2017) and this was also seen in our MG-HD mice. A possible mechanism for this effect could be the trans-cellular propagation of the mHTT protein from microglia to surrounding cells in either a prion-like fashion (Pecho-Vrieseling et al., 2014, Jeon et al., 2016 and Masnata et al., 2019) or through cellular mechanisms such as exosome release or the late endosomal/lysosomal unconventional secretory pathway (Trajkovic et al., 2017). Trans-cellular propagation of the mHTT protein could also explain the downregulation of *Drd1a*, *Nr4a1*, *Drd2* and *Bdnf* that we measured by qPCR on whole brain lysates from MG-HD mice (**Fig. 13g**). Another mechanism that could explain the secondary effect on astrocytes could be a release of proinflammatory molecules like IL-1 or TNF

produced by mHTT-expressing microglia, although this was not evident on a transcriptional level in MG-HD mice (**Fig. 11**). Interestingly, a discrepancy between cytokine secretion and cytokine transcription has previously been demonstrated in microglia isolated from the YAC128 mouse model of HD (Connolly et al., 2016). This study showed that microglia isolated from YAC128 mice secreted elevated levels of pro-inflammatory molecules such as IL-12, IL-10, IL-1β, IL-2 and KC in response to IFNγ and/or control standard endotoxin stimulation even though the transcription of these cytokines remained unchanged. Therefore, it could be the case that mHTT expression in microglia alters cytokine secretion rather than cytokine transcription and that the observed increased GFAP immunoreactivity in the MG-HD brain is a response to increased cytokine secretion from microglia.

$P2Y_{12}$ receptor expression is part of a microglia-specific gene signature and is absent from other peripheral macrophages (Butovsky et al., 2014). Decreased $P2Y_{12}$ receptor immunoreactivity was observed in plaque-associated myeloid cells of patients with Alzheimer's disease and in lesion-associated myeloid cells of patients with multiple sclerosis (Mildner et al., 2017a). It is not entirely clear whether the absence of $P2Y_{12}$ receptor in these cells resulted from receptor downregulation or internalization as microglia became activated or whether the cells with lower levels of $P2Y_{12}$ receptor were infiltrating blood-borne cells that lack $P2Y_{12}$ receptor expression. Since we observed no evidence of myeloid cell infiltration into the brains of MG-HD mice (**Fig. 8**), the decrease of $P2Y_{12}$ receptor immunoreactivity in microglia likely reflects the direct effect of mHTT in these cells (**Fig. 10**).

mHTT nuclear inclusions occur to different extents in different cell types (Jansen et al., 2017). It is interesting that microglia are the least sensitive to mHTT accumulation among brain cell types (only 0-2% occurrence across mouse models and patients), while neurons are the most vulnerable (Jansen et al., 2017). This could be due to the enhanced ability of microglia to proliferate compared to other brain cells (Askew et al., 2017), resulting in a reduced mHTT load in their progeny due to asymmetric inheritance of the accumulated protein (Rujano et al., 2006). We observed an increase in microglia density at 12 months of age in the MG-HD mice (**Fig. 9a-c**), although the $Iba1^+$ $Ki67^+$ proportion of microglia was not significantly increased. It is still likely that increased microglia proliferation does actually occur over time, which was not captured by measuring Ki67 immunoreactivity that only examines a very narrow time-window of proliferation. It is also possible that the decreased incidence of mHTT nuclear inclusions in microglia is due to the ability of microglia to clear aberrant proteins more effectively than other brain cells. This has been

demonstrated in the context of other proteinopathies such as Alzheimer's disease (Orre et al., 2013 and Su et al., 2016).

When comparing the brains of MG-HD mice at 12 months and 22 months of age, the genotype-specific effects of mHTT expression in microglia and the secondary effects it had on astrocytes were diluted (**Fig. 10, 12 and 17, 18**). It therefore seems that effects caused by mHTT in microglia at 12 months were masked by the gradual changes of microglia that occur with ageing (Silvin and Ginhoux, 2018). Taken together, our observations of mHTT-induced microglia changes MG-HD mice highlight the known heterogeneity of microglia in space and time. In whole, we demonstrated that any changes caused cell-autonomously by mHTT expression in microglia are mild and transient compared to the non-cell autonomous changes observed in models that ubiquitously express the mutant protein.

6.3.4 Targeted expression of mHTT to microglia in vivo does not drive HD-like behavioural or neuropathological deficits

Perhaps the most important finding of my study is that the selective expression of mHTT in microglia in the MG-HD model does not lead to HD-like neuropathology up to 22 months of age. In contrast to studies that targeted mHTT expression to astrocytes or oligodendrocytes (Bradford, 2009; Huang et al., 2015), we observed no evidence of neuronal pathology, brain atrophy, weight or behavioural changes that are characteristic of HD mouse models. It is important to note that the mouse models of HD used in the two aforementioned articles varied from ours in terms of the size of the repeat expansion, whether mHTT was full-length or N-terminal and in terms of the promoters that were used to drive the expression. The variability of HD mouse models is a general problem in HD research, which makes findings difficult to compare against each other.

We observed no evidence of striatal atrophy by MRI (**Section 5.8.3**) nor did we observe striatal neuron (Darpp32^{+}) cell loss (**Fig. 13 and 17**). The amount of PSD-95^{+} synapses and D2R protein expression also remained stable in 12 and 22-month old microglia HD mice (**Fig. 13 and 17**). Finally, mHTT targeted expression in microglia had no effect on the weight or motor and cognitive abilities of male (**Fig. 14**), female (**Fig. 15**) or aged MG-HD mice (**Fig. 17**). In a similar paradigm to ours, 8-week-old *Cx3cr1*^{Cre} *x Rosa-mHTT* mice only showed an increased number of Fluoro-Jade B^{+} degenerated/dead neurons compared to non-transgenic controls when intrastriatally injected with LPS (Crotti et al., 2014). These mice are identical to MG-HD mice, except that they constitutively expressed mHTT, meaning that mHTT expression extended to peripheral *Cx3cr1*-

expressing myeloid cells and also to neurons during development (https://www.jax.org/strain/025524). Based on these and my own data, we can conclude that with ageing and in the absence of secondary stimuli such as LPS-induced sterile inflammation or mHTT induced changes from peripheral myeloid cells and developing neurons, mHTT expression in microglia is not sufficient to induce HD-like neuropathology.

In another recent study, the BACHD mouse model of HD was used either to selectively deplete mHTT expression in myeloid lineage cells (including microglia) or to selectively deplete mHTT expression in the majority of cells in the brain but specifically excluding microglia (Petkau et al., 2019). By subsequent evaluation of HD-related behaviour and neuropathology, they showed that mice with myeloid-specific mHTT-deletion displayed no significant rescue of any behavioural or neuropathological deficits, while neural-specific knockout mice showed significant rescue of weight loss, RotaRod performance and striatal volume reduction. This study, that nicely complements ours, concludes that mHTT expression in microglia, though clearly affecting specific aspects of microglia function, does not alter disease pathogenesis in the BACHD mouse model that expresses the full-length human protein as opposed to just mHTT-exon1.

One drawback of the MG-HD model is that, although mHTT expression is targeted to microglia with great specificity, its expression is only induced at 5-7 weeks of age and, therefore, the potentially critical phase of development is not considered. In a recent study in which ubiquitous mHTT expression was stopped at post-natal day 21, mice displayed similar profiles of impairment to those that expressed mHTT throughout their life (Molero et al., 2016). Developmental aberrations that are unaccounted for in our model might also play an important role mHTT-induced changes in microglia, although, the study that selectively and constitutively depleted mHTT in all myeloid cells in the BACHD mouse suggest that this might not be important when it comes to microglia (Petkau et al., 2019).

In conclusion, this work has provided evidence that microglial dysfunction due to mHTT expression is not sufficient to drive the core HD-like phenotypes observed in mouse models of HD.

References

Aguzzi A, Barres BA, Bennett ML (2013) Microglia: scapegoat, saboteur, or something else. Science, 339:156–161.

Ajami B, Bennet JL, Krieger C, Tetzlaff W, Rossi FMV (2007) Local self-renewal can sustain CNS microglia maintenance and function throughout adult life. Nat Neurosci, 10:1538-1543.

Alexa A, Rahnenführer J, Lengauer T (2006) Improved scoring of functional groups from gene expression data by decorrelating GO graph structure. Bioinformatics, 22:1600–1607.

Arrasate M, Finkbeiner S (2012) Protein aggregates in Huntington's disease. Exp Neurol, 238:1–11.

Ashburner J, Friston KJ (2005) Unified segmentation. Neuroimage, 26:839–851.

Askew K, Li K, Olmos-Alonso A, Garcia-Moreno F, Liang Y, Richardson P, Tipton T, Chapman MA, Riecken K, Beccari S, Sierra A, Molnár Z, Cragg MS, Garaschuk O, Perry VH, Gomez-Nicola D (2017) Coupled Proliferation and Apoptosis Maintain the Rapid Turnover of Microglia in the Adult Brain. Cell Rep, 18:391–405.

Ayata P, Badimon A, Strasburger HJ, Duff MK, Montgomery SE, Loh YE, Ebert A, Pimenova AA, Ramirez BR, Chan AT, Sullivan JM, Purushothaman I, Scarpa JR, Goate AM, Busslinger M, Shen L, Losic B, Schaefer A (2018) Epigenetic regulation of brain region-specific microglia clearance activity. Nat Neurosci 21:1049-1060.

Barnat M, Capizzi M, Aparicio E, Boluda S, Wennagel D, Kacher R, Kassem R, Lenoir S, Agasse F, Braz BY, Liu JP, Ighil J, Tessier A, Zeitlin SO, Duyckaerts C, Dommergues M, Durr A, Humbert S (2020) Huntington's disease alters human neurodevelopment. Science 369:787-793.

Baquet ZC, Gorski JA, Jones KR (2004) Early striatal dendrite deficits followed by neuron loss with advanced age in the absence of anterograde cortical brain-derived neurotrophic factor. J Neurosci, 24:4250–4258.

Barbaro BA, Lukacsovich T, Agrawal N, Burke J, Bornemann DJ, Purcell JM, Worthge SA, Caricasole A, Weiss A, Song W, Morozova OA, Colby DW, Marsh JL (2015) Comparative study of naturally occurring huntingtin fragments in Drosophila points to exon 1 as the most pathogenic species in Huntington's disease. Hum Mol Genet, 24:913–925.

Bates GP, Dorsey R, Gusella JF, Hayden MR, Kay C, Leavitt BR, Nance M, Ross CA, Scahill RI, Wetzel R, Wild EJ, Tabrizi SJ (2015) Huntington disease. Nature Reviews Disease Primers, 1:1-21.

Bennett EJ, Shaler TA, Woodman B, Ryu KY, Zaitseva TS, Becker CH, Bates GP, Schulman H, Kopito RR (2007) Global changes to the ubiquitin system in Huntington's disease. Nature, 448:704–708.

Björkqvist M, Wild EJ, Thiele J, Silvestroni A, Andre R, Lahiri N, Raibon E, Lee RV, Benn CL, Soulet D, Magnusson A, Woodman B, Landles C, Pouladi MA, Hayden MR, Khalili-Shirazi A, Lowdell MW, Brundin P, Bates GP, Leavitt BR, Möller T, Tabrizi SJ (2008) A novel pathogenic pathway of immune activation detectable before clinical onset in Huntington's disease. J Exp Med, 205:1869–1877.

Blank T, Prinz M (2017) Type I interferon pathway in CNS homeostasis and neurological disorders. Glia, 65:1397–1406.

Böttcher C, Schlickeise S, Sneeboer MAM, Kunkel D, Knop A, Paza E, Fidzinski P, Kraus L, Snijders GJL, Kahn RS, Schulz AR, Mei HE, NBB-Psy, Hol EM, Siegmund B, Glauben R, Spruth E, de Witte LD, Priller J (2019) Human microglia regional heterogeneity and phenotypes determined by multiplexed single -cell mass cytometry. Nat Neurosci 22:78-90.

Bradford J, Shin JY, Roberts M, Wang CE, Li XJ, Li S (2009) Expression of mutant huntingtin in mouse brain astrocytes causes age-dependent neurological symptoms. Proc Natl Acad Sci USA, 106:22480–22485.

Browne SE, Bowling AC, MacGarvey U, Baik MJ, Berger SC, Muqit MM, Bird ED, Beal MF (1997) Oxidative damage and metabolic dysfunction in Huntington's disease: selective vulnerability of the basal ganglia. Ann Neurol, 41:646–653.

Butler R, Bates GP (2006) Histone deacetylase inhibitors as therapeutics for polyglutamine disorders. Nat Rev Neurosci, 7:784–796.

Butovsky O, Jedrychowski MP, Moore CS, Cialic R, Lanser AJ, Gabriely G, Koeglsperger T, Dake B, Wu PM, Doykan CE, Fanek Z, Liu L, Chen Z, Rothstein JD, Ransohoff RM, Gygi SP, Antel JP, Weiner HL (2014) Identification of a unique TGF-β-dependent molecular and functional signature in microglia. Nat Neurosci, 17:131–143.

Cepeda C, Murphy KP, Parent M, Levine MS (2014) The role of dopamine in Huntington's disease. Prog Brain Res, 211:235–254.

Chen M, Ona VO, Li M, Ferrante RJ, Fink KB, Zhu S, Bian J, Guo L, Farrell LA, Hersch SM, Hobbs W, Vonsattel JP, Cha JH, Friedlander RM (2000) Minocycline inhibits caspase-1 and caspase-3 expression and delays mortality in a transgenic mouse model of Huntington disease. Nat Med, 6:797–801.

Connolly C, Magnusson-Lind A, Lu G, Wagner PK, Southwell AL, Hayden MR, Björkqvist M, Leavitt BR (2016) Enhanced immune response to MMP3 stimulation in microglia expressing mutant huntingtin. Neuroscience, 325:74–88.

Cowin RM, Bui N, Graham D, Green JR, Grueninger S, Yuva-Paylor LA, Syed AU, Weiss A, Paylor R (2011) Onset and progression of behavioral and molecular phenotypes in a novel congenic R6/2 line exhibiting intergenerational CAG repeat stability. PLoS One, 6:e28409.

Crapser JD, Ochaba J, Soni N, Reidling JC, Thompson LM, Green KN (2019) Microglial depletion prevents extracellular matrix changes and striatal volume reduction in a model of Huntington's disease. Brain, 0:1-23

Creus-Muncunill J, Ehrlich ME (2019) Cell-Autonomous and Non-cell-Autonomous Pathogenic Mechanisms in Huntington's Disease: Insights from In Vitro and In Vivo Models. Neurotherapeutics, 16:957-978.

Crotti A, Benner C, Kerman BE, Gosselin D, Lagier-Tourenne C, Zuccato C, Cattaneo E, Gage FH, Cleveland DW, Glass CK (2014) Mutant Huntingtin promotes autonomous microglia activation via myeloid lineage-determining factors. Nat Neurosci, 17:513–521.

Davalos D, Grutzendler J, Yang G, Kim JV, Zuo Y, Jung S, Littman DR, Dustin ML, Gan WB (2005) ATP mediates rapid microglial response to local brain injury in vivo. Nat Neurosci, 8:752–758.

Davies SW, Turmaine M, Cozens BA, DiFiglia M, Sharp AH, Ross CA, Scherzinger E, Wanker EE, Mangiarini L, Bates GP (1997) Formation of neuronal intranuclear inclusions underlies the neurological dysfunction in mice transgenic for the HD mutation. Cell, 90:537–548.

Díaz-Hernández M, Díez-Zaera M, Sánchez-Nogueiro J, Gómez-Villafuertes R, Canals JM, Alberch J, Miras-Portugal MT, Lucas JJ (2009) Altered P2X7-receptor level and function in mouse models of Huntington's disease and therapeutic efficacy of antagonist administration. The FASEB Journal, 23:1893–1906.

Dietrich P, Shanmugasundaram R, Shuyu E, Dragatsis I (2009) Congenital hydrocephalus associated with abnormal subcommissural organ in mice lacking huntingtin in Wnt1 cell lineages. Hum Mol Genet, 18:142–150.

DiFiglia M, Sapp E, Chase KO, Davies SW, Bates GP, Vonsattel JP, Aronin N (1997) Aggregation of Huntingtin in Neuronal Intranuclear Inclusions and Dystrophic Neurites in Brain. Science, 277:1990–1993.

Dobin A, Davis CA, Schlesinger F, Drenkow J, Zaleski C, Jha S, Batut P, Chaisson M, Gingeras TR (2013) STAR: ultrafast universal RNA-seq aligner. Bioinformatics, 29:15–21.

Donley D, Nelson R, Gigley J, Fox J (2019) Mutant huntingtin protein alters the response of microglial cells to inflammatory stimuli. bioRxiv [Preprint]

Dragatsis I, Levine MS, Zeitlin S (2000) Inactivation of Hdh in the brain and testis results in progressive neurodegeneration and sterility in mice. Nat Genet, 26:300–306.

Drouin-Ouellet J, Sawiak SJ, Cisbani G, Lagacé M, Kuan WL, Saint-Pierre M, Dury RJ, Alata W, St-Amour I, Mason SL, Calon F, Lacroix S, Gowland PA, Francis ST, Barker RA, Cicchetti F (2015) Cerebrovascular and blood-brain barrier impairments in Huntington's disease: Potential implications for its pathophysiology. Ann Neurol, 78:160–177.

Duyao M, Auerbach A, Ryan A, Persichetti F, Barnes G, McNeil S, Ge P, Vonsattel J, Gusella J, Joyner A, et A (1995) Inactivation of the mouse Huntington's disease gene homolog Hdh. Science, 269:407–410.

Faideau M, Kim J, Cormier K, Gilmore R, Welch M, Auregan G, Dufour N, Guillermier M, Brouillet E, Hantraye P, Déglon N, Ferrante RJ, Bonvento G (2010) In vivo expression of polyglutamine-expanded huntingtin by mouse striatal astrocytes impairs glutamate transport: a correlation with Huntington's disease subjects. Hum Mol Genet, 19:3053–3067.

Fonseca MI, Chu SH, Hernandez MX, Fang MJ, Modarresi L, Selvan P, MacGregor GR, Tenner AJ (2017) Cell-specific deletion of C1qa identifies microglia as the dominant source of C1q in mouse brain. J Neuroinflammation, 14:48.

Franciosi S, Ryu JK, Shim Y, Hill A, Connolly C, Hayden MR, McLarnon JG, Leavitt BR (2012) Age-dependent neurovascular abnormalities and altered microglial morphology in the YAC128 mouse model of Huntington disease. Neurobiol Dis, 45:438–449.

Friedman JH, Trieschmann ME, Myers RH, Fernandez HH (2005) Monozygotic twins discordant for Huntington disease after 7 years. Arch Neurol, 62:995–997.

Frost JL, Schafer DP (2016) Microglia: Architects of the Developing Nervous System. Trends Cell Biol, 26:587–597.

Gauthier LR, Charrin BC, Borrell-Pagès M, Dompierre JP, Rangone H, Cordelières FP, De Mey J, MacDonald ME, Lessmann V, Humbert S, Saudou F (2004) Huntingtin controls neurotrophic support and survival of neurons by enhancing BDNF vesicular transport along microtubules. Cell, 118:127–138.

Georgiou N, Bradshaw JL, Chiu E, Tudor A, O'Gorman L, Phillips JG (1999) Differential clinical and motor control function in a pair of monozygotic twins with Huntington's disease. Mov Disord, 14:320–325.

Ghosh R, Tabrizi SJ (2018) Clinical Features of Huntington's Disease. In: Polyglutamine Disorders: Advances in Experimental Medicine and Biology eds, pp 1–28. Cham: Springer International Publishing.

Ginhoux F, Greter M, Leboeuf M, Nandi S, See P, Gokhan S, Mehler MF, Conway SJ, Ng LG, Stanley ER, Samokhvalov IM, Merad M (2010) Fate mapping analysis reveals that adult microglia derive from primitive macrophages. Science, 330:841–845.

Giorgini F, Möller T, Kwan W, Zwilling D, Wacker JL, Hong S, Tsai LC, Cheah CS, Schwarcz R, Guidetti P, Muchowski PJ (2008) Histone deacetylase inhibition modulates kynurenine pathway activation in yeast, microglia, and mice expressing a mutant huntingtin fragment. J Biol Chem, 283:7390–7400.

Goldmann T, Wieghofer P, Müller PF, Wolf Y, Varol D, Yona S, Brendecke SM, Kierdorf K, Staszewski O, Datta M, Luedde T, Heikenwalder M, Jung S, Prinz M (2013) A new type of microglia gene targeting shows TAK1 to be pivotal in CNS autoimmune inflammation. Nature Neuroscience, 16:1618–1626.

Gómez-Esteban JC, Lezcano E, Zarranz JJ, Velasco F, Garamendi I, Pérez T, Tijero B (2007) Monozygotic twins suffering from Huntington's disease show different cognitive and behavioural symptoms. Eur Neurol, 57:26–30.

Grabert K, Michoel T, Karavolos MH, Clohisey S, Baillie JK, Stevens MP, Freeman TC, Summers KM, McColl BQ (2016) Microglial brain region-dependent diversity and selective regional sensitivities to aging. Net Neurosci 19:504-516.

Gray M (2019) Astrocytes in Huntington's Disease. Adv Exp Med Biol, 1175:355–381.

Gu X, André VM, Cepeda C, Li S-H, Li X-J, Levine MS, Yang XW (2007) Pathological cell-cell interactions are necessary for striatal pathogenesis in a conditional mouse model of Huntington's disease. Molecular Neurodegeneration, 2:8.

Gu X, Li C, Wei W, Lo V, Gong S, Li SH, Iwasato T, Itohara S, Li XJ, Mody I, Heintz N, Yang XW (2005) Pathological cell-cell interactions elicited by a neuropathogenic form of mutant Huntingtin contribute to cortical pathogenesis in HD mice. Neuron, 46:433–444.

Gutekunst CA, Levey AI, Heilman, CJ, Whaley WL, Yi H, Nash NR, Rees HD, Madden JJ, Mersch SM (1995) Identification of huntingtin in the brain and human lymphoblastoid cell lines with anti-fusion protein antibodies. Proc Natl Acad Sci USA, 92:8710-8714.

Hagemeyer N, Hanft K-M, Akriditou M-A, Unger N, Park ES, Stanley ER, Staszewski O, Dimou L, Prinz M (2017) Microglia contribute to normal myelinogenesis and to oligodendrocyte progenitor maintenance during adulthood. Acta Neuropathologica, 134:441–458.

Heinz S, Benner C, Spann N, Bertolino E, Lin YC, Laslo P, Cheng JX, Murre C, Singh H, Glass CK (2010) Simple combinations of lineage-determining transcription factors prime cis-regulatory elements required for macrophage and B cell identities. Mol Cell, 38:576–589.

Huang B, Wei W, Wang G, Gaertig MA, Feng Y, Wang W, Li XJ, Li S (2015) Mutant huntingtin downregulates myelin regulatory factor-mediated myelin gene expression and affects mature oligodendrocytes. Neuron, 85:1212–1226.

Huntington G (1872) On Chorea. The Medical and Surgical Reporter: A Weekly Journal, 26:317–321.

Huntington Study Group COHORT Investigators, Dorsey E (2012) Characterization of a large group of individuals with huntington disease and their relatives enrolled in the COHORT study. PLoS One, 7:e29522.

Jaitin DA, Kenigsberg E, Keren-Shaul H, Elefant N, Paul F, Zaretsky I, Mildner A, Cohen N, Jung S, Tanay A, Amit I (2014) Massively parallel single-cell RNA-seq for marker-free decomposition of tissues into cell types. Science, 343:776–779.

Jansen AHP, van Hal M, op den Kelder IC, Meier RT, de Ruiter A-A, Schut MH, Smith DL, Grit C, Brouwer N, Kamphuis W, Boddeke HWGM, den Dunnen WFA, van Roon WMC, Bates GP, Hol EM, Reits EA (2017) Frequency of nuclear mutant huntingtin inclusion formation in neurons and glia is cell-type-specific. Glia, 65:50–61.

Jeon I, Cicchetti F, Cisbani G, Lee S, Li E, Bae J, Lee N, Li L, Im W, Kim M, Kim HS, Oh SH, Kim TA, Ko JJ, Aubé B, Oueslati A, Kim YJ, Song J (2016) Human-to-mouse prion-like propagation of mutant huntingtin protein. Acta Neuropathol, 132:577–592.

Jin YN, Johnson GV (2010) The interrelationship between mitochondrial dysfunction and transcriptional dysregulation in Huntington disease. J Bioenerg Biomembr, 42:199–205.

Katsimpardi L, Litterman NK, Schein PA, Miller CM, Loffredo FS, Wojtkiewicz GR, Chen JW, Lee RT, Wagers AJ, Rubin LL (2014) Vascular and neurogenic rejuvenation of the aging mouse brain by young systemic factors. Science, 344:630–634.

Kay C, Hayden MR, Leavitt BR (2017) Epidemiology of Huntington disease. Handb Clin Neurol, 144:31–46.

Kayson E, Eberly S, Anderson KE, Marder K, Shoulson I, Oakes D, Young AB, Biglan K, Hersch S, Huntington SGPHAROSI (2019) The Prospective Huntington At-Risk Observational Study (PHAROS): The Emotional Well-Being, Safety and Feasibility of Long-Term Research Participation. J Huntingtons Dis, 8:435–441.

Kettenmann H, Kirchhoff F, Verkhratsky A (2013) Microglia: new roles for the synaptic stripper. Neuron, 77:10–18.

Khoshnan A, Patterson PH (2011) The role of IκB kinase complex in the neurobiology of Huntington's disease. Neurobiol Dis, 43:305–311.

Khoshnan A, Sabbaugh A, Calamini B, Marinero SA, Dunn DE, Yoo JH, Ko J, Lo DC, Patterson PH (2017) IKKβ and mutant huntingtin interactions regulate the expression of IL-34: implications for microglial-mediated neurodegeneration in HD. Hum Mol Genet, 26:4267–4277.

Kierdorf K, Erny D, Goldmann T, Sander V, Schulz C, Perdiguero EG, Wieghofer P, Heinrich A, Riemke P, Hölscher C, Müller DN, Luckow B, Brocker T, Debowski K, Fritz G, Opdenakker G, Diefenbach A, Biber K, Heikenwalder M, Geissmann F, Rosenbauer F, Prinz M (2013) Microglia emerge from erythromyeloid precursors via Pu.1- and Irf8-dependent pathways. Nat Neurosci, 16:273–280.

Kimmelman J, Mogil JS, Dirnagl U (2014) Distinguishing between exploratory and confirmatory preclinical research will improve translation. PLoS Biol, 12:e1001863.

Klein S, Staring M, Murphy K, Viergever MA, Pluim JP (2010) elastix: a toolbox for intensity-based medical image registration. IEEE Trans Med Imaging, 29:196–205.

Klöppel S, Gregory S, Scheller E, Minkova L, Razi A, Durr A, Roos RA, Leavitt BR, Papoutsi M, Landwehrmeyer GB, Reilmann R, Borowsky B, Johnson H, Mills JA, Owen G, Stout J, Scahill RI, Long JD, Rees G, Tabrizi SJ, the Track-On Investigators (2015) Compensation

in Preclinical Huntington's Disease: Evidence From the Track-On HD Study. EBioMedicine, 2:1420–1429.

Kraft AD, Kaltenbach LS, Lo DC, Harry GJ (2012) Activated microglia proliferate at neurites of mutant huntingtin-expressing neurons. Neurobiol Aging, 33:621.e17–33.

Kwan W, Träger U, Davalos D, Chou A, Bouchard J, Andre R, Miller A, Weiss A, Giorgini F, Cheah C, Möller T, Stella N, Akassoglou K, Tabrizi SJ, Muchowski PJ (2012) Mutant huntingtin impairs immune cell migration in Huntington disease. J Clin Invest, 122:4737–4747.

Labadorf A, Hoss AG, Lagomarsino V, Latourelle JC, Hadzi TC, Bregu J, MacDonald ME, Gusella JF, Chen JF, Akbarian S, Weng Z, Myers RH (2015) RNA Sequence Analysis of Human Huntington Disease Brain Reveals an Extensive Increase in Inflammatory and Developmental Gene Expression. PLoS One, 10:e0143563.

Lanska DJ (2000) George Huntington (1850-1916) and hereditary chorea. J Hist Neurosci, 9:76–89.

Lavin Y, Winter D, Blecher-Gonen R, David E, Keren-Shaul H, Merad M, Jung S, Amit I (2014) Tissue-resident macrophage enhancer landscapes are shaped by the local microenvironment. Cell, 159:1312–1326.

Lawson LJ, Perry VH, Dri P, Gordon S (1990) Heterogeneity in the distribution and morphology of microglia in the normal adult mouse brain. Neuroscience, 39:151–170.

Lawson LJ, Perry VH, Gordon S (1992) Turnover of resident microglia in the normal adult mouse brain. Neuroscience, 48:405–415.

Li H, Wyman T, Yu ZX, Li SH, Li XJ (2003) Abnormal association of mutant huntingtin with synaptic vesicles inhibits glutamate release. Hum Mol Genet, 12:2021–2030.

Liddelow SA, Guttenplan KA, Clarke LE, Bennett FC, Bohlen CJ, Schirmer L, Bennett ML, Münch AE, Chung W-S, Peterson TC, Wilton DK, Frouin A, Napier BA, Panicker N, Kumar M, Buckwalter MS, Rowitch DH, Dawson VL, Dawson TM, Stevens B, Barres BA (2017) Neurotoxic reactive astrocytes are induced by activated microglia. Nature, 541:481–487.

Liu JP, Zeitlin SO (2017) Is Huntingtin Dispensable in the Adult Brain. J Huntingtons Dis, 6:1–17.

Liu W, Pfister EL, Kennington LA, Chase KO, Mueller C, DiFiglia M, Aronin N (2016) Does the Mutant CAG Expansion in Huntingtin mRNA Interfere with Exonucleolytic Cleavage of its First Exon. Journal of Huntington's Disease, 5:33–38.

Love MI, Huber W, Anders S (2014) Moderated estimation of fold change and dispersion for RNA-seq data with DESeq2. Genome Biol, 15:550.

Mangiarini L, Sathasivam K, Seller M, Cozens B, Harper A, Hetherington C, Lawton M, Trottier Y, Lehrach H, Davies SW, Bates GP (1996) Exon 1 of the HD gene with an expanded CAG repeat is sufficient to cause a progressive neurological phenotype in transgenic mice. Cell, 87:493–506.

Martinez-Vicente M, Talloczy Z, Wong E, Tang G, Koga H, Kaushik S, de Vries R, Arias E, Harris S, Sulzer D, Cuervo AM (2010) Cargo recognition failure is responsible for inefficient autophagy in Huntington's disease. Nat Neurosci, 13:567–576.

Masnata M, Sciacca G, Maxan A, Bousset L, Denis HL, Lauruol F, David L, Saint-Pierre M, Kordower JH, Melki R, Alpaugh M, Cicchetti F (2019) Demonstration of prion-like

properties of mutant huntingtin fibrils in both in vitro and in vivo paradigms. Acta Neuropathol, 137:981–1001.

Masuda T, Sankowski R, Staszewski O, Böttcher C, Amann L, Sagar, Scheiwe C, Nessler S, Kunz P, van Loo G, Coenen VA, Reinacher PC, Michel A, Sure U, Gold R, Grün D, Priller J, Stadelmann C, Prinz M (2019) Spatial and temporal heterogeneity of mouse and human microglia at single-cell resolution. Nature, 566:388–392.

Matcovitch-Natan O, Winter DR, Giladi A, Vargas Aguilar S, Spinrad A, Sarrazin S, Ben-Yehuda H, David E, Zelada González F, Perrin P, Keren-Shaul H, Gury M, Lara-Astaiso D, Thaiss CA, Cohen M, Bahar Halpern K, Baruch K, Deczkowska A, Lorenzo-Vivas E, Itzkovitz S, Elinav E, Sieweke MH, Schwartz M, Amit I (2016) Microglia development follows a stepwise program to regulate brain homeostasis. Science, 353:aad8670.

McColgan P, Tabrizi SJ (2018) Huntington's disease: a clinical review. Eur J Neurol, 25:24–34.

Mildner A, Schmidt H, Nitsche M, Merkler D, Hanish UC, Mack M, Heikenwalder M, Brück W, Priller J, Prinz M (2007) Microglia in the adult brain arise from Ly-6C^{hi}CCR2^{+} monocytes only under defined host conditions. Nat Neurosci, 10:1544-1553.

Mildner A, Huang H, Radke J, Stenzel W, Priller J (2017a) P2Y12 receptor is expressed on human microglia under physiological conditions throughout development and is sensitive to neuroinflammatory diseases. Glia, 65:375–387.

Mildner A, Schönheit J, Giladi A, David E, Lara-Astiaso D, Lorenzo-Vivas E, Paul F, Chappell-Maor L, Priller J, Leutz A, Amit I, Jung S (2017b) Genomic Characterization of Murine Monocytes Reveals C/EBPβ Transcription Factor Dependence of Ly6C- Cells. Immunity, 46:849–862.e7.

Mittelbronn M, Dietz K, Schluesener HJ, Meyermann R (2001) Local distribution of microglia in the normal adult human central nervous system differs by up to one order of magnitude. Acta Neuropathol, 101:249–255.

Molero AE, Arteaga-Bracho EE, Chen CH, Gulinello M, Winchester ML, Pichamoorthy N, Gokhan S, Khodakhah K, Mehler MF (2016) Selective expression of mutant huntingtin during development recapitulates characteristic features of Huntington's disease. Proc Natl Acad Sci USA, 113:5736–5741.

Nasir J, Floresco SB, O'Kusky JR, Diewert VM, Richman JM, Zeisler J, Borowski A, Marth JD, Phillips AG, Hayden MR (1995) Targeted disruption of the Huntington's disease gene results in embryonic lethality and behavioral and morphological changes in heterozygotes. Cell, 81:811–823.

Nazmi A, Field RH, Griffin EW, Haugh O, Hennessy E, Cox D, Reis R, Tortorelli L, Murray CL, Lopez-Rodriguez AB, Jin L, Lavelle EC, Dunne A, Cunningham C (2019) Chronic neurodegeneration induces type I interferon synthesis via STING, shaping microglial phenotype and accelerating disease progression. Glia, 67:1254–1276.

Niccolini F, Politis M (2014) Neuroimaging in Huntington's disease. World J Radiol, 6:301–312.

Nimmerjahn A, Kirchhoff F, Helmchen F (2005) Resting microglial cells are highly dynamic surveillants of brain parenchyma in vivo. Science, 308:1314–1318.

Orr HT, Zoghbi HY (2007) Trinucleotide repeat disorders. Annu Rev Neurosci, 30:575–621.

Orre M, Kamphuis W, Dooves S, Kooijman L, Chan ET, Kirk CJ, Dimayuga Smith V, Koot S, Mamber C, Jansen AH, Ovaa H, Hol EM (2013) Reactive glia show increased immunoproteasome activity in Alzheimer's disease. Brain, 136:1415–1431.

Orth M, Handley OJ, Schwenke C, Dunnett SB, Craufurd D, Ho AK, Wild E, Tabrizi SJ, Landwehrmeyer GB, Investigators OTEHDN (2010) Observing Huntington's Disease: the European Huntington's Disease Network's REGISTRY. PLoS Curr, 2:RRN1184.

Pagan F, Torres-Yaghi Y, Altshuler M (2017) The diagnosis and natural history of Huntington disease. Handb Clin Neurol, 144:63–67.

Palazuelos J, Aguado T, Pazos MR, Julien B, Carrasco C, Resel E, Sagredo O, Benito C, Romero J, Azcoitia I, Fernández-Ruiz J, Guzmán M, Galve-Roperh I (2009) Microglial CB2 cannabinoid receptors are neuroprotective in Huntington's disease excitotoxicity. Brain, 132:3152–3164.

Paldino E, Balducci C, La Vitola P, Artioli L, D'Angelo V, Giampà C, Artuso V, Forloni G, Fusco FR (2019) Neuroprotective Effects of Doxycycline in the R6/2 Mouse Model of Huntington's Disease. Mol Neurobiol, 57:1889–1903.

Paolicelli RC, Bolasco G, Pagani F, Maggi L, Scianni M, Panzanelli P, Giustetto M, Ferreira TA, Guiducci E, Dumas L, Ragozzino D, Gross CT (2011) Synaptic pruning by microglia is necessary for normal brain development. Science, 333:1456–1458.

Pardo R, Molina-Calavita M, Poizat G, Keryer G, Humbert S, Saudou F (2010) pARIS-htt: an optimised expression platform to study huntingtin reveals functional domains required for vesicular trafficking. Mol Brain, 3:17.

Paulsen JS, Long JD, Ross CA, Harrington DL, Erwin CJ, Williams JK, Westervelt HJ, Johnson HJ, Aylward EH, Zhang Y, Bockholt HJ, Barker RA, PREDICT-HD IACOTHSG (2014) Prediction of manifest Huntington's disease with clinical and imaging measures: a prospective observational study. Lancet Neurol, 13:1193–1201.

Pavese N, Gerhard A, Tai YF, Ho AK, Turkheimer F, Barker RA, Brooks DJ, Piccini P (2006) Microglial activation correlates with severity in Huntington disease: a clinical and PET study. Neurology, 66:1638–1643.

Paxinos G, Franklin KBJ (2004) The Mouse Brain in Stereotaxic Coordinates. Gulf Professional Publishing.

Pecho-Vrieseling E, Rieker C, Fuchs S, Bleckmann D, Esposito MS, Botta P, Goldstein C, Bernhard M, Galimberti I, Müller M, Lüthi A, Arber S, Bouwmeester T, van der Putten H, Di Giorgio FP (2014) Transneuronal propagation of mutant huntingtin contributes to non–cell autonomous pathology in neurons. Nature Neuroscience, 17:1064–1072.

Perry VH (2010) Contribution of systemic inflammation to chronic neurodegeneration. Acta Neuropathol, 120:277–286.

Petkau TL, Hill A, Connolly C, Lu G, Wagner P, Kosior N, Blanco J, Leavitt BR (2019) Mutant huntingtin expression in microglia is neither required nor sufficient to cause the Huntington's disease-like phenotype in BACHD mice. Human Molecular Genetics, 28:1661–1670.

Pfaffl MW, Tichopad A, Prgomet C, Neuvians TP (2004) Determination of stable housekeeping genes, differentially regulated target genes and sample integrity: BestKeeper--Excel-based tool using pair-wise correlations. Biotechnol Lett, 26:509–515.

Politis M, Lahiri N, Niccolini F, Su P, Wu K, Giannetti P, Scahill RI, Turkheimer FE, Tabrizi SJ, Piccini P (2015) Increased central microglial activation associated with peripheral cytokine levels in premanifest Huntington's disease gene carriers. Neurobiology of Disease, 83:115–121.

Polyzos AA, McMurray CT (2017) The chicken or the egg: mitochondrial dysfunction as a cause or consequence of toxicity in Huntington's disease. Mech Ageing Dev, 161:181–197.

Prinz M, Jung S, Priller J (2019) Microglia Biology: One Century of Evolving Concepts. Cell, 179:292–311.

Ransohoff RM (2016) How neuroinflammation contributes to neurodegeneration. Science, 353:777–783.

Reiner A, Albin RL, Anderson KD, D'Amato CJ, Penney JB, Young AB (1988) Differential loss of striatal projection neurons in Huntington disease. Proc Natl Acad Sci USA, 85:5733–5737.

Réu P, Khosravi A, Bernard S, Mold JE, Salehpour M, Alkass K, Perl S, Tisdale J, Possnert G, Druid H, Frisén J (2017) The Lifespan and Turnover of Microglia in the Human Brain. Cell Rep, 20:779–784.

Ross CA, Kronenbuerger M, Duan W, Margolis RL (2017) Mechanisms underlying neurodegeneration in Huntington disease: applications to novel disease-modifying therapies. Handb Clin Neurol, 144:15–28.

Ross CA, Poirier MA (2004) Protein aggregation and neurodegenerative disease. Nat Med, 10 Suppl:S10–7.

Roux JC, Zala D, Panayotis N, Borges-Correia A, Saudou F, Villard L (2012) Modification of Mecp2 dosage alters axonal transport through the Huntingtin/Hap1 pathway. Neurobiol Dis, 45:786–795.

Rubinsztein DC, Leggo J, Coles R, Almqvist E, Biancalana V, Cassiman JJ, Chotai K, Connarty M, Crauford D, Curtis A, Curtis D, Davidson MJ, Differ AM, Dode C, Dodge A, Frontali M, Ranen NG, Stine OC, Sherr M, Abbott MH, Franz ML, Graham CA, Harper PS, Hedreen JC, Hayden MR (1996) Phenotypic characterization of individuals with 30-40 CAG repeats in the Huntington disease (HD) gene reveals HD cases with 36 repeats and apparently normal elderly individuals with 36-39 repeats. Am J Hum Genet, 59:16–22.

Rujano MA, Bosveld F, Salomons FA, Dijk F, van Waarde MA, van der Want JJ, de Vos RA, Brunt ER, Sibon OC, Kampinga HH (2006) Polarised asymmetric inheritance of accumulated protein damage in higher eukaryotes. PLoS Biol, 4:e417.

Sankowski R, Böttcher C, Masuda T, Geirsdottir L, Sindram SE, Seredina T, Muhs A, Scheiwe C, Shah MJ, Heiland DH, Schnell O, Grün D, Priller J, Prinz M (2019) Mapping microglia states in the human brain through the integration of high-dimensional techniques. Nat Neurosc 22:2098-2110.

Sapp E, Kegel KB, Aronin N, Hashikawa T, Uchiyama Y, Tohyama K, Bhide PG, Vonsattel JP, DiFiglia M (2001) Early and progressive accumulation of reactive microglia in the Huntington disease brain. J Neuropathol Exp Neurol, 60:161–172.

Sathasivam K, Neueder A, Gipson TA, Landles C, Benjamin AC, Bondulich MK, Smith DL, Faull RL, Roos RA, Howland D, Detloff PJ, Housman DE, Bates GP (2013) Aberrant splicing of HTT generates the pathogenic exon 1 protein in Huntington disease. Proc Natl Acad Sci USA, 110:2366–2370.

Sawiak SJ, Wood NI, Carpenter TA, Morton AJ (2012) Huntington's disease mouse models online: high-resolution MRI images with stereotaxic templates for computational neuroanatomy. PLoS One, 7:e53361.

Schindelin J, Arganda-Carreras I, Frise E, Kaynig V, Longair M, Pietzsch T, Preibisch S, Rueden C, Saalfeld S, Schmid B, Tinevez JY, White DJ, Hartenstein V, Eliceiri K, Tomancak P, Cardona A (2012) Fiji: an open-source platform for biological-image analysis. Nat Methods, 9:676–682.

Schneider WM, Chevillotte MD, Rice CM (2014) Interferon-Stimulated Genes: A Complex Web of Host Defenses. Annual Review of Immunology, 32:513–545.

Sciacca G, Cicchetti F (2017) Mutant huntingtin protein expression and blood–spinal cord barrier dysfunction in huntington disease. Annals of Neurology, 82:981–994.

Semaka A, Kay C, Doty C, Collins JA, Bijlsma EK, Richards F, Goldberg YP, Hayden MR (2013) CAG size-specific risk estimates for intermediate allele repeat instability in Huntington disease. J Med Genet, 50:696–703.

Shankaran M, Marino ME, Busch R, Keim C, King C, Lee J, Killion S, Awada M, Hellerstein MK (2007) Measurement of brain microglial proliferation rates in vivo in response to neuroinflammatory stimuli: application to drug discovery. J Neurosci Res, 85:2374–2384.

Shin J-Y, Fang Z-H, Yu Z-X, Wang C-E, Li S-H, Li X-J (2005) Expression of mutant huntingtin in glial cells contributes to neuronal excitotoxicity. The Journal of Cell Biology, 171:1001–1012.

Sierra A, Encinas JM, Deudero JJ, Chancey JH, Enikolopov G, Overstreet-Wadiche LS, Tsirka SE, Maletic-Savatic M (2010) Microglia shape adult hippocampal neurogenesis through apoptosis-coupled phagocytosis. Cell Stem Cell, 7:483–495.

Siew JJ, Chen HM, Chen HY, Chen HL, Chen CM, Soong BW, Wu YR, Chang CP, Chan YC, Lin CH, Liu FT, Chern Y (2019) Galectin-3 is required for the microglia-mediated brain inflammation in a model of Huntington's disease. Nat Commun, 10:3473.

Silajdžić E, Björkqvist M (2018) A Critical Evaluation of Wet Biomarkers for Huntington's Disease: Current Status and Ways Forward. J Huntingtons Dis, 7:109–135.

Silvestroni A, Faull RL, Strand AD, Möller T (2009) Distinct neuroinflammatory profile in post-mortem human Huntington's disease. Neuroreport, 20:1098–1103.

Silvin A, Ginhoux F (2018) Microglia heterogeneity along a spatio-temporal axis: More questions than answers. Glia, 66:2045–2057.

Simmons DA, Casale M, Alcon B, Pham N, Narayan N, Lynch G (2007) Ferritin accumulation in dystrophic microglia is an early event in the development of Huntington's disease. Glia, 55:1074–1084.

Smith DL, Woodman B, Mahal A, Sathasivam K, Ghazi-Noori S, Lowden PA, Bates GP, Hockly E (2003) Minocycline and doxycycline are not beneficial in a model of Huntington's disease. Ann Neurol, 54:186–196.

Smith LK, He Y, Park JS, Bieri G, Snethlage CE, Lin K, Gontier G, Wabl R, Plambeck KE, Udeochu J, Wheatley EG, Bouchard J, Eggel A, Narasimha R, Grant JL, Luo J, Wyss-Coray T, Villeda SA (2015) β2-microglobulin is a systemic pro-aging factor that impairs cognitive function and neurogenesis. Nat Med, 21:932–937.

Sorolla MA, Reverter-Branchat G, Tamarit J, Ferrer I, Ros J, Cabiscol E (2008) Proteomic and oxidative stress analysis in human brain samples of Huntington disease. Free Radic Biol Med, 45:667–678.

Steffan JS, Kazantsev A, Spasic-Boskovic O, Greenwald M, Zhu YZ, Gohler H, Wanker EE, Bates GP, Housman DE, Thompson LM (2000) The Huntington's disease protein interacts with

p53 and CREB-binding protein and represses transcription. Proc Natl Acad Sci USA, 97:6763–6768.

Steventon JJ, Trueman RC, Ma D, Yhnell E, Bayram-Weston Z, Modat M, Cardoso J, Ourselin S, Lythgoe M, Stewart A, Rosser AE, Jones DK (2016) Longitudinal in vivo MRI in a Huntington's disease mouse model: Global atrophy in the absence of white matter microstructural damage. Sci Rep, 6:32423.

Stifter SA, Greter M (2020) STOP floxing around: Specificity and leakiness of inducible Cre/loxP systems. Eur J Neuroimmunol 50(3):338-341.

Strand AD, Baquet ZC, Aragaki AK, Holmans P, Yang L, Cleren C, Beal MF, Jones L, Kooperberg C, Olson JM, Jones KR (2007) Expression profiling of Huntington's disease models suggests that brain-derived neurotrophic factor depletion plays a major role in striatal degeneration. J Neurosci, 27:11758–11768.

Stremmel C, Schuchert R, Wagner F, Thaler R, Weinberger T, Pick R, Mass E, Ishikawa-Ankerhold HC, Margraf A, Hutter S, Vagnozzi R, Klapproth S, Frampton J, Yona S, Scheiermann C, Molkentin JD, Jeschke U, Moser M, Sperandio M, Massberg S, Geissmann F, Schulz C (2018) Yolk sac macrophage progenitors traffic to the embryo during defined stages of development. Nat Commun, 9:75.

Su P, Zhang J, Wang D, Zhao F, Cao Z, Aschner M, Luo W (2016) The role of autophagy in modulation of neuroinflammation in microglia. Neuroscience, 319:155–167.

Tabrizi SJ, Reilmann R, Roos RA, Durr A, Leavitt B, Owen G, Jones R, Johnson H, Craufurd D, Hicks SL, Kennard C, Landwehrmeyer B, Stout JC, Borowsky B, Scahill RI, Frost C, Langbehn DR, TRACK-HD I (2012) Potential endpoints for clinical trials in premanifest and early Huntington's disease in the TRACK-HD study: analysis of 24 month observational data. Lancet Neurol, 11:42–53.

Tai YF, Pavese N, Gerhard A, Tabrizi SJ, Barker RA, Brooks DJ, Piccini P (2007) Microglial activation in presymptomatic Huntington's disease gene carriers. Brain, 130:1759–1766.

Tay TL, Mai D, Dautzenberg J, Fernández-Klett F, Lin G, Sagar, Datta M, Drougard A, Stempfl T, Ardura-Fabregat A, Staszewski O, Margineanu A, Sporbert A, Steinmetz LM, Pospisilik JA, Jung S, Priller J, Grün D, Ronneberger O, Prinz M (2017) A new fate mapping system reveals context-dependent random or clonal expansion of microglia. Nature Neuroscience, 20:793–803.

Telenius H, Kremer B, Goldberg YP, Theilmann J, Andrew SE, Zeisler J, Adam S, Greenberg C, Ives EJ, Clarke LA (1994) Somatic and gonadal mosaicism of the Huntington disease gene CAG repeat in brain and sperm. Nat Genet, 6:409–414.

The Huntington's Disease Collaborative Research Group (1993) A novel gene containing a trinucleotide repeat that is expanded and unstable on Huntington's disease chromosomes. Cell, 72:971–983.

Tong X, Ao Y, Faas GC, Nwaobi SE, Xu J, Haustein MD, Anderson MA, Mody I, Olsen ML, Sofroniew MV, Khakh BS (2014) Astrocyte Kir4.1 ion channel deficits contribute to neuronal dysfunction in Huntington's disease model mice. Nat Neurosci, 17:694–703.

Trajkovic K, Jeong H, Krainc D (2017) Mutant Huntingtin Is Secreted via a Late Endosomal/Lysosomal Unconventional Secretory Pathway. The Journal of Neuroscience, 37:9000–9012.

Tremblay MÈ, Lowery RL, Majewska AK (2010) Microglial interactions with synapses are modulated by visual experience. PLoS Biol, 8:e1000527.

van den Bogaard SJ, Dumas EM, Roos RA (2013) The role of iron imaging in Huntington's disease. Int Rev Neurobiol, 110:241–250.

Vandesompele J, De Preter K, Pattyn F, Poppe B, Van Roy N, De Paepe A, Speleman F (2002) Accurate normalization of real-time quantitative RT-PCR data by geometric averaging of multiple internal control genes. Genome Biol, 3:RESEARCH0034.

Verdonk F, Roux P, Flamant P, Fiette L, Bozza FA, Simard S, Lemaire M, Plaud B, Shorte SL, Sharshar T, Chrétien F, Danckaert A (2016) Phenotypic clustering: a novel method for microglial morphology analysis. J Neuroinflammation, 13:153.

Villeda SA, Plambeck KE, Middeldorp J, Castellano JM, Mosher KI, Luo J, Smith LK, Bieri G, Lin K, Berdnik D, Wabl R, Udeochu J, Wheatley EG, Zou B, Simmons DA, Xie XS, Longo FM, Wyss-Coray T (2014) Young blood reverses age-related impairments in cognitive function and synaptic plasticity in mice. Nat Med, 20:659–663.

Wake H, Moorhouse AJ, Miyamoto A, Nabekura J (2013) Microglia: actively surveying and shaping neuronal circuit structure and function. Trends Neurosci, 36:209–217.

Wang G, Liu X, Gaertig MA, Li S, Li XJ (2016) Ablation of huntingtin in adult neurons is nondeleterious but its depletion in young mice causes acute pancreatitis. Proc Natl Acad Sci USA, 113:3359–3364.

Wang N, Gray M, Lu XH, Cantle JP, Holley SM, Greiner E, Gu X, Shirasaki D, Cepeda C, Li Y, Dong H, Levine MS, Yang XW (2014) Neuronal targets for reducing mutant huntingtin expression to ameliorate disease in a mouse model of Huntington's disease. Nat Med, 20:536–541.

Weiss A, Träger U, Wild EJ, Grueninger S, Farmer R, Landles C, Scahill RI, Lahiri N, Haider S, Macdonald D, Frost C, Bates GP, Bilbe G, Kuhn R, Andre R, Tabrizi SJ (2012) Mutant huntingtin fragmentation in immune cells tracks Huntington's disease progression. J Clin Invest, 122:3731–3736.

Yona S, Kim KW, Wolf Y, Mildner A, Varol D, Breker M, Strauss-Ayali D, Viukov S, Guilliams M, Misharin A, Hume DA, Perlman H, Malissen B, Zelzer E, Jung S (2013) Fate mapping reveals origins and dynamics of monocytes and tissue macrophages under homeostasis. Immunity, 38:79–91.

Zeitlin S, Liu JP, Chapman DL, Papaioannou VE, Efstratiadis A (1995) Increased apoptosis and early embryonic lethality in mice nullizygous for the Huntington's disease gene homologue. Nat Genet, 11:155–163.

Zhao XF, Alam MM, Liao Y, Huang T, Mathur R, Zhu X, Huang Y (2019) Targeting Microglia Using Cx3cr1-Cre Lines: Revisiting the Specificity. eNeuro, 6(4).

Zlokovic BV (2011) Neurovascular pathways to neurodegeneration in Alzheimer's disease and other disorders. Nat Rev Neurosci, 12:723–738.

Zuccato C, Cattaneo E (2009) Brain-derived neurotrophic factor in neurodegenerative diseases. Nat Rev Neurol, 5:311–322.

Zuccato C, Ciammola A, Rigamonti D, Leavitt BR, Goffredo D, Conti L, MacDonald ME, Friedlander RM, Silani V, Hayden MR, Timmusk T, Sipione S, Cattaneo E (2001) Loss of huntingtin-mediated BDNF gene transcription in Huntington's disease. Science, 293:493–498.

Zuccato C, Tartari M, Crotti A, Goffredo D, Valenza M, Conti L, Cataudella T, Leavitt BR, Hayden MR, Timmusk T, Rigamonti D, Cattaneo E (2003) Huntingtin interacts with

REST/NRSF to modulate the transcription of NRSE-controlled neuronal genes. Nat Genet, 35:76–83.

Statutory Declaration

I, Ekaterini Maria Lyras, by personally signing this document in lieu of an oath, hereby affirm that I prepared the submitted dissertation on the topic "The role of microglia dysfunction in Huntington's Disease", independently and without the support of third parties, and that I used no other sources and aids than those stated.

All parts which are based on the publications or presentations of other authors, either in letter or in spirit, are specified as such in accordance with the citing guidelines. The sections on methodology (in particular regarding practical work, laboratory regulations, statistical processing) and results (in particular regarding figures, charts and tables) are exclusively my responsibility.

Furthermore, I declare that I have correctly marked all of the data, the analyses, and the conclusions generated from data obtained in collaboration with other persons, and that I have correctly marked my own contribution and the contributions of other persons (cf. declaration of contribution). I have correctly marked all texts or parts of texts that were generated in collaboration with other persons.

My contributions to any publications to this dissertation correspond to those stated in the below joint declaration made together with the supervisor. All publications created within the scope of the dissertation comply with the guidelines of the ICMJE (International Committee of Medical Journal Editors; www.icmje.org) on authorship. In addition, I declare that I shall comply with the regulations of Charité – Universitätsmedizin Berlin on ensuring good scientific practice.

I declare that I have not yet submitted this dissertation in identical or similar form to another Faculty.

The significance of this statutory declaration and the consequences of a false statutory declaration under criminal law (Sections 156, 161 of the German Criminal Code) are known to me.

Berlin, 25.10.2020

Ekaterini Maria Lyras

Curriculum Vitae

My curriculum vitae does not appear in the electronic version of my paper for reasons of data protection.

My curriculum vitae does not appear in the electronic version of my paper for reasons of data protection.

Publication list

Rolfes S, Munro DAD, **Lyras EM**, Matute E, Ouk K, Harms C, Böttcher C, Priller (2020) Lentiviral delivery of human erythropoietin attenuates hippocampal atrophy and improves cognition in the R6/2 mouse model of Huntington's disease. Neurobiol Dis 144:105024

Lorenz C, Lesimple P, Bukowiecki R, Zink A, Inak G, Mlody B, Singh M, Mah N, Auré K, Leong M, Zabiegalov O, **Lyras EM**, Pfiffer V, Fauler B, Eichhorst J, Wiesner B, Huebner N, Priller J, Mielke T, Meierhofer D, Izsvák Z, Meier JC, Bouillaud F, Adjaye J, Schuelke M, Wanker EE, Lombès A, Prigione A. (2017) Mitochondrial ATP synthase mutations impair calcium handling and mitochondrial polarization in iPSC-derived neural cells thereby enabling personalized compound screenings. Cell Stem Cell. 20(5):659-674e9.

Mergler S, Garreis F, Sahlmüller M, **Lyras EM**, Reinach P, Dwarakanath A, Paulsen F, Pleyer U. (2012) Calcium regulation by thermo- and osmosensing transient receptor potential vanilloid channels (TRPVs) in human conjunctival epithelial cells. Histochemistry & Cell Biology, 137 (6): 743-61.

Acknowledgements

First of all, I would like to thank Prof. Josef Priller for providing me with this interesting topic, for supervising my doctoral thesis, for his continuous scientific support and critical discussion of the project. I will also be forever grateful to Dr. Chotima Böttcher for supervising and teaching me and for her endless encouragement and care.

I thank everyone responsible for financing this work. More specifically, the SFB TRR43 for the Graduate School Stipend I received and the German Academic Exchange Service for the PhD Scholarship.

In the past years I was always able to rely on scientists and technical assistants at the Charité for scientific, technical and moral support. I would like to specifically thank all former and current members of the AG Priller, it was a pleasure to work with you. I am especially grateful to Jasmin Jamal El-Din and Christian Böttcher for their excellent technical help and for sprinkling my daily life at the lab with great energy and smiles. I would also like to thank Dr. Francisco Fernandez-Klett for kindly and patiently sharing his scientific knowledge and Dr. Simone Rolfes, Qimuge Gong, Anniki Knopp and Camila Fernández Zapata for their camaraderie. I thank Victoria Stiglbauer, Mayumi Kohiyama and Eduardo Matute for their commitment during their internships, Dr. Mareike Voget for translating the summary of this thesis and for her friendship and Julian Tapprich for helping with the illustrations. I would also like to thank members of Experimental Neurology at the Charité and specifically Ingo Przesdzing and Susanne Müller for patiently answering technical questions.

Many thanks go to Dr. Désirée Kunkel, Dr. Kajetan Bentele, Dr. Stefan Paul Koch, Dr. Philipp Boehm-Sturm, Dr. Andreas Weiss, Dr. Alexander Mildner, Dr. Hadas Keren-Shaul, Dr. Ido Amit Dr. Alessandro Prigione and Dr. Ferah Yildirim for their excellent scientific advice and friendly collaboration.

This path was made possible for me through the infinite love of my grandmother, my parents, my brother and my friends. Kostas, Louis, Francesco and Akki, thank you for your friendship, for encouraging me through all of the difficulties and for generously offering laughter and joy as an antidote to all the frustration.

Berlin, October 2020